Institute of Crop Science (340a)
University of Hohenheim
Department of Agronomy
Prof. Dr. Wilhelm Claupein

Implementation and Improvement of an Unmanned Aircraft System for Precision Farming Purposes

Dissertation

In fulfillment of the requirements for the degree of
'Doktor der Agrarwissenschaften'
(Dr. sc. agr. / Ph.D. in Agricultural Sciences)
submitted to the
Faculty of Agricultural Sciences

by
Jakob Geipel
born in Ochsenfurt, Germany

April 2016

This thesis was accepted as a doctoral dissertation in fulfillment of the requirements for the degree of 'Doktor der Agrarwissenschaften' (Dr. sc. agr. / Ph.D. in Agricultural Sciences) by the Faculty of Agricultural Sciences at the University of Hohenheim on March 30, 2016. The colloquium took place on April 13, 2016.

Dean of the Faculty:	Prof. Dr. Ralf T. Vögele
Reviewer:	Prof. Dr. Wilhelm Claupein
	Prof. Dr. Wolfgang Dorner

Contents

Abbreviations and acronyms

CSM	crop surface model
FMIS	farm management information system
GNSS	global navigation satellite system
NDVI	normalized difference vegetation index
NIR	near-infrared radiation spectrum
OGC	Open Geospatial Consortium Inc.
PF	precision farming
REIP	red-edge inflection point
RGB	red green blue
RMSE	root mean square error
RTK	real-time kinematic
SD	standard deviation
TIR	thermal infrared radiation spectrum
UAS	unmanned aircraft system
UAV	unmanned aerial vehicle
VI	vegetation index
VIS	visual radiation spectrum

Summary

Precision farming (PF) is an agricultural concept that accounts for within-field variability by gathering spatial and temporal information with modern sensing technology and performs variable and targeted treatments on a smaller scale than field scale. PF research quickly recognized the possible benefits unmanned aerial vehicles (UAVs) can add to the site-specific management of farms. As UAVs are flexible carrier platforms, they can be equipped with a range of different sensing devices and used in a variety of close-range remote sensing scenarios. Most frequently, UAVs are utilized to gather actual in-season canopy information with imaging sensors that are sensitive to reflected electro-magnetic radiation in the visual (VIS) and near-infrared (NIR) spectrum. They are generally used to infer the crops' biophysical and biochemical parameters to support farm management decisions.

A current disadvantage of UAVs is that they are not designed to interact with their attached sensor payload. This leads to the need of intensive data post-processing and prohibits the possibility of real-time scenarios, in which UAVs can directly transfer information to field machinery or robots. In consequence, this thesis focused on the development of a smart unmanned aircraft system (UAS), which in the thesis' context was regarded as a combination of a UAV carrier platform, an on-board central processing unit for sensor control and data processing, and a remotely connected ground control station. The ground control station was supposed to feature the possibility of flight mission control and the standardized distribution of sensor data with a sensor data infrastructure, serving as a data basis for a farm management information system (FMIS). The UAS was intended to be operated as a flexible monitoring tool for in-season above-ground biomass and nitrogen content estimation as well as crop yield prediction. Therefore, the selection, development, and validation of appropriate imaging sensors and processing routines were key parts to prove the UAS' usability in PF scenarios.

The individual objectives were (i) to implement an advanced UAV for PF research, providing the possibilities of remotely-controlled and automatic flight mission execution, (ii) to improve the developed UAV to a UAS by implementing sensor control, data processing and communication functionalities, (iii) to select and develop appropriate sensor systems for yield prediction and nitrogen fertilization strategies, (iv) to integrate the sensor systems into the UAS and to test the performance in example use cases, and (v) to embed the UAS into a standardized sensor data infrastructure for data storage and usage in PF applications.

This work demonstrated the successful development of a custom rotary-wing UAV carrier platform with an embedded central processing unit. A modular software framework was developed with the ability to control any kind of sensor payload in real-time. The sensors can be triggered and their measurements are retrieved, fused together with the carrier's navigation information, logged and broadcasted to a ground control

station. The setup was used as basis for further research, focusing on information generation by sophisticated data processing.

For a first application of predicting the grain yield of corn (*Zea mays* L.), a simple RGB camera was selected to acquire a set of aerial imagery of early- and mid-season corn crops. Orthoimages were processed with different ground resolutions and were computed to simple vegetation indices (VI) for a crop/non-crop classification. In addition to that, crop surface models (CSMs) were generated to estimate the crop heights. Linear regressions were performed with the corn grain yield as dependent variable and crop height and crop coverage as independent variable. The analysis showed the best prediction results of a relative root mean square error (RMSE) of 8.8 % at mid-season growth stages and ground resolutions of 4 $cm\ px^{-1}$. Moreover, the results indicate that with on-going canopy closure and homogeneity accounting for high ground resolutions and crop/non-crop classification becomes less and less important.

For the estimation of above-ground biomass and nitrogen content in winter wheat (*Triticum aestivum* L.) a programmable multispectral camera was developed. It is based on an industrial multi-sensor camera, which was equipped with bandpass filters to measure four narrow wavelength bands in the so-called red-edge region. This region is the transition zone in between the VIS and NIR spectrum and known to be sensitive to leaf chlorophyll content and the structural state of the plant. It is often used to estimate biomass and nitrogen content with the help of the normalized difference vegetation index (NDVI) and the red-edge inflection point (REIP). The camera system was designed to measure ambient light conditions during the flight mission to set appropriate image acquisition times, which guarantee images with high contrast. It is fully programmable and can be further developed to a real-time image processing system. The analysis relies on semi-automatic orthoimage processing. The NDVI orthoimages were analyzed for the correlation with biomass by means of simple linear regression. These models proved to estimate biomass for all measurements with RMSEs of 12.3 % to 17.6 %. The REIP was used to infer nitrogen content and showed good results with RMSEs of 7.6 % to 11.7 %. Both NDVI and REIP were also tested for the in-season grain yield prediction ability (RMSE = 9.0–12.1 %), whereas grain protein content could be modeled with the REIP, except for low-fertilized wheat plots.

The last part of the thesis comprised the development of a standardized sensor data infrastructure as a first step to a holistic farm management. The UAS was integrated into a real-time sensor data acquisition network with standardized data base storage capabilities. The infrastructure was based on open source software and the geo-data standards of the Open Geospatial Consortium (OGC). A prototype implementation was tested for four exemplary sensor systems and proved to be able to acquire, log, visualize and store the sensor data in a standardized data base via a sensor observation service on-the-fly. The setup is scalable to scenarios, where a multitude of sensors, data bases, and web services interact with each other to exchange and process data.

This thesis demonstrates the successful prototype implementation of a smart UAS and a sensor data infrastructure, which offers real-time data processing functionality. The UAS is equipped with appropriate sensor systems for agricultural crop monitoring and has the potential to be used in real-world scenarios.

Zusammenfassung

'Precision farming' (PF) ist ein landwirtschaftliches Konzept, das die Variabilität innerhalb eines Feldes berücksichtigt, indem es mit Hilfe moderner Sensortechnologien räumliche und zeitliche Bestandsinformationen sammelt. Dadurch ist PF in der Lage, gezielte teilflächenspezifische Anwendungen innerhalb eines Feldes durchzuführen. Die Forschung im Bereich von PF hat früh die potenziellen Vorzüge von kleinen Luftfahrzeugen, sogenannten 'unmanned aerial vehicles' (UAVs), für die teilflächenspezifische Bewirtschaftung erkannt. Da UAVs flexible Lastenträger darstellen, können sie mit den verschiedensten Sensoren ausgestattet und in einer Vielzahl von fernerkundlichen Anwendungsfällen in der Landwirtschaft genutzt werden. Dabei werden sie am häufigsten mit bildgebenden Sensoren eingesetzt, um aktuelle Informationen über den Pflanzenbestand in der Vegetationsperiode zu liefern. Die eingesetzten Sensoren sind dabei meist zur Messung elektromagnetischer Strahlung im sichtbaren (VIS) und nahen infraroten (NIR) Bereich ausgelegt. Im Allgemeinen werden sie dazu benutzt auf biophysikalische und biochemische Eigenschaften der Nutzpflanzen zu schließen und damit die Entscheidungsprozesse in der Bestandsführung zu unterstützen.

Ein aktueller Nachteil der UAVs ist, dass sie nicht dafür gebaut werden um mit ihrer Nutzlast zu interagieren. Das führt zu einem Bedarf an erheblicher Datennachverarbeitung und verhindert Echtzeitszenarios, in denen UAVs Informationen direkt an Feldmaschinen und Roboter senden können. Aus diesem Grund konzentrierte sich diese Dissertation auf die Entwicklung eines intelligenten fliegenden Systems, eines sogenannten 'unmanned aircraft system' (UAS), welches im Kontext dieser Dissertation als eine Kombination aus UAV Trägerplattform, zentralem Computer zur Sensorsteuerung und Datenverarbeitung, sowie einer entfernt verbundenen Bodenstation betrachtet wurde. Die Bodenstation war zur Flugüberwachung und zur standardisierten Verteilung der Sensordaten über eine Sensordateninfrastruktur bestimmt. Die Sensordateninfrastruktur diente als Basis eines sogenannten 'farm management information system' (FMIS), das die Verwaltung und Bewirtschaftung eines landwirtschaftlichen Betriebs mit Methoden der Informatik unterstützt. Das UAS sollte als flexibles Aufklärungswerkzeug eingesetzt werden, um Schätzungen von Biomasse, Stickstoffgehalt und erwartetem Ertrag während der Vegetationsperiode zu liefern. Daher war die Auswahl, Entwicklung und Validierung geeigneter bildgebender Sensoren und zugehöriger Verarbeitungsmethoden ein zentraler Bestandteil, um die Nutzbarkeit von UAS im PF zu belegen.

Die einzelnen Ziele waren (i) der Aufbau eines UAVs für das PF, das sich fernsteuern und automatisch nach Wegpunkten fliegen lässt, (ii) die Erweiterung des UAVs zum UAS, durch die Entwicklung einer zentralen Sensorsteuerung, Datenverarbeitung und Kommunikationsfähigkeit, (iii) die Auswahl und Entwicklung geeigneter Sensorsysteme zur Ertragsschätzung und Stickstoffdüngung, (iv) der Einbau der Sensorsysteme in das UAS und deren Validierung in Beispielanwendungen und (v) die Integration des UAS

in eine standardisierte Sensordateninfrastruktur um die Daten für PF-Anwendungen abzuspeichern und verfügbar zu machen.

Diese Dissertation präsentiert eine erfolgreiche Entwicklung eines Drehflügler-UAVs mit zentraler Steuereinheit. Dazu passend wurde eine modulare Software entwickelt, die jegliche Sensorik in Echtzeit steuern kann. Messungen können ausgelöst, empfangen, mit den Navigationsdaten des UAVs fusioniert, gespeichert und an eine Bodenstation gesendet werden. Das UAV diente als Basis weiterer Forschung, die die Verarbeitung von Sensordaten zur Erzeugung pflanzenbaulicher Information zum Ziel hatte.

Eine erste Anwendung war die Ertragsschätzung von Körnermais (*Zea mays* L.). Eine einfache RGB Kamera wurde dazu benutzt Luftbilder von Maispflanzen in frühen und mittleren Wachstumsstadien aufzunehmen. Daraus wurden Orthophotos mit unterschiedlichen Bodenauflösungen erzeugt und zu einfachen Vegetationsindizes (VIs) zur Klassifizierung der Pixel als 'Pflanze' oder 'nicht Pflanze' weiterverarbeitet. Zusätzlich wurden Oberflächenmodelle des Pflanzenbestands, sogenannte 'crop surface models' (CSMs), erzeugt, um die Pflanzenhöhen abzuschätzen. Mit dem Ertrag als abhängige Variable, sowie Pflanzenhöhe und Bedeckungsgrad als unabhängige Variablen, wurden lineare Regressionen durchgeführt. Die Analyse ergab beste Vorhersagen mit geringsten Standardabweichungen (SD) von 8.8 % für die Messungen in mittleren Wachstumsstadien mit einer Bodenauflösung von 4 $cm\ px^{-1}$. Darüber hinaus zeigten die Ergebnisse, dass hohe Bodenauflösungen und Klassifizierung mit fortschreitendem Reihenschluss und sich angleichendem Pflanzenbestand immer unwichtiger werden.

Zur Schätzung von Biomasse und Stickstoffgehalt von Winterweizen (*Triticum aestivum* L.) wurde eine programmierbare multispektrale Kamera entwickelt. Sie basiert auf einer Industriekamera mit mehreren Sensorköpfen, von denen jeder mit einem Bandpassfilter bestückt wurde. Die Kamera misst vier schmalbandige Wellenlängen im Übergangsbereich vom VIS- zum NIR-Spektrum, der sogenannten roten Kante 'red-edge'. Dieser Bereich ist dafür bekannt Rückschlüsse auf den Chlorophyllgehalt der Blätter und die Pflanzenstruktur zuzulassen. Mit Hilfe der Formeln zur Berechnung des 'normalized difference vegetation index' (NDVI) und des 'red-edge inflection point' (REIP) wird dieser Bereich oft zur Schätzung von Biomasse und Stickstoffgehalt genutzt. Das Kamerasystem wurde darüber hinaus entworfen, die Lichtverhältnisse während des Fluges zu messen und geeignete Belichtungszeiten festzulegen, um Bilder mit hohem Kontrast zu erzeugen. Die Kamera ist komplett programmierbar und kann zur Echtzeitbildverarbeitung weiterentwickelt werden. Die Untersuchung basiert auf der teilautomatisierten Erzeugung von Orthophotos. Die NDVI Orthophotos wurden mit Hilfe einer einfachen linearen Regression auf ihre Korrelation mit Biomasse getestet. Sie zeigten über alle Messzeitpunkte, dass sie Biomasse mit Standardabweichungen von 12.3 % bis 17.6 % schätzen konnten. Der REIP wurde zur Stickstoffgehaltschätzung heran gezogen und zeigte gute Ergebnisse mit Standardabweichungen von 7.6 % bis 11.7 %. Beide, NDVI und REIP, wurden auch auf ihre Vorhersagefähigkeit des Korn-

ertrags getestet (SD = 9.0–12.1 %). Überdies konnte, außer in gering gedüngten Parzellen, der Proteingehalt im Korn mit dem REIP abgeschätzt werden.

Der letzte Teil der Dissertation beinhaltete die Entwicklung einer standardisierten Sensordateninfrastruktur als Schritt hin zu einem umfassenden Bewirtschaftungskonzept, das möglichst viele Faktoren berücksichtigt. Das UAS wurde in ein echtzeitbasiertes Sensordatennetzwerk integriert, das Sensordaten erfassen und standardisiert in Datenbanken ablegen kann. Die Infrastruktur basiert auf quellcodeoffener 'open source' software und den Geodatenstandards des Open Geospatial Consortiums (OGC). Eine erste Umsetzung einer solchen Infrastruktur wurde mit vier Beispielsensoren getestet und zeigte, dass Sensordaten in Echtzeit erfasst, lokal gespeichert, visualisiert und mittels eines Sensordatendienstes ('sensor observation service') standardisiert in einer Datenbank gespeichert werden konnten. Die Umsetzung ist auf eine beliebige Anzahl von Sensoren und Diensten erweiterbar und ermöglicht ihnen den Austausch und die Verarbeitung von Daten.

Diese Dissertation zeigt eine erfolgreiche Umsetzung eines intelligenten UAS und einer Sensordateninfrastruktur, die Sensordatenverarbeitung in Echtzeit anbietet. Das UAS ist mit Sensoren ausgestattet, die zur landwirtschaftlichen Beurteilung von Pflanzenbeständen geeignet sind und zeigt Potential auch unter realistischen Bedingungen eingesetzt werden zu können.

1 Introduction

Crop production relies on agronomic experience and the ability to adapt management strategies to a vast amount of agricultural parameters. Accurate information about weather, soil and crop status are, amongst others, key factors for effective and valuable management. Besides experience, visual examination, and sensor readings, crop growth models are useful tools to support farmers in deriving management decisions. Crop growth models depend on estimates of the parameters, which are often derived from field samples. As many parameters change throughout the growing season, repeated sampling is desired to increase model prediction accuracy and to improve the quality of management decisions. However, frequent sampling increases work load and expenses. While parameter selection and finding appropriate modeling strategies for parameter assessment are sophisticated tasks, data sampling is often a tiring labor. With the advancement of motion systems, sensors, and algorithms machines may overcome these problems thus taking over more and more tasks of this information management process and proposing best-management practices to the farmers.

1.1 Precision farming - a long way to adoption

Regarding the raising demand for food due to an increase in global population in the next decades, crop and livestock production must improve nutrient and water use efficiency, as well as integrated pest management to avoid negative environmental impacts (Tilman et al., 2002). With the end of the last millennium, the idea of accounting for within-field variability was transferred to precision farming (PF) as an agricultural concept, exploiting the possibilities of improving agricultural application and information technologies (Stafford, 2000; Whelan and McBratney, 2000; Auernhammer, 2001). PF was intended to avoid the drawbacks of uniform treatments by gathering spatio-temporal information and performing variable and targeted treatments on a smaller scale than a field scale. Stafford (2000) described this as a possible solution to "[...] meet much of the increasing environmental, economic, market and public pressures on arable agriculture." He identified three barriers to overcome before PF will be widely accepted. First, the development of expert systems, to support farmers' management decisions. These systems shall process data to information, whereas the data should be treated in a standardized way. Second, the evolution of algorithms and strategies for localized applications and their scientific evidence of benefit. Third, the development of automatic sensor systems, which are able to sense specific factors or suitable surrogates, as well as the development of more precise application technologies and localization methods. He believed that these problems would have been solved during the first decade of the 21st century and most arable enterprises will have adopted PF on a whole-farm basis by the end of 2009. From today's view, one can say that this prediction was too optimistic.

Several surveys have been conducted to disseminate the adoption of PF technologies and strategies by farmers in European countries. Reichardt et al. (2009) interviewed German farmers from 2001 to 2007. They found a slight increase from 6.65 % (2001) to 9.33 % (2007) in the number of PF users, as well as an increase from 54 % (2001) to 62 % (2007) in the number of farmers that were aware of PF technologies. Pedersen et al. (2004) identified 400 Danish farmers (approximately 9 % of the cereal acreage), who used some sort of PF technology in 2004. In more recent research on the use of advanced farming systems in 2009, Lawson et al. (2011) reported the use of one or more PF practices for 24 % of the German, 9 % of the Danish, and 3 % of the Finnish survey participants. These numbers cannot be seen as a wide adoption of PF in agricultural practice. Nevertheless, these studies show an increasing amount of farmers being aware of the potential of PF. However, regardless of the benefits PF management promises at its current state, farmers are still unsure about the importance of PF technologies for future agriculture. Reichardt et al. (2009) identified that farmers still lack knowledge about the correct application of PF management strategies. Moreover, they pointed out two other drawbacks: the time spent to get used to the new technologies and the heterogeneity of machinery and software standards of different vendors. In consequence, one must state that some of the barriers still exist.

Regarding the defined barriers, most advances were made in the domains of localization, sensing and application technology. With the upcoming of real-time kinematic (RTK) global navigation satellite system (GNSS) localization possibilities, high position accuracy led to an increased use of spatial information in the agricultural management process. Accurate mapping of yields, sampling of soil, and targeted applications of inputs were popular steps towards a site-specific consideration of with-in field heterogeneity. For this purpose, sensor systems were developed to measure soil electric conductivity (Adamchuk et al., 2004; Corwin and Lesch, 2005), combine harvesters were equipped with yield assessment capabilities (Reyns et al., 2002), and implements were used to apply and document variable rates of inputs (Bongiovanni and Lowenberg-Deboer, 2004). More recent research focused on the improvement of sensor systems and navigation capabilities of tractors and implements. Automatic steering systems and even more accurate sensing and application technologies generate new possibilities in row-culture cultivation (Åstrand and Baerveldt, 2005; Kise et al., 2005), controlled traffic applications (Tullberg et al., 2007; McHugh et al., 2009), seeding (Griepentrog et al., 2005; Leemans and Destain, 2007), and weeding (Weis et al., 2008; Rueda-Ayala et al., 2015). As time-saving and non-destructive sampling methods were preferred, the use of satellite, airborne and ground-based remote-sensing systems is very popular (Heege et al., 2008; Erdle et al., 2011; Thenkabail et al., 2012). Their optical multi- and hyperspectral sensors provide the ability to infer crop parameters by measuring electro-magnetic radiation. Predominantly, biomass, leaf area, chlorophyll concentration, and nitrogen status are determined by leaf and canopy reflection in the visual

(VIS) and the near-infrared (NIR) wavelength bands (Rouse Jr. et al., 1974; Horler et al., 1983; Guyot et al., 1988; 1992). In addition, fluorescence sensitive techniques to determine the photosynthetic activity and thermal infrared (TIR) techniques to infer the water status of crops are the focus of on-going research (Jones et al., 2009; Rascher et al., 2010).

Despite Stafford (2000), Whelan and McBratney (2000) clearly pointed out the importance of scientific evidence that farmers benefit from variable field management. It is common sense that this benefit cannot be solely measured in economic terms. This benefit shall rather be seen as a guarantee of high crop production level and quality together with the preservation of the environment by a reduction of inputs (Whelan and McBratney, 2000; Auernhammer, 2001; Tilman et al., 2002; McBratney et al., 2005). Researchers were constantly working on proofing this hypothesis throughout the last years. They have developed many algorithms for variable field management and conducted a multitude of field experiments to investigate improved nutrient, soil, water, and pest management. However, with the definition of benefit being rather vague, it has become inherent that a universal final conclusion cannot be drawn.

The development of proper decision-support systems is still a major obstacle. This applies mostly to the holistic data management of a farm, comprising all processes about crop, soil and climatic information (Fountas et al., 2015). Farm management information systems (FMIS) can be seen as tools for the acquisition, the processing, the storage, the documentation, and the distribution of farming data, which support and enable farmers to derive sophisticated management decisions (Sørensen et al., 2010). Fountas et al. (2015) gave a very recent overview on the current situation of FMIS in precision agriculture. Again, economic benefit and user-friendliness were recognized as general adoption barriers for farmers. In terms of precision farming processes, they particularly identified the need to cover large amounts of spatio-temporal data, which arise in field production. As these geo-data commonly originate from a multitude of data sources, standardized data handling is of great importance. As a solution to facilitate the use of FMIS by standardization, Nash et al. (2009) proposed the use of geo-spatial web services to build sophisticated data infrastructures. These infrastructures offer the possibility to automate agricultural data processing, even for mobile scenarios. Kaivosoja et al. (2014), for example, introduced an exemplary implementation in weed spraying, proving that automatic farming operations can be built with these infrastructures.

The development within the last years shows that PF research is continuously working on dismantling the identified barriers. However, farmers still need to invest a lot of time, technology, and knowledge. As the ratio of economic benefit and investment is small, farmers hesitate to adopt PF, yet.

1.2 Unmanned aircraft systems as agricultural observers

The advance in technical development has brought up consumer grade miniature aircrafts, so-called unmanned aerial vehicles (UAVs) or unmanned aircraft systems (UASs). The Civil Aviation Authority describes a UAS as a combination of an unmanned aircraft, a carrier platform, a communication link, a remote pilot station and all other elements necessary to enable flight (CAA, 2015). UAV and UAS are only two of a multitude of terms, which are currently in use. To clarify their use in this thesis, this work utilizes UAV in the context of a remotely or automatically piloted aerial vehicle, whereas UAS is used to describe a more complete system, comprising a UAV, a central processing unit to combine all sensors and a data communication infrastructure.

UAVs develop to popular means for rapid and comprehensive field data acquisition (Zhang and Kovacs, 2012). They can be used as carrier platforms and be equipped with a multitude of different sensor systems. This leads to certain advantages compared to traditional remote sensing with satellites (Van Der Wal et al., 2013; Zecha et al., 2013). First, the sensor system can be exchanged in accordance to the intended task. In consequence, almost any kind of data can be generated. Second, UAVs can be operated at any time when needed, except in very poor weather situations. Third, being close to the ground, these aircrafts provide cloud-free data with a very high spatial resolution. Satellites, in contrast, have the advantages of advanced sensor calibration models and high spatial coverages.

The UAVs are classified by different categories, like maximum take-off weight, vertical take-off and landing capability, flying altitude and endurance (Watts et al., 2012). PF research typically uses so-called micro UAVs. In most countries, they are considered to be model aircrafts. They do not fall under the stricter rules of aviation. Typically, they are allowed to be piloted in an operators visual line-of-sight and a maximum flight level of around 100–150 m. They are either fixed-winged (airplane) or rotary-winged (multi-rotor helicopter) with a maximum take-off weight of less than 5 kg and an endurance of 15–30 min. Often, they can be piloted by both remote control and autopilot following a pre-defined route of waypoints (Zhang and Kovacs, 2012).

In PF research, UAVs are utilized to gather comprehensive data sets of the actual field situation throughout the growing season. Imaging systems, like standard or customized RGB, multispectral, and hyperspectral cameras are the most frequent sensors in use. Aasen et al. (2015) categorized these cameras as either sensitive in just a few wavelength bands (RGB and multispectral) or in a multitude of bands (hyperspectral). Hyperspectral cameras are more sophisticated sensors, providing a high spectral resolution, comparable to the one of field spectrometers. Nevertheless, all cameras share one important feature. They provide a high spatial resolution and, therefore, coverage for large areas.

Within the last years, extensive research with UAVs has been conducted for a wide range of agricultural applications. Most of the studies utilized the same methods as the

established ground-based systems. They analyzed the radiometric response, which was reflected by the canopy in the VIS, NIR and TIR radiation spectrum (Thenkabail et al., 2012). Building on the experience from satellite remote sensing, many field studies used multispectral camera systems to derive different plant parameters. Hunt Jr. et al. (2010) modified a custom RGB camera to make it sensitive to the NIR spectrum and assessed the leaf area index in winter wheat (*Triticum aestivum* L.). Primicerio et al. (2012) used a multispectral imaging sensor and a structural vegetation index (VI) to derive vigour maps of vineyards (*Vitis* L.). Stagakis et al. (2012) monitored water stress in orange orchards (*Citrus sinensis* L.) with the help of physiological vegetation indices and Borra-Serrano et al. (2015) developed a routine for multispectral mapping of different weed species in sunflower fields (*Helianthus* L.).

Thermal cameras are also increasingly tested to measure canopy temperature to infer water stress. Berni et al. (2009) have conducted a study with thermal and narrow band reflection information to quantify the leaf area index, chlorophyll content, water stress, and the canopy temperature in different agricultural fields. Gonzalez-Dugo et al. (2013) derived a new crop water stress index by investigating the water status of fruit trees. Kusnierek and Korsaeth (2014) showed some limitations of this technique on UAVs but proved that it is possible to distinguish between stressed and non-stressed barley (*Hordeum vulgare* L.) plants.

With the advancement of lightweight hyperspectral imaging sensors, more and more narrow bands were captured in order to provide imagery with more detailed spectral information. Researchers started to work on fusing the knowledge of field spectrometry with the techniques of image analysis and produced very sophisticated UAV sensing methods. Zarco-Tejada et al. (2012) used a thermal and a hyperspectral imaging sensor to compute multiple VIs and to detect chlorophyll fluorescence emissions to infer water status in orange (*Citrus sinensis* L.) and mandarin orchards. Calderón et al. (2013) detected the infection of olive trees with *Verticillium wilt*, both, with thermal information and chlorophyll fluorescence, generated by thermal and hyperspectral imaging devices. Burkart et al. (2015) investigated the compensation of angular effects on spectral reflection of wheat by bi-directional reflection modeling to improve hyperspectral data of vegetation, derived by UAVs. Although they used a non-imaging hyperspectral device, the method is valuable and adoptable for imaging sensors, too.

Another recent strategy is to utilize aerial imagery and structure from motion techniques to create 3D crop surface models (CSMs). The idea is to combine spatial information and canopy heights with spectral reflection information. Bendig et al. (2015) have investigated the possibilities of this approach to estimate biomass in barley fields, whereas Zarco-Tejada et al. (2014) and Díaz-Varela et al. (2015) developed combined methods to extract tree heights in olive orchards (*Olea europaea* L.). Aasen et al. (2015) describe a method to produce multi-layered hyperspectral imagery to derive a multitude of narrow band VIs and a CSM in barley for chlorophyll and biomass

detection.

The studies demonstrate the potential of close-range remote sensing as valuable source of information for intelligent field management. Frequently updated information about the field conditions add great value to crop growth and management models. However, UAVs cannot be considered as fully operational systems for agricultural practice, yet. Besides the need of training and experience for operation, current UAVs in agricultural scenarios lack an important feature: standardized methods for image processing and information extraction. One major drawback is that there is still need for expert knowledge and intensive post-processing to transform sensor data into information. Another drawback is that the sensor measurements are commonly not accessible before the UAV has returned to ground. In consequence, data needs to be acquired and forwarded to a data base and processing system manually.

Developing into a mobile and inter-connected agriculture with instantaneous decision support, UAVs do not satisfy the demand of an easy integration into the farm management process. An obvious solution is to evolve UAVs into smarter systems, connecting the carrier platforms with the sensor devices, adding some real-time sensor control and data processing functionality and enable them to communicate with remote computers and agricultural machines on-the-fly. Recent studies point out the direction, which machine-to-machine communication and robotization can lead to. Initial considerations were to develop UASs and embed them into real-time applications, utilizing them as agricultural scouts for information retrieval. Kazmi et al. (2011) propose to operate ground vehicles together with UASs, which are used to detect and localize weed and transfer this information to the ground vehicles for close-to-crop inspection. Kuhnert et al. (2012) demonstrated a realization of such an approach, by transmitting aerial imagery from a UAS to a ground robot, which processes the images to detect objects and to approach their locations for possible treatments. Hernandez et al. (2015) performed a first indoor experiment to calculate the volume of the grain inside a trailer during harvesting to automatize and optimize trailer and spout movements.

With regard to the possibility of acquiring accurate actual canopy information at a large scale and the opportunities robotic fleets and real-time data processing generate for automatized crop management, it is necessary to overcome the current limitations of UAVs. There is an inherent need of smart UAS, facilitating the use and the agricultural information generation by standardized data exchange and improved processing methods.

1.3 Objectives

This thesis examines the applicability of a UAS and attached sensor devices as a mean of information retrieval in the domain of PF. Therefore, it builds on the progress in PF sensing and application technology. The thesis focuses on the improvement of sensor data acquisition, storage, and processing for typical PF applications. The following

overview lists the objectives in detail. The objectives were

- to implement an advanced UAV for PF research, providing the possibilities of remotely-controlled and automatic flight mission execution,
- to improve the developed UAV to a UAS by implementing sensor control, data processing and communication functionalities,
- to select and develop appropriate sensor systems for yield prediction and nitrogen fertilization strategies,
- to integrate the sensor systems into the UAS and to test the performance in example use cases,
- and to embed the UAS into a standardized sensor data infrastructure for data storage and usage in PF applications.

1.4 Structure

Section 1 gives insight into the recent development of PF and close range remote sensing technologies in agriculture. It points out the barriers for a wide adoption of PF and the latest applications of UAVs and UASs in this domain. Furthermore, it formulates the thesis' objectives and gives a structural overview.

Section 2 introduces a concept to enhance common UAV technology by equipping UAVs with an embedded low-cost computer to improve sensor control and sensor data acquisition methods. In example, a real-time sensor data software framework was developed to control sensor devices and to retrieve, fuse, log and broadcast sensor data on-the-fly. The setup was implemented on a custom UAV, commonly used in the PF research domain. The implementation shows a way to enrich UAVs with UAS functionality and proved its usability with attached temperature, humidity and imaging sensors.

Section 3 provides an example use case of the prototype UAS for mid-season prediction of corn (*Zea mays* L.) yield potential. Aerial images were acquired in the photosynthetically active radiation spectrum and analyzed with a combined spectral and spatial modeling approach. The images were used to compute VIs for crop/non-crop classification and 3D CSMs for crop height determination. Classification results and crop height data were tested on their corn yield prediction ability with three linear regression models. A combined approach showed the best results and proved to be a suitable method for mid-season corn yield prediction.

Section 4 illustrates in-season biomass and nitrogen status detection for use in split fertilization strategies. A programmable industrial camera system was configured to serve as a multispectral camera on the prototype UAS. Images were acquired in the so-called red-edge region, a transition zone in between the visual and the near-infrared

radiation spectrum, and related to the above-ground biomass and nitrogen content at different growth stages of winter wheat. The acquired multispectral images were processed to normalized difference vegetation index (NDVI) and red-edge inflection point (REIP) orthoimages for an analysis with simple linear regression models. The results indicate good estimations of biomass and nitrogen content, as well as in-season prediction abilities of final grain yield and grain protein content.

Section 5 describes a method to utilize open source software and data standards of the Open Geospatial Consortium for the realization of a holistic sensor data infrastructure for PF applications. The proposed infrastructure implemented four exemplary PF sensor systems: (i) a stationary weather sensor for measuring temperature and relative humidity; (ii) a stationary spectrometer for the registration of incident solar radiation; (iii) a tractor, equipped with a fluorescence sensor for the detection of within-field plant health; and (iv) the prototype UAS, equipped with two camera systems and a spectrometer, for the detection of the plants' spectral signatures. The infrastructure covers the control of sensors, the access to the sensor data and the transmission of the sensor data to a sensor observation service, which stores the sensor data in a standardized data base. In addition, the sensor observation service gives farmers and computer systems the possibility to access the sensor data in a well-defined way and to utilize them in web service-based farming applications.

Section 2 is a peer-reviewed article, which has been published in the proceedings of an international conference. Sections 3–5 consist of articles, which have been published in international peer-reviewed scientific journals. Section 6 discusses the findings, which are presented in Sections 2–5 with regard to the objectives of this thesis, as presented in Section 1. In addition, it evaluates the applicability of the UAS in PF practice and points out the expected perspectives.

2 Enhancement of micro Unmanned Aerial Vehicles for agricultural aerial sensor systems

Geipel, J., G. G. Peteinatos, W. Claupein and R. Gerhards, 2013. Enhancement of micro Unmanned Aerial Vehicles for agricultural aerial sensor systems. In J. V. Stafford, ed., *Precision agriculture '13*, pp. 161–167. Wageningen Academic Publishers, Wageningen, The Netherlands.

UAVs are used in most agricultural close-range remote sensing scenarios. They serve as carrier platforms for the sensor devices, which are needed to infer crop parameters and ambient growing conditions. A major disadvantage of these UAVs is that they are not designed to interact with the attached sensor payload. In consequence, each sensor utilizes an individual control unit and data storage device, not being able to exchange and process all acquired data on-the-fly. This leads to two limitations. On the one hand, real-time scenarios, in which UAVs act as scouts for information retrieval or robotic field work coordination, are impossible. On the other hand, the inherent need for post-mission data processing increases the effort for the generation of information for decision support.

This publication focuses on the development of a UAS, which combines a carrier platform with the possibilities of real-time sensor data processing and, in addition, provides broadcasting functionality to enable communication with a ground control station. Therefore, a custom rotary-wing UAV was equipped with a central processing unit and a modular software framework was developed to control any kind of sensor device. It provides the functionality to trigger sensor measurements, to retrieve the sensed data, to fuse the sensed data from all attached sensors, to log the data on a storage device and to broadcast the data to a remote ground control station. The setup was tested in an above-field micro-climate mapping scenario with exemplary low-cost location, temperature, humidity and imaging sensors. The framework successfully performed the desired operations and proved to generate location-based sensor data in real-time. The developed UAS was used in combination with more sophisticated sensor systems in the subsequent parts of the work (see Section 3–4).

Enhancement of micro Unmanned Aerial Vehicles for agricultural aerial sensor systems

J. Geipel[1], G.G. Peteinatos[2], W. Claupein[1] and R. Gerhards[2]
[1]*Institute of Crop Science, Department of Agronomy (340a), University of Hohenheim, Fruwirthstraße 23, 70599 Stuttgart, Germany; jakob.geipel@uni-hohenheim.de*
[2]*Institute of Phytomedicine, Department of Weed Science (360b), University of Hohenheim, Otto-Sander-Straße 5, 70599 Stuttgart, Germany*

Abstract

Micro Unmanned Aerial Vehicles (UAV) are used in a variety of agricultural research applications. However, UAVs are often not designed to interact with their attached sensor devices. This circumstance leads to disadvantages in sensor data acquisition and leads to increased efforts in post-mission data processing. This paper introduces a real-time sensor data software framework, executed on an embedded low-cost computer to aggregate carrier and sensor device measurements. The proposed setup provides functionality to control sensor devices and to retrieve, fuse, log and broadcast sensor data on-the-fly. A prototype implementation proved its functionality in an example use case of above-field micro-climate mapping with low-cost temperature, humidity and image sensors.

Keywords: UAV, embedded computer, sensor data fusion, software framework

Introduction

Micro UAVs have evolved to valuable carrier platforms for environmental sensor devices. Using appropriate sensors, these platforms are able to support site-specific management decisions by providing data in a high spatial, temporal and even radiometric resolution (Hunt *et al.*, 2010; Lelong *et al.*, 2008; Primicerio *et al.*, 2012).
Typically, aerial platforms, such as UAVs, and their mounted sensors are designed as independent systems without intercommunication. These platforms are intended to operate flight missions and to provide detailed geographical location information by their onboard navigation sensors, while sensor devices are mounted to sense environmental parameters. Frequently, these devices do not communicate with the carrier's flight system and store sensed observations in proprietary data storage devices, which are independent of that of the carrier platform. However, most researchers are interested in location-based sensor data, e.g. for the determination of image positions (Berni *et al.*, 2009; Xiang and Tian, 2011). Standard UAV-based sensor system designs rarely offer the possibility of real-time data exchange. Consequently, the desired connection of geographical location and sensor data is commonly established by using soft- and hardware solutions, specially designed for the specific sensor device (Hruska *et al.*, 2012; Huang *et al.*, 2010), or by time-consuming post-processing after completion of the flight mission (Grenzdörffer *et al.*, 2008).
Embedded small and light-weight computer systems, carrying out on-board sensor fusion and system tasks, are able to reduce these efforts in sensor data processing (Kuhnert *et al.*, 2012). Following this idea, this work proposes a low-cost implementation of an on-the-fly processing, sensor data-fusing software framework, by inter-connecting carrier and sensor devices, based on a mounted embedded computer as processing and storage unit. This system approach is designed to establish a wireless data link between the processing unit and a base receiver station for flight mission monitoring and real-time data logging.
The operability of the implemented low-cost aerial sensor system was evaluated by conducting a field test experiment. Therefore, an example mapping of micro-climate conditions was carried out

to test the functionality of the software framework and to infer whether low-cost climate sensors are potentially useful to provide location-based micro-climate information around plant development and micro-climate in-field variability.

Materials and methods

Hardware setup

The carrier platform '*Hexe*', which was used to carry out the field tests, is a modified Mikrokopter UAV (HiSystems GmbH, Moormerland, Germany), which operates for approximately 10 min while carrying a sensor payload of 1 kg. It is a vertical take-off and landing, six-rotor, micro UAV, equipped with various navigation sensors. A three-axis accelerometer, a three-axis gyroscope, a three-axis magnetic compass, a barometric pressure sensor and a global positioning system (GPS) receiver allow '*Hexe*' to process navigation information during the flight mission. An internal navigation filter updates a strapdown inertial navigation algorithm with information from the aforementioned GPS, magnetic compass and barometric pressure sensors. Exploiting this position information, a control loop governs the rotors' speeds, enabling *'Hexe'* to hover at given positions and to autonomously follow user-defined waypoint routes. *'Hexe'* offers a serial interface (RS-232), over USB or the Bluetooth wireless port to access its navigation information in real-time.

Core element of the aerial sensor system is a credit-card sized Raspberry Pi Model B computer (Raspberry Pi Foundation, Caldecote, Cambridgeshire, UK). It is equipped with a Broadcom BCM2835 system on a chip, including a 700 MHz ARM11 processor and 256 MB of random-access memory (RAM). Amongst others, it provides two Universal Serial Bus (USB) ports, one Ethernet (LAN) port and 26 general purpose input/output (GPIO) pins to connect the carrier's internal processing unit and several sensor devices. In the aerial sensor system setup, the Raspberry Pi serves to aggregate carrier and sensor devices by running the real-time sensor data software framework in a Linux operating system environment.

In order to sense climatic conditions, a combined temperature and humidity sensor was connected to the Raspberry Pi's GPIO pins and interfaced via the Inter-Integrated Circuit (I^2C) bus. This Hygrochip Digital Humidity Sensor HYT-221 (IST AG, Wattwil, Switzerland) operates in temperatures ranging from -40 °C to 125 °C, and guarantees an accuracy of ±0.2 °C for common observations ranging from 0 °C to 60 °C. Humidity measurements range from 0% relative humidity (rH) to 100% rH, whereas the accuracy level decreases from ±1.8% rH, ranging from 0% rH to 80% rH, down to ±4.0% rH when exceeding 80% rH.

In addition to the combined temperature and humidity sensor, a standard c270 Logitech HD Webcam (Logitech S.A., Morges, Switzerland) was connected to one of the Raspberry Pi's USB ports to capture images during the flight mission. The focus of the camera's lens is fixed and suitable for distances beyond 0.4 m, whereas the image resolution is adjustable from 1,280×720 pixels, for streaming videos, up to 3 megapixels (MP), for capturing single images.

Furthermore, the Raspberry Pi was connected to a wireless local area network (WLAN) via a TL-WN822N Wireless USB Adapter (TP-LINK Technologies Co., Ltd., Shenzhen, China). The adapter operates the Institute of Electrical and Electronic Engineers (IEEE) 802.11b/g/n WLAN standards at frequencies ranging from 2.4 GHz to 2.4835 GHz.

The WLAN was setup by a WBR-3406TX 11g Wireless AP Router (Digital Data Communications GmbH, Dortmund, Germany), operating IEEE 802.11b/g WLAN standards.

This router was placed next to the base receiver station, a Lenovo ThinkPad Edge E325 notebook (Lenovo Group Limited, Hong Kong), which was used to generate user-defined waypoint routes and, moreover, operated as client for the reception and storage of all incoming data, broadcasted by the Raspberry Pi.

The carrier platform, with the mounted hardware components and a diagram of the communication between the components are illustrated in Figure 1.

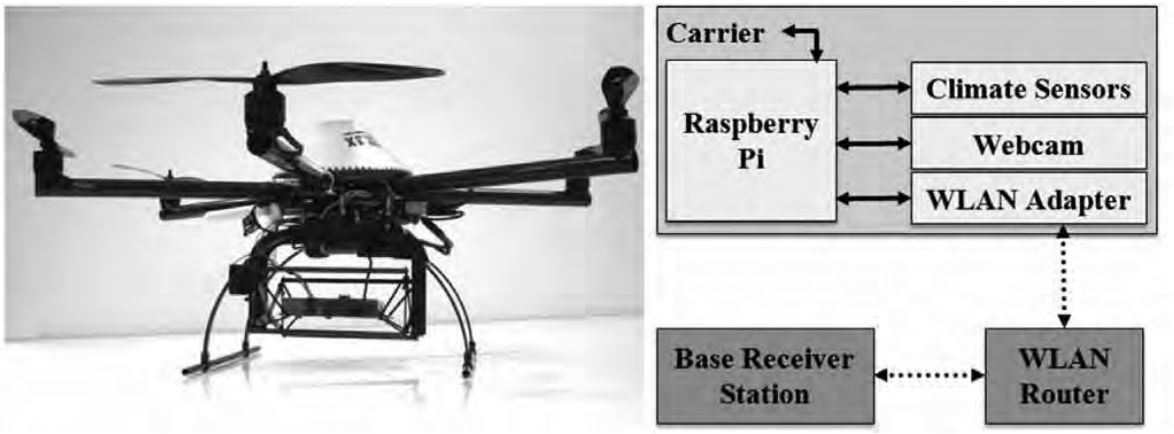

Figure 1. Modified Mikrokopter *'Hexe'* with attached Raspberry Pi, HYT-221 climate sensor, c270 webcam and TL-WN822N WLAN adapter (left). Schematic overview of the communication structure between the components (right).

Software framework

The multi-purpose software framework was developed to provide functionality for the five most important real-time requirements: sensor device control, sensor data retrieval, sensor data fusion, sensor data logging and sensor data broadcasting.

To meet these requirements, the framework's architecture was based on a modular concept. A core control routine initializes and runs the framework. This core routine co-ordinates several input and output plug-ins, which are registered at program start-up. Each plug-in is invoked by the core routine and is executed in an individual thread. The core routine then controls thread execution and memory access, queries data which is gathered by input plug-ins, and provides data to the output plug-ins for further processing and transmission. Basically, input plug-ins define communication with attached sensor devices, control the devices and make measured data available to the core routine. Output plug-ins, in contrast, retrieve data from the core routine and process them.

The aforementioned architecture was implemented in the C/C++ programming language and compiled for the Raspberry Pi's processor architecture. Figure 2 shows the individual modules of this architecture. The prototype software framework contains an input plug-in to request the carrier's navigation information at a rate of 4 Hz, a second one to request the combined temperature and humidity sensor data at a rate of 4 Hz, and a third one to capture webcam images with a resolution of 1,280×960 pixels at a rate of 2 Hz. An output plug-in collects this data at a predefined rate of 2 Hz, fuses the data to compact data tuples, logs these tuples to the Raspberry Pi's storage and, in addition, broadcasts these tuples over the wireless network to the base receiver station for subsequent processing or storage on the ground device.

Micro-climate field test

For the evaluation of the prototype aerial sensor system, an example mapping of micro-climate conditions was carried out at a research field at the University of Hohenheim, Stuttgart, Germany. The research field covers an area of approximately 0.5 ha and was sampled at altitudes of 5 m, 25 m and 50 m above ground. The aforementioned sensors were used to map temperature, humidity and capture aerial images. The sensor data software framework gathered, fused, logged and transmitted the data through a wireless interface to a base receiver station.

The post-mission processing was done with open source software, released under free license schemas: Hugin, a panorama creation software, and referenced using Quantum GIS (QGIS), a geographic information system (GIS). The acquired climate data was analysed in R, a statistical

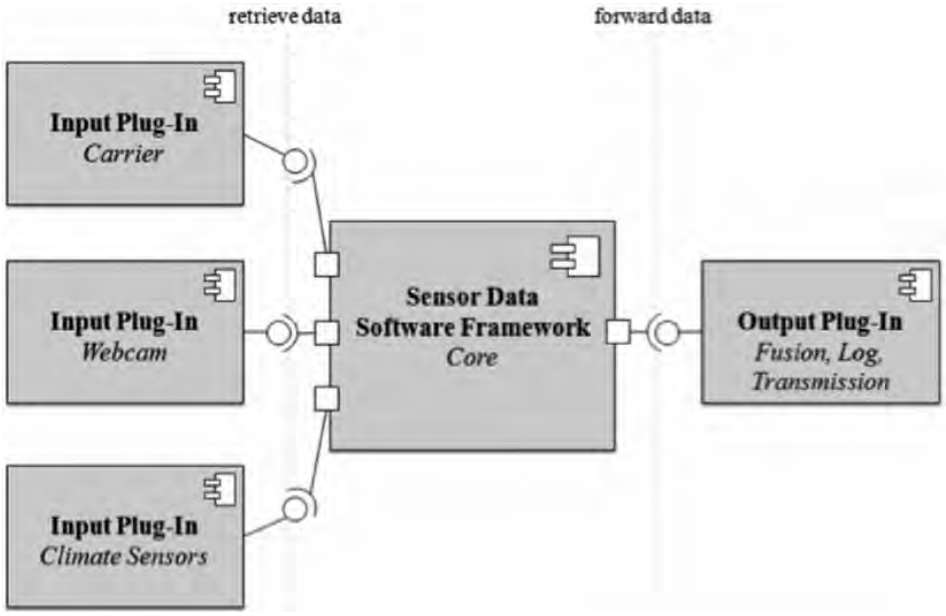

Figure 2. Component diagram of the modular software framework architecture with the core controlling routine, interfacing three input plug-ins for each connected sensor device and one output plug-in for data fusion, logging and transmission.

software environment and programming language, and subsequently processed and visualized in QGIS as a spatially-interpolated multi-layer map.

Results

During the entire field test, the software framework performed as expected. Every sensor was successfully accessed, given tasks and read out. The output plug-in generated all data sets, which were logged both on the Raspberry Pi and the base receiver station. Inconsistencies in data, either caused by system errors or by package loss through wireless transmission, were not observed.
The hardware expenses for the mounted equipment are listed in Table 1. The total cost of the equipment was 127 €, which is considered to be easily affordable. Since open source software was used for post-mission processing, no software expenditure was incurred.
The field test generated three different data sets for altitude levels of 5 m, 25 m and 50 m. Each set contained position, altitude, temperature and humidity information, sampled at a rate of 2 Hz. Arithmetic means and root mean square errors (RMSE) were calculated for each flight level and are outlined in Table 2. The absolute accuracy was not tested against data from a professional weather station. As expected, temperature decreased with height above ground dropping from 3.8 °C at an altitude of 5 m to 2.5 °C at 50 m. On the other hand, relative humidity increased slightly from 66.7% at 5 m to 69.7% at an altitude of 50 m.

Table 1. Hardware expenses, disregarding basic setup costs for the carrier platform, base receiver station and remote control. Prices are the projects' acquisition costs. (08/2012).

Item	Raspberry Pi Computer	HYT-221 Climate	c270 Webcam	TL-WN822N Adapter	WBR-3406TX Router	Total
Cost (€)	33	23	25	16	30	127

Table 2. Arithmetic mean and RMSE values for temperature and humidity measurements, subdivided according to their altitude level.

Altitude level (m)	5	25	50
Temperature (°C)	3.8±0.5	3.0±0.2	2.5±0.1
Humidity (rH)	66.7±3.3%	68.0±1.2%	69.7±0.5%

An example of the outcome of the multi-layer map is presented in Figure 3. The left side illustrates the geographically referenced aerial image, stitched from low-resolution webcam images, which were captured at an altitude of 50 m. The right side shows two inverse distance weighted (IDW) interpolated maps for temperature and relative humidity distribution, sensed at an altitude of 5 m.

Discussion

Regarding the software implementation, the micro-climate field test showed the framework's ability to meet the specified requirements of real-time functionality. Input plug-ins successfully controlled the attached sensor devices and, additionally, managed the sensor data retrieval. The implemented output plug-in fused all input sensor data, logged it and broadcast it to the base receiver station.
The software framework proved its applicability for the generation of location-based sensor data from a low-altitude aerial platform, aiming at post-mission analysis for the derivation of features that identify spatial variability, as required by precision farming operations.
All auxiliary hardware components, which were used along with the basic setup, were easily and broadly available and were acquired for a sum of 127 €. The potential of improving control and

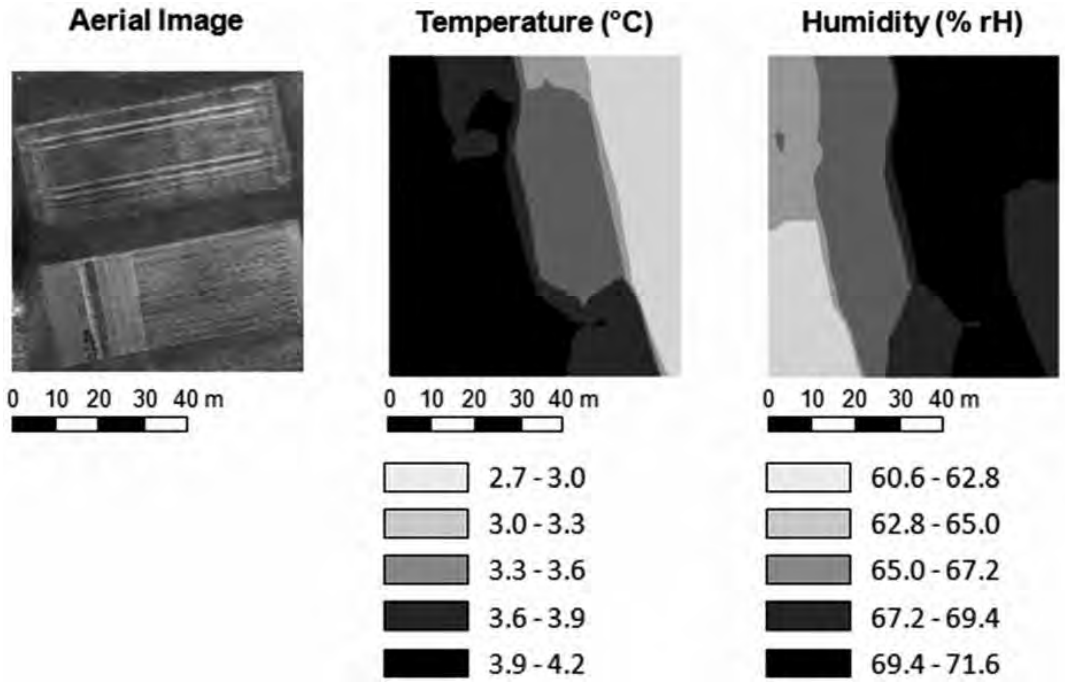

Figure 3. Example layers of a multi-layer map, created with QGIS, showing a referenced aerial image, captured by a webcam at an altitude of 50 m (left), an interpolated temperature (middle) and relative humidity map (right) at 5 m altitude, derived from the climate sensor data.

functionality between carrier platforms and sensors was achieved and demonstrated even with this low-cost equipment.
The results of the micro-climate use case indicate that low-cost, and therefore less efficient, sensor devices are capable of retrieving microclimatic data. The repeatability of these data needs to be examined along with their accuracy compared with ground truth values. It can be assumed that low-cost sensors provide potential to measure basic parameters for mapping of micro-climate conditions. Even though the measured parameters might not be highly accurate, they can be used to identify trends.

Future work

In a prospective software revision phase, improvements will be done on implementing accurately timed fusion algorithms, which will be adapted to meet individual mission requirements. Moreover, improvements will be performed, focusing on constant reduction of post-mission efforts. Among others, these improvements include advanced tasking mechanisms for the sensors and the carrier platform, as well as on-board real-time data evaluation and correction of the measurements. Additionally since the framework provides communication with a ground based system, monitoring of the progress and fusion of the data with ground sensors can be achieved.
As the software framework proved its potential to improve performance for close-range aerial remote sensing systems, it will be used in future research on providing site-specific information for precision farming applications. Utilising spectral in-field information from reflected radiation, e.g. Leaf Area Index, Red Edge Inflection Point and Normalized Difference Vegetation Index, these applications will focus on crop fertilisation and weed suppression. Therefore, more sophisticated sensor devices will be integrated into the framework for capturing images at higher resolution and sensing hyper-spectral information with spectrometers.

Conclusions

This work shows the first steps in developing a sophisticated low-cost agricultural aerial sensor system. The approach offers real-time sensor measurements, sensor data fusion, processing, transmission and storage. It allows UAVs to overcome their simple carrier functionality to intelligent sensor systems.

Acknowledgements

The authors acknowledge the Carl-Zeiss-Foundation (Carl-Zeiss-Stiftung) for funding this work as part of the collaborative project SenGIS at the University of Hohenheim, Stuttgart, Germany.

References

Berni, J. A. J., Zarco-Tejada, J. A., Suárez, L., González-Dugo, V. and Fereres, E. 2009. Remote sensing of vegetation from UAV platforms using lightweight multispectral and thermal imaging sensors. In: (Eds.) Heipke, C., Jacobsen, K., Müller, S., Sörgel, U., ISPRS Hannover Workshop High-Resolution Earth Imaging for Geospatial Information: ISPRS Archives – Volume XXXVIII-1-4-7/W5.

Grenzdörffer, G. J., Engel, A. and Teichert, B. 2008. The photogrammetric potential of low-cost UAVs in forestry and agriculture. In: The International Archives of the Photogrammetry, Remote Sensing and Spatial Information Sciences, ISPRS Congress. Part B1, 1207-1213.

Hruska, R., Mitchell, J., Anderson, M. and Glenn, N. F. 2012, Radiometric and Geometric Analysis of Hyperspectral Imagery Acquired from an Unmanned Aerial Vehicle. Remote Sensing 4 2736-2752.

Huang, Y., Thomson, S. J., Lan, Y. and Maas, S. J. 2010. Multispectral imaging systems for airborne remote sensing to support agricultural production management. International Journal of Agricultural and Biological Engineering 3 (1) 50-62.

Hunt, E. R., Hively, W. D., Fujikawa, S. J., Linden, D. S., Daughtry, C. S. T. and McCarty, G. W. 2010. Acquisition of NIR-Green-Blue Digital Photographs from Unmanned Aircraft for Crop Monitoring. Remote Sensing 2 290-305.

Kuhnert, L., Müller, K., Ax, M. and Kuhnert, K.-D. 2012. Object localization on agricultural areas using an autonomous team of cooperating ground and air robots. In: The International Conference of Agricultural Engineering CIGR-Ageng2012.

Lelong, C. C. D., Burger, P., Jubelin, G., Roux, B., Labbé, S. and Baret, F. 2008. Assessment of Unmanned Aerial Vehicles Imagery for Quantitative Monitoring of Wheat Crop in Small Plots. Sensors 8 3557-3585.

Primicerio, J., Di Gennaro, S. F., Fiorillo, E., Genesio, L., Lugato, E., Matese, A. and Vaccari, F. P. 2012. A flexible unmanned aerial vehicle for precision agriculture. Precision Agriculture 13 517-523.

Xiang, H. and Tian, L. 2011. Method for automatic georeferencing aerial remote sensing (RS) images from an unmanned aerial vehicle (UAV) platform. Biosystems Engineering 108 104-113.

3 Combined Spectral and Spatial Modeling of Corn Yield Based on Aerial Images and Crop Surface Models Acquired with an Unmanned Aircraft System

Geipel, J., J. Link and W. Claupein, 2014. Combined Spectral and Spatial Modeling of Corn Yield Based on Aerial Images and Crop Surface Models Acquired with an Unmanned Aircraft System. *Remote Sensing*, 6(11):10335–10355.

Stafford (2000) addressed not only the automation of sensor systems (see Section 2) and the usage of standardized data for information extraction by expert systems (see Section 5), but also an evolution of algorithms and strategies for localized management to overcome the barriers for PF adoption. For the determination of input factors like nutrients, pesticides, and water crop management relies heavily on the farmers experience from earlier years, estimates of actual crop status, and predictions of expected yields.

This publication demonstrates a modern approach to support farmers to predict their within-field yield potential in corn. Earlier studies have already demonstrated that corn height and grain yield are highly intercorrelated. As structure from motion techniques allow to derive 3D CSMs from aerial imagery, the prototype UAS was equipped with a consumer grade digital camera and tested in a corn field at early- to mid-season growth stages. The image processing resulted in high resolution CSMs and ortho-rectified RGB images with a spatial resolution of up to 2 $cm\ px^{-1}$. The orthoimages were processed to vegetation indices and used for (i) a pixel-based crop/non-crop classification and (ii) an estimation of the crop coverage factor. Different strategies to derive representative crop heights from the CSMs were tested and linear regression models were set up to investigate their yield prediction abilities. The study shows that an approach, which utilizes a combination of CSM height, classification information and crop coverage, showed good results with inaccuracies of only 8.8 % for mid-season yield prediction. Moreover, the test indicated that the modeling strategy depends on the growth stage. With on-going plant development, the need for high resolution imagery and combined methods decreases as progressive canopy closure eliminates the visible spatial and spectral heterogeneity in the crop stand.

Remote Sens. **2014**, *11*, 10335-10355; doi:10.3390/rs61110335

OPEN ACCESS

remote sensing

ISSN 2072-4292

www.mdpi.com/journal/remotesensing

Article

Combined Spectral and Spatial Modeling of Corn Yield Based on Aerial Images and Crop Surface Models Acquired with an Unmanned Aircraft System

Jakob Geipel *, Johanna Link and Wilhelm Claupein

Institute of Crop Science, University of Hohenheim, Fruwirthstr. 23, Stuttgart 70599, Germany; E-Mails: Johanna.Link@uni-hohenheim.de (J.L.); Wilhelm.Claupein@uni-hohenheim.de (W.C.)

* Author to whom correspondence should be addressed; E-Mail: jakob.geipel@uni-hohenheim.de; Tel.: +49-711-459-22938; Fax: +49-711-459-22297.

External Editor: Arko Lucieer, Pablo J. Zarco-Tejada, Uwe Rascher, Georg Bareth and Prasad S. Thenkabail

Received: 19 May 2014; in revised form: 26 September 2014 / Accepted: 10 October 2014 / Published: 27 October 2014

Abstract: Precision Farming (PF) management strategies are commonly based on estimations of within-field yield potential, often derived from remotely-sensed products, e.g., Vegetation Index (VI) maps. These well-established means, however, lack important information, like crop height. Combinations of VI-maps and detailed 3D Crop Surface Models (CSMs) enable advanced methods for crop yield prediction. This work utilizes an Unmanned Aircraft System (UAS) to capture standard RGB imagery datasets for corn grain yield prediction at three early- to mid-season growth stages. The imagery is processed into simple VI-orthoimages for crop/non-crop classification and 3D CSMs for crop height determination at different spatial resolutions. Three linear regression models are tested on their prediction ability using site-specific (i) unclassified mean heights, (ii) crop-classified mean heights and (iii) a combination of crop-classified mean heights with according crop coverages. The models show determination coefficients R^2 of up to 0.74, whereas model (iii) performs best with imagery captured at the end of stem elongation and intermediate spatial resolution (0.04 m·px^{-1}). Following these results, combined spectral and spatial modeling, based on aerial images and CSMs, proves to be a suitable method for mid-season corn yield prediction.

Remote Sens. **2014**, *11* **10336**

Keywords: corn; crop coverage; crop height; crop surface model; CSM, UAS; yield

1. Introduction

Corn (*Zea mays* L.) biomass and grain yields vary depending on site, climatic conditions and management decisions. Moreover, variation is likely to occur within fields. Following the idea of Precision Farming (PF), the identification of within-field spatial and temporal variability shows potential to support crop management concepts to meet much of the increasing environmental, economic, market and public pressures on arable agriculture [1]. Management strategies account for (i) environmental issues by adapting the input factors to the demand of the crop and, thus, avoid over- or under-application [2,3], (ii) economic issues by calculating within-field net returns [4] and (iii) possibilities to improve the control and influence of the quality of the product [5].

Yield estimations prior to harvest play a key role in the determination of input factors, like nutrients, pesticides and water, as well as for the planning of upcoming labor- and cost-intensive actions, like harvesting, drying and storage. In addition, bioenergy- and other corn-related industries benefit from these estimations, too [6]. Commonly, farmers use different methods for prediction. Coarse estimations are built on the farmer's expert knowledge. Better estimations can be drawn from destructive sampling procedures in representative areas [7]. Unfortunately, destructive sampling is very labor-and cost-intensive work. Another approach is using yield maps, providing information about spatial and temporal variability of yields in previous years [8]. Although yield maps give some hints at within-field yield potential, they have limitations in explaining current growing conditions. Thus, reliable information about actual within-field yield estimations is usually drawn from more promising methods. Besides using linear regression models with additional information on crop management [6] or weather and soil attributes [9], several studies demonstrate the power of crop growth models to predict yield [10,11]. Although crop growth models return good estimates, their practical applicability may be limited due to the need of extensive input data for implementation. On a local and regional level, remote sensing products are quite common for estimating corn yield [12–14]. For a further increase in accuracy, some authors also combine actual remote sensing data and crop growth models [15,16]. Consequently, PF data has potential to improve crop development and yield prediction with smart management strategies and yield models.

With the upcoming of cheap and handy Unmanned Aircraft Systems (UASs), remotely-sensed data at high spatial and temporal resolutions have become more and more affordable [17]. Many researchers focus on RGB, multi-, hyper-spectral and thermal imaging techniques for crop monitoring [18–20], crop and weed discrimination [21,22] or on the generation of Digital Elevation Models (DEMs) [23–26]. Despite that, less research has been conducted on 3D Crop Surface Models (CSMs) [27–29] or on the possibilities of a combined analysis of both 3D and spectral information [30–32].

This study focuses on modeling of corn grain yield with a combined spectral and spatial analysis of aerial imagery. Standard imagery, which has been captured by a RGB consumer camera, the most common sensor used on UASs, serves as the data basis. Although RGB imagery carries limited spectral information compared to more sophisticated types, like multi-, hyper-spectral and thermal ones, its high

Remote Sens. **2014**, *11* **10337**

spatial resolution allows one to create detailed CSMs for further crop investigation [28]. In addition to that, spectral information from RGB imagery can be used to determine positions of crops and estimate site-specific crop coverage factors by applying basic methods for crop/non-crop separation [33–35].

Recent studies found a high correlation of corn plant height and corn grain yield at early- to mid-season growth stages [36–38]. Yin *et al.* [37] also showed that linear regression models for the prediction of corn grain yield may be the preferred ones, because of their simplicity. Based on these findings, this study's objective was to assess the potential of CSMs to predict corn grain yield at early- to mid-season growth stages by using mean crop heights and different linear regression models. The underlying hypotheses were to predict corn grain yield with simple linear regression models, building on plot-wise mean crop height as the predictor variable. The mean crop heights were generated in two ways, with and without respect to previously classified crop/non-crop pixels. Additionally, a multiple linear regression model was set up, including the crop coverage factor as a second predictor variable to improve prediction accuracy.

2. Materials and Methods

2.1. Experimental Setup

Ihinger Hof (48.74°N, 8.92°E), a research station of the University of Hohenheim, was chosen to serve as an experimental site for a field trial to predict corn grain yield by aerial imagery and crop surface models. The regional climate is categorized as a temperate climate with an annual average temperature of 7.9 °C and an average precipitation of 690 mm.

Figure 1. Overview of the two-factorial field trial in corn with 64 plots of a size of 36 × 6 m each. Four sowing densities (8–11 seeds·m^{-2}) were tested at four different levels of nitrogen fertilization (50, 100, 150 and 200 kg·N·ha^{-1}) in a setup with four replicates.

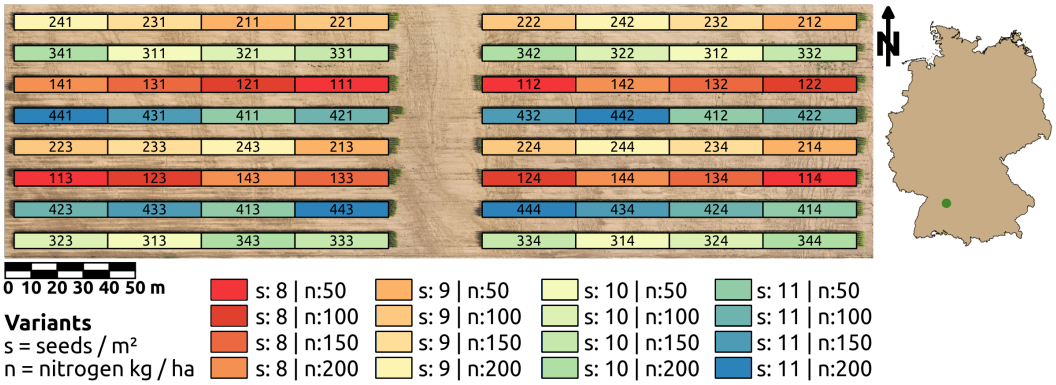

A two-factorial field trial was laid out in a common randomized split-plot design on 27 May 2013, with the corn cultivar "NK Ravello". Four sowing densities (8–11 seeds·m^{-2}) were tested at four different levels of nitrogen fertilization (50, 100, 150 and 200 kg·N·ha^{-1}) in a setup with four replicates. This resulted in 64 plots of a size of 36 × 6 m each and a total trial size of 1.38 ha (see Figure 1). Row spacing was set to 0.75 m, whereas seed spacing was adjusted according to the desired density

level (0.115–0.158 m). Harvest and determination of corn grain yield with a moisture content of 14% took place on 28 October 2013, with a Global Navigation Satellite System (GNSS)-assisted combine harvester.

2.2. UAS and Sensor Setup

In this field experiment, a modified MikroKopter (MK) Hexa XL served as the aerial carrier platform to conduct sensor measurements [39]. Equipped with standard MK navigation sensors (Inertial Measurement Unit (IMU) and differential GNSS receiver), it is able to perform user-defined waypoint flights. Assembled with a payload of 1 kg and a lithium polymer battery with a capacity of 5000 mAh, this UAS operates approximately 10 min at an altitude level of 50 m above ground. With an additionally integrated Raspberry Pi Model B computer, it merges its navigation information with observations from attached sensor devices on-the-fly [40,41].

As the imaging sensor, a Canon Ixus 110 IS RGB consumer camera was attached to the UAS [42]. The camera's sensor resolution was set to a maximum of 4000 × 3000 pixels to achieve a ground resolution of approximately 0.02 m·px^{-1} at a flight altitude of 50 m. The camera was configured to predefined focal length (5.0 mm), aperture (f/2.8) and exposure time (1/500, 1/800 or 1/1000 s), whereas image triggering was software-controlled via a USB connection with the Raspberry Pi.

2.3. Measurements

Flight missions were performed on three dates during early- and mid-season crop development (beginning of stem elongation, end of stem elongation and end of emergence of inflorescence), referring to Zadoks' scale's Z32, Z39 and Z58 [43]. In each mission, aerial images were captured at a scheduled flight altitude of 50 m with an intended overlap of 80% in-track and 60% cross-track to ensure image redundancy. All images have been captured with a nadir view of direction, in clear skies and around noon. Each flight mission produced about 400 images covering all experimental plots with a ground resolution of approximately 0.02 m·px^{-1}. An overview of the flight missions is given in Table 1.

Table 1. Overview of performed flight missions at Zadoks' scale's crop growth stages Z32, Z39 and Z58 and the number of images for subsequent processing, flight altitude, approximate image ground resolution, mission time, illumination and wind speed.

Date	Growth Stage	Images	Scheduled Altitude (m)	Ground Resolution (m·px^{-1})	Time	Illumination	Wind (m·s^{-1})
17/07/2013	Z32	253	50	0.02	11–12 am	clear sky	1
01/08/2013	Z39	198	50	0.02	10–11 am	clear sky	2
15/08/2013	Z58	268	50	0.02	10–11 am	clear sky	2

2.4. Image Processing

Prior to processing, the selected original images were reduced in resolution to create four additional datasets of imagery at ground resolutions of 0.04, 0.06, 0.08 and 0.10 m·px^{-1}. These artificial datasets were used to simulate corn grain yield prediction performance at different spatial resolution levels of aerial imagery. Regarding the shape and structure of corn, as well as the applied plant spacing of 0.115 to 0.158 m and a row spacing of 0.75 m, the computed ground resolutions lie somewhere within the leaf and canopy level. As a consequence, high ground resolutions are expected to cover fine structures (leaf level), whereas low resolutions are expected to cover coarse structures (canopy level). The following image processing routine was performed for each dataset and crop growth stage individually.

2.4.1. Orthoimage and Digital Elevation Model

Imagery and corresponding UAS navigation information were used to generate orthoimages and DEMs with the help of the 3D reconstruction software Agisoft PhotoScan 1.0.1 [44]. In a first step of processing, all selected images were aligned, mosaicked and geo-referenced by the software's feature matching and Structure from Motion (SfM) algorithms. In a similar way as the popular Scale-Invariant Feature Transform (SIFT) approach from Lowe [45], feature detection was performed on each image to generate descriptors for image correspondence detection. Based on the correspondences and initial GNSS image locations, the SfM algorithm reconstructed the 3D scene, camera positions and orientations [46]. In a second step, a DEM was extracted from the 3D scene by applying a natural neighbor interpolation [47]. This DEM represents the geo-referenced surface of the experimental site and is based on altitude values relative to the GNSS' reference ellipsoid. Generally, absolute crop heights are calculated by subtracting a second DEM, a so-called Digital Terrain Model (DTM), representing the surface of the ground relative to the same reference ellipsoid as the DEM (see Figure 2).

Figure 2. Visualization of DEM and DTM altitudes relative to a commonly shared GNSS reference ellipsoid (red surface). While the DEM represents a surface model of the experimental site (green surface), the DTM represents the surface of the ground. The DTM was approximated by interpolation of ground classified DEM pixels (yellow surface). Absolute crop heights are derived by subtraction of the two surface representations.

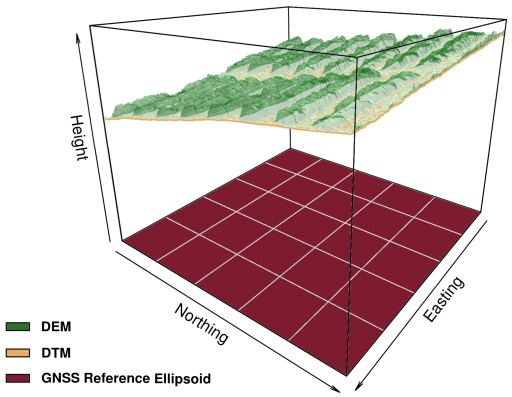

Therefore, in a third step, a DTM was inferred from the 3D scene by excluding non-ground pixels, which have been previously classified using the software's automatic classification routine. To ensure the classification of real ground points, the point cloud was subdivided into cells of 7 × 7 m, and each cell's lowest point was used for triangulation of a coarse initial DTM. After that, the initial DTM was densified by checking whether each remaining point meets the following two requirements: the vertical distance to the DTM-surface lies within a predefined buffer of 0.03 m, and at least one of the vectors to a ground-classified point intersects the DTM-plane with less than a predefined angle of 15°. In a last step, a mosaicked orthoimage, DEM and DTM were exported to three individual GeoTiff raster files for subsequent processing.

2.4.2. Crop Surface Model and Vegetation Indices

Further processing was performed with the statistical computation software, R [48–50]. The exported GeoTiff raster files were combined to a single raster stack object containing red, green, blue, DEM and DTM information as individual raster layers. A CSM raster layer was generated by pixel-wise subtraction of DTM layer altitudes from DEM layer altitudes and was added to the raster stack object.

In addition to that, three simple Vegetation Indices (VIs) were derived from the RGB bands containing the pixels' greenness information in relation to their redness and/or blueness. The Excess Green Index (ExG), Vegetation Index Green (VIg), which is sometimes also referred to as the Normalized Green-Red Difference Index (NGRDI), and an adapted broadband variant of the Plant Pigment Ratio (PPRb) were selected as appropriate VIs to approach a detailed separation of crop and soil pixels [33,34,51,52]. Table 2 lists these VIs' calculation formulas, which were performed on the raster stack object individually.

Table 2. Vegetation indices applied on the RGB images for pixel based crop/soil separation. The Excess Green Index (ExG) accounts for a combination of green and red, as well as green and blue reflection differences. The Vegetation Index Green (VIg) (sometimes also referred to as the Normalized Green-Red Difference Index (NGRDI)) represents a normalized green and red difference, whereas the adapted broadband variant of the Plant Pigment Ratio (PPRb) makes use of a normalized green and blue difference.

Index Reference	Explanation	Formula
ExG Woebbecke *et al.* [33] & Meyer *et al.* [51]	Excess Green Index	$2 \times R_{green} - R_{red} - R_{blue}$
VIg Gitelson *et al.* [34]	Vegetation Index Green	$\frac{R_{green} - R_{red}}{R_{green} + R_{red}}$
PPRb based on Metternicht [52]	Plant Pigment Ratio	$\frac{R_{green} - R_{blue}}{R_{green} + R_{blue}}$

2.4.3. Plot-Wise Feature Extraction

Features were extracted by a self-developed automatic routine. First, field trial plot information was imported as a polygonal shapefile. For this analysis, plot size was reduced to rectangles of 9 × 6 m around the original plots' centers to account for plot boundary effects, e.g., sowing or fertilization inaccuracies. Second, a shapefile containing harvested corn yield information was imported, and mean corn yields were determined for each individual plot. Third, mean plot heights were calculated using height information from the CSM layer. Fourth, for each VI layer, all pixels that fall inside a plot were extracted, and five different thresholds were computed on the selected pixels' aggregated histogram based on the method of Ridler and Calvard [53] and Kort [50]. Consequently, VI layer pixels were classified as non-crop pixels in the case that the pixels' values were below the defined thresholds and as crop pixels in the case that they were above the defined thresholds, respectively (see Figure 3).

Figure 3. VI-based Ridler thresholding by the example of a 4 × 4 m sub-sample of plot 413 with a sowing density of 11 seeds·m^{-2} and nitrogen application of 50 kg·N·ha^{-1}. The upper left corner shows the RGB orthoimage, which is displayed at a ground resolution of 0.04 m and at crop growth stage Z39. The second image in the upper row shows the ExG layer, which was derived from the RGB orthoimage. Based on the ExG layer's histogram, five different thresholds were computed. Threshold r_3 is the original Ridler threshold, whereas the other thresholds represent four variations on the Ridler method (upper right corner). The remaining images show the ExG layer's classification (green = crop, yellow = soil) based on the five thresholds. In this example, threshold r_3 and r_4 seem to classify best. Thresholds r_1 and r_2 seem to overestimate crop coverage, while r_5 seems to underestimate crop coverage.

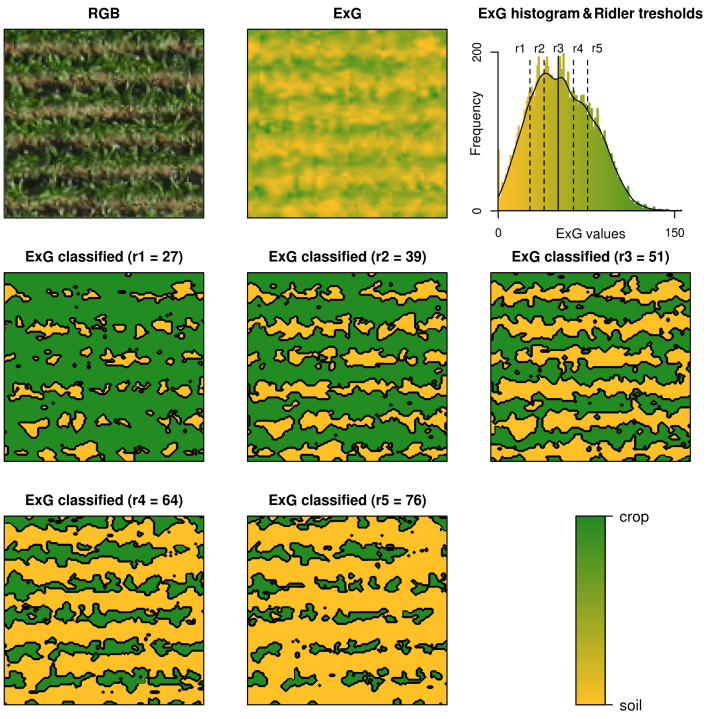

Remote Sens. **2014**, *11* **10342**

Fifth, for each VI layer and its five identified thresholds, mean plot heights were calculated using the CSM layer height information solely from crop-classified pixels (see Figure 4). Sixth, for each VI layer and its five identified thresholds, plot crop coverage was computed by dividing the number of crop-classified pixels by the total number of pixels in each plot.

Figure 4. Mean crop height computation using the example of a 4 × 4 m sub-sample of plot 413 with a sowing density of 11 seeds·m^{-2} and nitrogen application of 50 kg·N·ha^{-1}. The lower part of the figure shows a stack of the RGB orthoimage and the ExG layer classification based on threshold r_4 at a ground resolution of 0.04 m and at crop growth stage Z39. The upper part shows the corresponding CSM layer height information as a 3D representation, colored by the ExG-classification. Mean crop height was calculated by the crop-classified CSM layer heights only and is displayed as a semi-transparent plane.

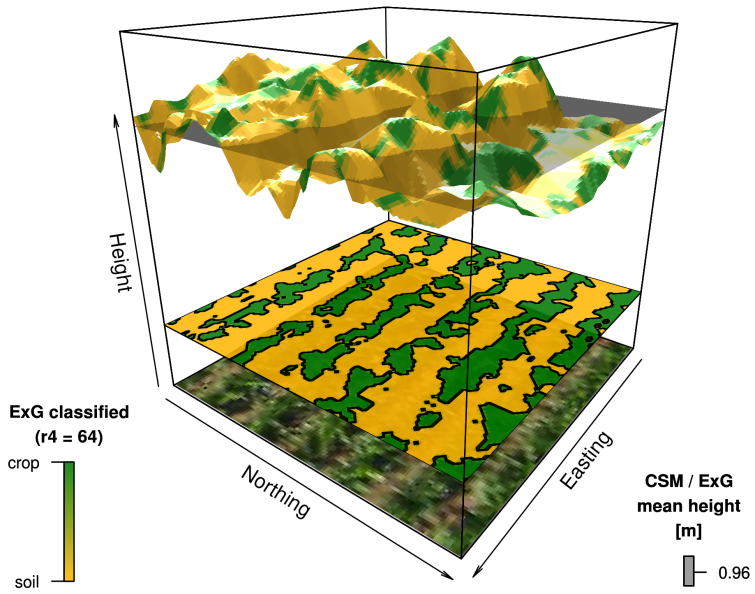

2.5. Modeling Strategy

In the last step of processing, the extracted features were used to model corn grain yield with three different strategies. Based on the findings of Yin *et al.* [37] that all investigated regression models predict sufficiently well, standard linear regression models were set up for prediction. Assuming that Y_i is the harvested corn grain yield, $\overline{H}_{irs}$ is the i-th mean plot height, regardless of any pixel classification, at the r-th ground resolution level and the s-th growth stage, whereas b_0 and b_1 are the regression coefficients. Equation (1) shows a simple linear regression model for corn grain yield prediction, forming strategy S_1.

$$Y_i = (b_0 + b_1 \times \overline{H}_{irs}) + \varepsilon_{irs} \quad (1)$$

Strategy S_2 was laid out in the same way as strategy S_1, except $\overline{H}_{irstv}$ representing the i-th mean plot height calculated from pixels, which were classified as crop by using the v-th VI layer and the t-th Ridler threshold estimate at the r-th ground resolution and s-th growth stage (Equation (2)).

$$Y_i = (b_0 + b_1 \times \overline{H}_{irstv}) + \varepsilon_{irstv} \quad (2)$$

The third strategy S_3 is a multiple linear regression approach, extending strategy S_2. This approach accounts for a second predictor variable C_{irstv} representing the i-th plot crop coverage factor, which was computed by the v-th VI layer, and the t-th Ridler threshold estimate at the r-th ground resolution and the s-th growth stage (Equation (3)).

$$Y_i = (b_0 + b_1 \times \overline{H}_{irstv} + b_2 \times C_{irstv}) + \varepsilon_{irstv} \quad (3)$$

While the first two strategies follow the approach of Yin *et al.* [37], strategy S_3 also considers the crop coverage factor as an additional predictor for expected corn grain yield.

2.6. Statistical Analysis

Statistical analysis was conducted with the statistical computation software, R. The field trial was analyzed as a mixed model using a standard two-way analysis of variance (ANOVA) approach. All modeling strategies for corn grain yield prediction were tested with and without classification-based mean crop heights at all crop growth stages, ground resolutions, Ridler threshold estimates and deduced crop coverage factors. The prediction accuracy of the different modeling strategies was assessed by using R^2 determination coefficient values as quality indicators. Spatial visualization of predicted and harvested corn grain yield was carried out using the geographical information system QGIS [54].

3. Results and Discussion

3.1. Field Trial

The ANOVA showed a significant influence of nitrogen fertilization on corn grain yield. Significant influences of sowing density, as well as of the interaction of both factors were not detected. The non-significant influence of sowing density was not expected, but might have been caused by the small variability in the range of sowing density levels of 8–11 seeds·m^{-2}. Detailed results are not presented in the following.

3.2. Image Processing

The 3D reconstruction software, Agisoft PhotoScan 1.0.1, was able to perform image alignment and 3D scene reconstruction for all imagery datasets. Geo-referencing was based on camera location information, derived from GNSS and IMU data. Orthoimage, DEM and DTM computation succeeded for all imagery datasets. Resulting orthoimage ground resolution was at the level of input image ground resolution. As dense point cloud reconstruction is a very hardware-demanding task, the imagery used for DEM and DTM generation was downscaled by a factor of two to save processing time. Although

DEM and DTM were exported with the corresponding orthophoto's ground resolution, the underlying dense point cloud was built with less detail than theoretically possible.

As the produced DTMs are based on the interpolation of previously classified ground points, this method is generally prone to misclassification at dense crop stands and canopy closure. In these situations, only a small amount of ground points will be visible at all, weakening the reliability of the interpolation results. Moreover, some of the classified points may not represent the "real" ground, leading to an underestimation of crop heights. In a homogeneous field, a correction factor could compensate for this underestimation. In an inhomogeneous field, the correction factor would not be constant anymore. To avoid these problems, it is recommended to produce DTMs at sowing stage, without the need for classification and interpolation of large gaps.

Geo-referencing accuracy was assessed by the help of 24 Ground Control Points (GCPs), which were installed permanently and measured with RTK-GNSS equipment. Heavy rainfalls in July silted many of the GCPs. In addition, others have been destroyed by intensive mechanical weed control in between the corn strips. Unfortunately, the GCPs were not renewed before performing flight missions at Z39 and Z58. As a consequence, imagery from these stages lack accurate GCP information. Thus, accuracy assessment was performed on Z32 imagery, only.

Table 3. Resulting root mean squared errors (m) (RMSE) at ground control point (GCP) locations for indirectly (GCP-based) and directly (GNSS- and IMU-based) geo-referenced imagery at Z32 for all image ground resolutions.

Geo-Reference	**Coordinate Component**	**Ground Resolution (m·px^{-1})**				
		0.02	**0.04**	**0.06**	**0.08**	**0.10**
GCPs	Horizontal	0.058	0.063	0.084	0.089	0.082
	Vertical	0.068	0.059	0.051	0.046	0.075
GNSS & IMU	Horizontal	0.430	0.375	0.399	0.409	0.376
	Vertical	0.303	0.273	0.283	0.320	0.379

In addition to direct (GNSS- and IMU-based) geo-referencing, indirect (GCP-based) geo-referencing was conducted on Z32 imagery for enhanced CSM quality assessment. Table 3 lists the resulting root mean squared errors of a comparison of measured and computed GCP coordinates for both methods and all image ground resolutions at Z32. As expected, indirectly geo-referenced imagery showed smaller residuals than the directly geo-referenced one. Horizontal RMSEs for indirectly geo-referenced imagery ranged from 0.058 to 0.089 m, whereas vertical RMSEs ranged from 0.046 to 0.075 m. In contrast to that, horizontal RMSEs for directly geo-referenced imagery ranged from 0.375 to 0.430 m, whereas vertical RMSEs ranged from 0.273 to 0.379 m. The accuracies of both methods are in accordance with the findings of Turner *et al.* [55] and Ruiz *et al.* [56], although vertical accuracy performs slightly better than expected. GCP-based accuracy assessment for directly geo-referenced imagery at Z39 and Z58 was not performed. Nevertheless, comparison of identifiable field boundaries with those of Z32 did not show excessive horizontal accuracy errors for all resolutions.

The developed R-routine managed to calculate CSMs, VIs and all threshold variants for every imagery dataset. CSM quality was assessed by comparison of mean plot heights at Z32, derived from accurate

and indirectly geo-referenced imagery, with those derived from less accurate and directly geo-referenced imagery. Table 4 shows the resulting root mean squared errors for plot height comparisons, ranging from 0.024 m for high resolution imagery to 0.008 m for low resolution imagery. With a difference of 0.20 m in between the highest and lowest mean plot height at Z32, direct geo-referencing shows little influence on mean plot height computation. Unfortunately, independent reference measurements, e.g., manual height measurements, 3D laser scanning datasets or CSMs, derived by other SfM software packages, were not available to assess absolute CSM accuracy. Therefore, subsequent analyses and results are proven for this dataset, only.

Table 4. Resulting root mean squared errors (m) (RMSE) of comparing mean plot heights calculated from indirectly (GCP-based) and directly (GNSS- and IMU-based) geo-referenced imagery at Z32 for all image ground resolutions.

	Coordinate	Ground Resolution (m·px^{-1})				
Value	**Component**	**0.02**	**0.04**	**0.06**	**0.08**	**0.10**
Plot Height	Vertical	0.024	0.010	0.009	0.010	0.008

Horizontal alignment errors of directly geo-referenced imagery strongly influence the results of automatic feature extraction. To account for misalignment, the polygonal shapefile, containing this field trial's plot information, was realigned individually for all imagery at all growth stages and image ground resolutions.

The computed original Ridler thresholds r_3 were regarded as suitable for automatic separation of crop and soil, as well as most of the threshold variants r_2 and r_4. In contrast to that, threshold variants r_1 and r_5 showed results of crop overestimation at threshold r_1 and underestimation at threshold r_5, respectively (see e.g., Figure 3). However, mean plot heights $\overline{H}_{irstv}$ and crop coverage factors C_{irstv} were computed for all strategies at every threshold level r_{1-5} for subsequent comparison of prediction performance.

3.3. Modeling Strategy

All results of the applied corn grain yield prediction strategies are summarized in Table 5, whereas Figure 5 visualizes the most important findings. Strategy S_3 was evaluated for collinearity of its predictor variables, mean crop height and crop coverage. Critical collinearity at any crop growth stage was not found. As all strategies built on data from one growing period, leave-one-out cross-validation was conducted to evaluate each model's predictive quality. Table 6 shows the resulting root mean squared errors of prediction (RMSEP), ranging from 0.67 to 1.28 t·ha^{-1} (8.8% to 16.9%).

Crop growth stage Z32 was neglected in Figure 5, as none of the strategies resulted in R^2 determination coefficient values higher than 0.56. As crops were still small and stems were beginning to elongate, crops' leaves were not overlapping at this point in time. Lacking canopy closure, the prediction models had to account for information contained at the leaf level. Therefore, imagery with highest resolutions of 0.02 and 0.04 m·px^{-1} performed best and showed significant R^2 values. In contrast, lower resolution datasets did not provide much detail, resulting in low R^2 values. Strategy S_3 was generally able to significantly improve prediction accuracies of strategies S_1 and S_2 for all VIs by adding the crop

Remote Sens. **2014**, *11* **10346**

coverage factor as the second predictor variable. Although the highest resolution imagery of 0.02 m·px^{-1} performed best at this stage, even higher resolutions may be more appropriate for CSM and, thus, mean plot height generation. Reaching maximum R^2 values of 0.56 and considering additional environmental impacts on crop growth during the growing season, none of the applied strategies was assessed to be reliable for early-season corn grain yield prediction.

Figure 5. Resulting determination coefficients R^2 of modeling strategies S_{1-3} for all VIs and aerial image ground resolutions at crop growth stages Z39 and Z58. Grey values represent R^2 values for strategy S_1, whereas black values represent strategy S_2 at Ridler threshold r_3 and colored values represent strategy S_3 at Ridler threshold r_3, respectively. In addition to the R^2 values of strategies S_2 and S_3 at Ridler threshold r_3, minimum and maximum R^2 values of the four remaining threshold variants are indicated as range bars for every aerial image ground resolution individually.

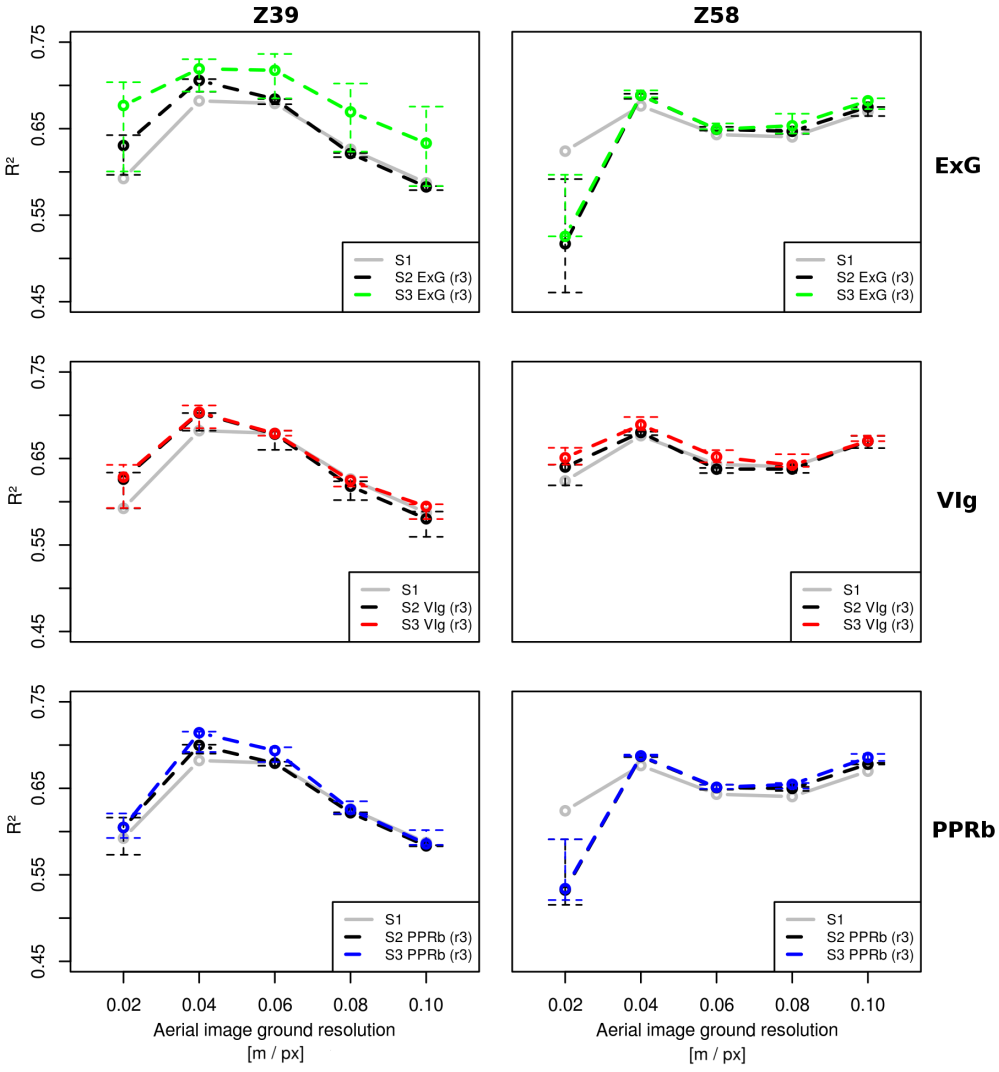

Remote Sens. **2014**, *11* **10347**

Table 5. The resulting determination coefficients R^2 of the prediction of corn grain yield by applying strategies S_{1-3} for all combinations of VIs, aerial image ground resolutions, crop growth stages and computed Ridler thresholds. Significance codes for predictor variable crop height are represented as * in superscript, whereas significance codes for predictor variable crop coverage factor are represented as $_*$ in subscript (appearing only in strategy S_3).

Ground Res. (m·px^{-1})			**ExG**					**VIg**					**PPRb**				
Z	**S$_x$**	**r$_x$**	**0.02**	**0.04**	**0.06**	**0.08**	**0.10**	**0.02**	**0.04**	**0.06**	**0.08**	**0.10**	**0.02**	**0.04**	**0.06**	**0.08**	**0.10**
Z32	S_1		0.48***	0.26***	0.12**	0.05	0.09*	0.48***	0.26***	0.12**	0.05	0.09*	0.48***	0.26***	0.12**	0.05	0.09*
Z32	S_2	r_1	0.54***	0.27***	0.12**	0.05	0.09*	0.53***	0.25***	0.11**	0.05	0.08*	0.46***	0.25***	0.11**	0.05	0.09*
Z32	S_2	r_2	0.55***	0.24***	0.11**	0.04	0.08*	0.55***	0.21***	0.09*	0.03	0.07*	0.47***	0.21***	0.08*	0.03	0.08*
Z32	S_2	r_3	0.55***	0.23***	0.08*	0.03	0.08*	0.46***	0.16***	0.05	0.02	0.05	0.46***	0.18***	0.05	0.02	0.07*
Z32	S_2	r_4	0.53***	0.20***	0.06*	0.02	0.06*	0.36***	0.11**	0.02	0.01	0.04	0.42***	0.14**	0.03	0.01	0.04
Z32	S_2	r_5	0.51***	0.17***	0.04	0.01	0.05	0.25***	0.09*	0.01	0.01	0.05	0.37***	0.09*	0.02	0.00	0.03
Z32	S_3	r_1	0.54***	0.30*	0.21$_{*}$	0.20$_{**}$	0.21$_{**}$	0.53***	0.25*	0.13	0.07	0.10	0.52$^{***}_{**}$	0.30$^{*}_{*}$	0.19$_{*}$	0.13$_{*}$	0.18$_{*}$
Z32	S_3	r_2	0.55***	0.36$^{*}_{**}$	0.32$_{***}$	0.31$_{***}$	0.33$_{***}$	0.56***	0.31$^{*}_{**}$	0.23$_{**}$	0.19$_{***}$	0.21$_{**}$	0.53$^{***}_{**}$	0.35$^{*}_{***}$	0.27$_{***}$	0.23$_{***}$	0.27$_{***}$
Z32	S_3	r_3	0.55***	0.38$^{*}_{***}$	0.35$_{***}$	0.34$_{***}$	0.38$_{***}$	0.52$^{***}_{**}$	0.37$^{*}_{***}$	0.32$_{***}$	0.31$_{***}$	0.34$_{***}$	0.52$^{***}_{**}$	0.37$^{*}_{***}$	0.33$_{***}$	0.30$_{***}$	0.33$_{***}$
Z32	S_3	r_4	0.55***	0.37$^{*}_{***}$	0.33$_{***}$	0.32$_{***}$	0.38$_{***}$	0.47$^{***}_{***}$	0.35$^{*}_{***}$	0.31$_{***}$	0.32$_{***}$	0.37$_{***}$	0.50$^{***}_{**}$	0.36$^{*}_{***}$	0.32$_{***}$	0.30$_{***}$	0.33$_{***}$
Z32	S_3	r_5	0.52***	0.33$^{*}_{***}$	0.29$_{***}$	0.29$_{***}$	0.34$_{***}$	0.41$^{***}_{***}$	0.31$^{*}_{***}$	0.28$_{***}$	0.29$_{***}$	0.36$_{***}$	0.46$^{***}_{**}$	0.33$^{*}_{***}$	0.30$_{***}$	0.29$_{***}$	0.32$_{***}$
Z39	S_1		0.59***	0.68***	0.68***	0.63***	0.59***	0.59***	0.68***	0.68***	0.63***	0.59***	0.59***	0.68***	0.68***	0.63***	0.59***
Z39	S_2	r_1	0.60***	0.69***	0.68***	0.62***	0.58***	0.59***	0.68***	0.68***	0.62***	0.59***	0.57***	0.69***	0.68***	0.62***	0.58***
Z39	S_2	r_2	0.62***	0.70***	0.68***	0.62***	0.58***	0.61***	0.70***	0.68***	0.62***	0.58***	0.59***	0.70***	0.68***	0.62***	0.58***
Z39	S_2	r_3	0.63***	0.71***	0.68***	0.62***	0.58***	0.63***	0.70***	0.68***	0.62***	0.58***	0.60***	0.70***	0.68***	0.62***	0.58***
Z39	S_2	r_4	0.64***	0.71***	0.68***	0.62***	0.58***	0.63***	0.70***	0.67***	0.61***	0.57***	0.61***	0.70***	0.68***	0.62***	0.58***
Z39	S_2	r_5	0.64***	0.71***	0.68***	0.62***	0.58***	0.63***	0.70***	0.66***	0.60***	0.56***	0.62***	0.70***	0.68***	0.62***	0.58***
Z39	S_3	r_1	0.60***	0.69***	0.69***	0.62***	0.58***	0.59***	0.68***	0.68***	0.63***	0.60***	0.59***	0.69***	0.68***	0.63***	0.60***
Z39	S_3	r_2	0.65$^{*}_{***}$	0.71***	0.70***	0.64***	0.60***	0.62***	0.70***	0.68***	0.63***	0.59***	0.59***	0.71***	0.69***	0.62***	0.58***
Z39	S_3	r_3	0.68$^{***}_{**}$	0.72***	0.72$^{***}_{**}$	0.67$^{***}_{**}$	0.63$^{***}_{**}$	0.63***	0.70***	0.68***	0.62***	0.59***	0.60***	0.71***	0.69***	0.63***	0.59***
Z39	S_3	r_4	0.69$^{***}_{**}$	0.73$^{***}_{*}$	0.73$^{***}_{**}$	0.69$^{***}_{***}$	0.66$^{***}_{***}$	0.64***	0.71***	0.68***	0.62***	0.59***	0.61***	0.72***	0.70***	0.63***	0.59***
Z39	S_3	r_5	0.70$^{***}_{***}$	0.73$^{***}_{*}$	0.74$^{***}_{***}$	0.70$^{***}_{***}$	0.68$^{***}_{***}$	0.64***	0.71***	0.68***	0.62***	0.58***	0.62***	0.71***	0.70$^{***}_{*}$	0.64***	0.60***
Z58	S_1		0.62***	0.68***	0.64***	0.64***	0.67***	0.62***	0.68***	0.64***	0.64***	0.67***	0.62***	0.68***	0.64***	0.64***	0.67***
Z58	S_2	r_1	0.59***	0.68***	0.65***	0.64***	0.67***	0.64***	0.68***	0.64***	0.64***	0.68***	0.59***	0.69***	0.65***	0.65***	0.68***
Z58	S_2	r_2	0.55***	0.69***	0.65***	0.65***	0.67***	0.64***	0.68***	0.64***	0.64***	0.67***	0.56***	0.69***	0.65***	0.65***	0.68***
Z58	S_2	r_3	0.52***	0.69***	0.65***	0.65***	0.68***	0.64***	0.68***	0.64***	0.64***	0.67***	0.53***	0.69***	0.65***	0.65***	0.68***
Z58	S_2	r_4	0.49***	0.69***	0.65***	0.65***	0.67***	0.63***	0.68***	0.64***	0.64***	0.67***	0.52***	0.69***	0.65***	0.65***	0.68***
Z58	S_2	r_5	0.46***	0.69***	0.65***	0.65***	0.66***	0.62***	0.68***	0.63***	0.63***	0.66***	0.52***	0.69***	0.65***	0.65***	0.68***
Z58	S_3	r_1	0.60***	0.69***	0.65***	0.64***	0.67***	0.64***	0.68***	0.65***	0.64***	0.68***	0.59***	0.69***	0.65***	0.65***	0.69***
Z58	S_3	r_2	0.55***	0.69***	0.65***	0.65***	0.68***	0.65***	0.68***	0.65***	0.64***	0.67***	0.56***	0.69***	0.65***	0.66***	0.69***
Z58	S_3	r_3	0.53***	0.69***	0.65***	0.65***	0.68***	0.65***	0.69***	0.65***	0.64***	0.67***	0.53***	0.69***	0.65***	0.65***	0.69***
Z58	S_3	r_4	0.53$^{***}_{*}$	0.69***	0.65***	0.66***	0.69***	0.66$^{***}_{*}$	0.69***	0.66***	0.65***	0.67***	0.52***	0.69***	0.65***	0.65***	0.68***
Z58	S_3	r_5	0.54$^{***}_{**}$	0.69***	0.66***	0.67***	0.68***	0.66$^{***}_{**}$	0.70$^{***}_{*}$	0.66$^{***}_{*}$	0.65***	0.67***	0.52***	0.69***	0.65***	0.65***	0.68***
Significance Codes			$R^{2\,\overline{\mathbf{H(sig.height)}}}$			$R^{2}{}_{\mathbf{C(sig.coverage)}}$		$^{***}: p < 0.001$			$^{**}: p < 0.01$			$^{*}: p < 0.05$			

Z39 was identified as the crop growth stage with the best prediction performance. Figure 5 points out the most interesting findings. Generally, all VIs performed well, although the best results were achieved using ExG. High and intermediate ground resolutions of 0.04 and 0.06 m·px^{-1} showed R^2 values of up to 0.74 for strategy S_3. However, strategy S_3 improved results for ExG only. VIg and PPRb did not show significant improvements. Strategy S_2 outperformed strategy S_1 for resolutions of 0.02 and 0.04 m·px^{-1}, whereas at intermediate and low ground resolutions, strategies S_1 and S_2 did not differ in prediction accuracy. Coarse VI layer information and the beginning of canopy closure seemed to level out differences of simple plot mean height computation and the classification-based one. Unexpectedly, the highest resolution of 0.02 m·px^{-1} performed worse than high/intermediate resolutions. Although

Remote Sens. **2014**, *11* **10348**

strategies S_2 and S_3 significantly improved prediction using ExG, highest resolution strategies appeared to be prone to higher noise and a scale effect, as the level of resolution leads to analysis in between leaf and canopy level. As a consequence, CSM and classification results may be biased.

Table 6. The resulting root mean squared errors of prediction (RMSEP) of the leave-one-out cross-validation for evaluation of the predictive quality of applying strategies S_{1-3} for all combinations of VIs, aerial image ground resolutions, crop growth stages and computed Ridler thresholds.

Ground Res. (m·px^{-1})					**ExG**					**VIg**					**PPRb**			
Z	**S_x**	**r_x**	**0.02**	**0.04**	**0.06**	**0.08**	**0.10**	**0.02**	**0.04**	**0.06**	**0.08**	**0.10**	**0.02**	**0.04**	**0.06**	**0.08**	**0.10**
Z32	S_1		0.93	1.11	1.20	1.25	1.21	0.93	1.11	1.20	1.25	1.21	0.93	1.11	1.20	1.25	1.21
Z32	S_2	r_1	0.88	1.11	1.21	1.25	1.21	0.89	1.13	1.21	1.25	1.22	0.94	1.12	1.21	1.25	1.21
Z32	S_2	r_2	0.86	1.13	1.21	1.25	1.22	0.87	1.15	1.22	1.26	1.23	0.93	1.14	1.22	1.25	1.22
Z32	S_2	r_3	0.87	1.14	1.23	1.26	1.22	0.95	1.17	1.24	1.26	1.24	0.94	1.16	1.24	1.26	1.23
Z32	S_2	r_4	0.88	1.15	1.24	1.26	1.23	1.03	1.20	1.26	1.27	1.24	0.98	1.19	1.26	1.27	1.24
Z32	S_2	r_5	0.90	1.17	1.25	1.27	1.24	1.11	1.22	1.27	1.27	1.24	1.02	1.21	1.27	1.28	1.26
Z32	S_3	r_1	0.90	1.10	1.16	1.17	1.15	0.90	1.14	1.23	1.26	1.23	0.91	1.10	1.19	1.23	1.19
Z32	S_3	r_2	0.88	1.04	1.07	1.08	1.06	0.87	1.08	1.14	1.16	1.15	0.91	1.07	1.13	1.16	1.13
Z32	S_3	r_3	0.88	1.02	1.05	1.05	1.02	0.90	1.03	1.07	1.08	1.05	0.91	1.04	1.08	1.10	1.07
Z32	S_3	r_4	0.88	1.03	1.06	1.07	1.03	0.95	1.05	1.08	1.07	1.03	0.93	1.04	1.08	1.09	1.07
Z32	S_3	r_5	0.90	1.07	1.10	1.09	1.06	1.00	1.08	1.10	1.09	1.04	0.96	1.07	1.09	1.10	1.07
Z39	S_1		0.83	0.73	0.74	0.79	0.83	0.83	0.73	0.74	0.79	0.83	0.83	0.73	0.74	0.79	0.83
Z39	S_2	r_1	0.83	0.71	0.73	0.80	0.83	0.83	0.73	0.74	0.80	0.83	0.85	0.72	0.74	0.80	0.83
Z39	S_2	r_2	0.80	0.70	0.73	0.80	0.83	0.81	0.70	0.74	0.80	0.83	0.83	0.71	0.74	0.80	0.83
Z39	S_2	r_3	0.79	0.70	0.73	0.80	0.83	0.79	0.70	0.74	0.80	0.84	0.81	0.70	0.74	0.80	0.83
Z39	S_2	r_4	0.78	0.69	0.73	0.80	0.84	0.78	0.70	0.75	0.81	0.85	0.81	0.70	0.74	0.80	0.83
Z39	S_2	r_5	0.77	0.69	0.74	0.80	0.84	0.78	0.70	0.76	0.82	0.86	0.80	0.70	0.74	0.80	0.83
Z39	S_3	r_1	0.84	0.72	0.74	0.81	0.85	0.84	0.73	0.74	0.80	0.83	0.84	0.73	0.75	0.80	0.83
Z39	S_3	r_2	0.78	0.71	0.73	0.79	0.83	0.81	0.71	0.75	0.81	0.84	0.84	0.70	0.74	0.81	0.85
Z39	S_3	r_3	0.75	0.69	0.70	0.76	0.79	0.80	0.71	0.76	0.81	0.84	0.83	0.69	0.73	0.80	0.84
Z39	S_3	r_4	0.73	0.68	0.68	0.73	0.76	0.79	0.70	0.75	0.81	0.84	0.81	0.69	0.73	0.80	0.83
Z39	S_3	r_5	0.71	0.67	0.68	0.72	0.74	0.78	0.70	0.75	0.81	0.85	0.81	0.70	0.73	0.79	0.83
Z58	S_1		0.82	0.72	0.77	0.77	0.74	0.82	0.72	0.77	0.77	0.74	0.82	0.72	0.77	0.77	0.74
Z58	S_2	r_1	0.85	0.72	0.76	0.76	0.73	0.79	0.72	0.77	0.77	0.73	0.85	0.71	0.76	0.76	0.73
Z58	S_2	r_2	0.89	0.71	0.76	0.76	0.73	0.79	0.72	0.77	0.77	0.73	0.89	0.71	0.76	0.76	0.73
Z58	S_2	r_3	0.93	0.71	0.76	0.76	0.73	0.80	0.72	0.77	0.77	0.74	0.91	0.71	0.76	0.76	0.73
Z58	S_2	r_4	0.96	0.71	0.76	0.76	0.73	0.80	0.72	0.78	0.77	0.74	0.93	0.71	0.76	0.76	0.73
Z58	S_2	r_5	0.98	0.71	0.76	0.76	0.74	0.82	0.72	0.78	0.77	0.75	0.93	0.72	0.76	0.76	0.73
Z58	S_3	r_1	0.85	0.72	0.77	0.77	0.74	0.80	0.73	0.78	0.78	0.74	0.86	0.72	0.77	0.76	0.72
Z58	S_3	r_2	0.90	0.72	0.77	0.77	0.74	0.80	0.73	0.78	0.78	0.74	0.90	0.72	0.77	0.76	0.72
Z58	S_3	r_3	0.94	0.72	0.77	0.76	0.73	0.79	0.72	0.77	0.78	0.74	0.92	0.72	0.77	0.76	0.73
Z58	S_3	r_4	0.93	0.72	0.77	0.75	0.73	0.78	0.71	0.76	0.77	0.74	0.93	0.72	0.77	0.76	0.73
Z58	S_3	r_5	0.92	0.72	0.76	0.75	0.73	0.78	0.71	0.76	0.76	0.74	0.93	0.72	0.77	0.77	0.73

At Z58, results were strongly influenced by the occurrence of canopy closure. Hence, neither strategy S_2 nor strategy S_3 were able to significantly improve the corn grain yield prediction performance of strategy S_1. Moreover, highest resolution strategies showed similar patterns as in Z39. Except using VIg, imagery at a ground resolution of 0.02 m·px^{-1} seemed to underlay CSM and misclassification as in Z39. All other resolutions performed comparatively well, independent of applied strategy and VI. Although, these resolutions did not reach the maximum R^2 values of Z39, they were still considered as suitable for prediction.

Figure 6. Spatial illustration of plot-wise distribution of harvested corn grain yield (**top**), corn grain yield predicted by strategy S_3 at crop growth stage Z39, with ExG at Ridler threshold r_4 and an aerial image ground resolution of 0.04 m·px^{-1} (**middle**) and the resulting prediction error of this strategy (**bottom**). For this strategy, the total root mean squared error of prediction (RMSEP) equals 0.68 t·ha^{-1} (8.8%).

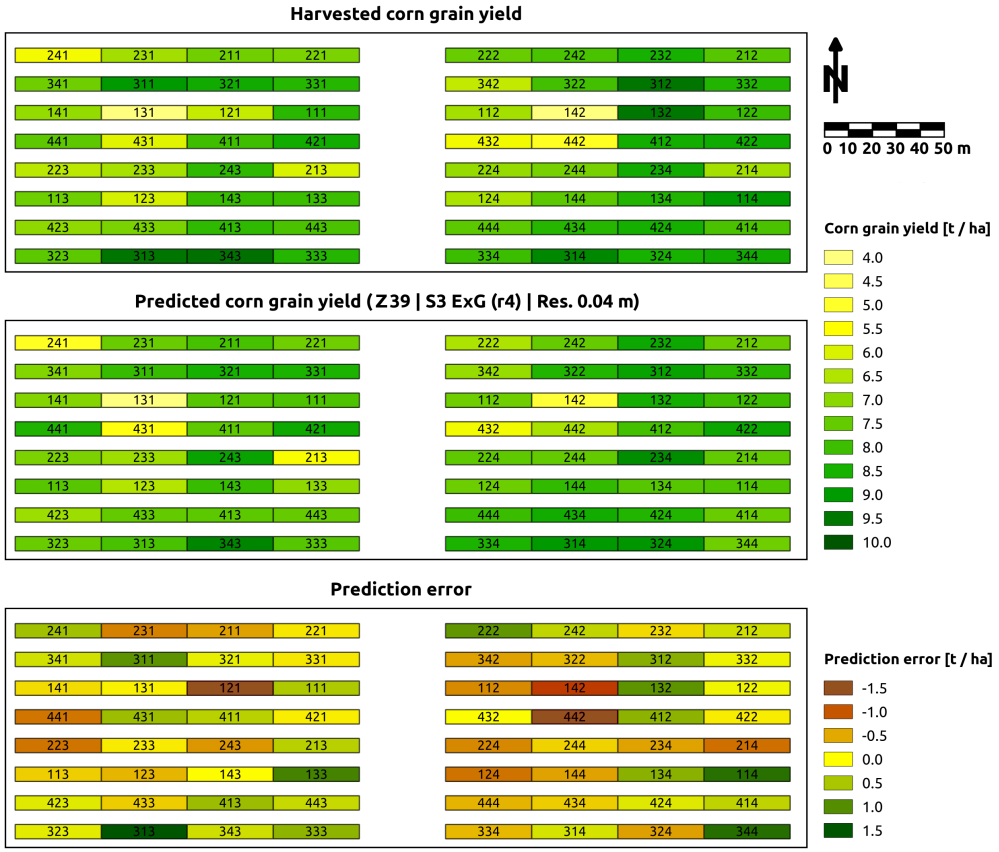

Table 7 summarizes the key findings. The most suitable resolution and modeling strategy depends on the crop growth stage. Due to row-based cultivation of corn and missing canopy closure, early growth stages require very high resolution imagery for accurate CSM computation and classification-based separation of crop and soil. Therefore, strategies S_2 and S_3 result in higher R^2 values than strategy S_1 ($R^2 \leq 0.56$). With ongoing crop development and beginning canopy closure, high resolution imagery and crop/soil classification gets less and less important. Highest resolution imagery showed a significant reduction of prediction accuracy at mid-season growth stages. All other imagery resolutions performed almost equally well (approximately $0.60 \leq R^2 \leq 0.70$) at all strategies S_{1-3} within these stages. Best prediction results were achieved by applying strategy S_2 and especially strategy S_3 at Z39 ($R^2 \leq 0.74$). Although strategy S_3 proved to have good performance at this specific growth stage, further investigation of the influence of crop coverage factor C_{irstv} on the prediction results of this multiple linear regression strategy seems of great interest.

Table 7. Overview of the best performing parameters for early- to mid-season corn grain yield prediction at different crop growth stages. So far, the increase in prediction performance in strategy S_3 appears to underlay an unknown factor. Therefore, strategy S_3 is listed in brackets.

	Growth Stage		
	Z32	**Z39**	**Z58**
Ground Resolution	highest/high	high/intermediate	high/intermediate/low
Vegetation Index	ExG	ExG	VIg
Prediction Strategy	S_2 / (S_3)	S_2 / (S_3)	S_1 / S_2 / (S_3)

These findings indicate the best corn grain yield prediction at mid-season crop growth stages Z39 and Z58. They are in accordance with the findings of Yin *et al.* [37]. Nevertheless, none of the strategies showed results comparable to the best predictions of Yin *et al.* [37]. Depending on the growth stage and crop rotation system, Yin *et al.* [37] stated significant determination coefficients of $0.25 \leq R^2 \leq 0.89$, whereas low R^2 values were achieved at early-season growth stages, only.

Applying strategy S_3 at Z39, Figure 6 visualizes plot-wise prediction results and compares them to the harvested corn grain yield. Using ExG at Ridler threshold r_4 and an aerial image ground resolution of 0.04 m·px^{-1}, the total RMSEP equals 0.68 t·ha^{-1} (8.8%). Although this strategy performed best, the ANOVA of the field trial's input factors did not show significant influence of sowing density on corn grain yield. As strategy S_3 utilizes computed crop coverage C_{irstv} as the estimator for sowing/stand density, the increase in prediction performance seems to underlay another factor, correlated with C_{irstv}. Other combinations of strategy S_3 and VIg/PPRb did not show improved results compared to strategy S_2.

4. Conclusions

This work shows the potential of exploiting spectral and spatial information from UAS-based RGB imagery for predicting corn grain yield in early- to mid-season crop growth stages. RGB imagery was used to compute crop surface models and to extract crop height information. In combination with RGB-based VI information, three different linear regression models were tested for the prediction of corn grain yield with R^2 determination coefficients of up to 0.74 and RMSEP ranging from 0.67 to 1.28 t·ha^{-1} (8.8% to 16.9%).

Generally, all tested VIs performed almost equally well at any crop growth stage. The same applies to tested classification thresholds r_{2-4}. Although some of the more extreme thresholds r_1 and r_5 showed satisfying results, these thresholds cannot be recommended, because of potential over- or under-estimation of crop coverage.

The most suitable resolution and modeling strategy depends on the crop growth stage. Due to row-based cultivation of corn and missing canopy closure, early growth stages require very high resolution imagery for accurate CSM computation and classification-based separation of crop and soil. Compared to using simple unclassified mean crop heights (S_1), prediction results significantly improve, when accounting for additional crop/soil classification information (S_2 and S_3). With ongoing crop

development and beginning canopy closure, high resolution imagery gets less and less important, sometimes even disadvantageous, due to higher noise. Good prediction results are achieved at intermediate resolutions by considering crop coverage as the second predictor variable (S_3). With the completion of canopy closure, neither high resolution imagery nor crop/soil classification show potential to further improve prediction. Concluding these findings, combined spectral and spatial modeling, based on aerial images and CSMs, proves to be a suitable method for mid-season corn yield prediction.

Acknowledgments

The authors acknowledge the Carl-Zeiss Foundation (Carl-Zeiss-Stiftung) for funding this work as part of the collaborative project "SenGIS" at the University of Hohenheim, Stuttgart, Germany.

Author Contributions

Jakob Geipel performed the field work, acquired the data, processed the imagery into VI layers and CSMs, computed the Ridler thresholds and mean crop heights, set up the corn yield predicition models, and wrote the manuscript. Johanna Link proposed the field trial's design, supported the statistical analysis, and wrote the introduction. Wilhelm Claupein proposed the idea for this study and helped with editorial contributions.

Conflicts of Interest

The authors declare no conflicts of interest.

References

1. Stafford, J. Implementing precision agriculture in the 21st century. *J. Agr. Eng. Res.* **2000**, *76*, 267–275.
2. Delin, S. Site-Specific Nitrogen Fertilization Demand in Relation to Plant Available Soil Nitrogen and Water. PhD Thesis, Swedish University of Agricultural Sciences, Skara, Sweden, 2005.
3. Flowers, M.; Weisz, R.; White, J. Yield-based management zones and grid sampling strategies: Describing soil test and nutrient variability. *Agron. J.* **2005**, *97*, 968–982.
4. Link, J.; Graeff, S.; Batchelor, W.D.; Claupein, W. Evaluating the economic and environmental impact of environmental compensation payment policy under uniform and variable-rate nitrogen management. *Agric. Syst.* **2006**, *91*, 135–153.
5. Bongiovanni, R.G.; Robledo, C.W.; Lambert, D.M. Economics of site-specific nitrogen management for protein content in wheat. *Comput. Electron. Agric.* **2007**, *58*, 13–24.
6. Mourtzinis, S.; Arriaga, F.J.; Balkcom, K.S.; Ortiz, B.V. Corn grain and stover yield prediction at R1 growth stage. *Agron. J.* **2013**, *105*, 1045–1050.
7. Lauer, J. Methods for Calculating Corn Yield. Avaliable online: http://corn.agronomy.wisc.edu/AA/pdfs/A033.pdf (accessed on 3 July 2014).
8. Blackmore, S. The interpretation of trends from multiple yield maps. *Comput. Electron. Agric.* **2000**, *26*, 37–51.

9. Rodrigues, M.S.; Cora, J.E.; Castrignano, A.; Mueller, T.G.; Rienzi, E. A spatial and temporal prediction model of corn grain yield as a function of soil attributes. *Agron. J.* **2013**, *105*, 1878–1887.
10. Thorp, K.R.; DeJonge, K.C.; Kaleita, A.L.; Batchelor, W.D.; Paz, J.O. Methodology for the use of DSSAT models for precision agriculture decision support. *Comput. Electron. Agric.* **2008**, *64*, 276–285.
11. Batchelor, W.D.; Basso, B.; Paz, J.O. Examples of strategies to analyze spatial and temporal yield variability using crop models. *Eur. J. Agron.* **2002**, *18*, 141–158.
12. Aparicio, N.; Villegas, D.; Casadesus, J.; Araus, J.L.; Royo, C. Spectral vegetation indices as nondestructive tools for determining durum wheat yield. *Agron. J.* **2000**, *92*, 83–91.
13. Pinter, P.J.; Jackson, R.D.; Idso, S.B.; Reginato, R.J. Multidate spectral reflectance as predictors of yield in water stressed wheat and barley. *Int. J. Remote Sens.* **1981**, *2*, 43–48.
14. Salazar, L.; Kogan, F.; Roytman, L. Using vegetation health indices and partial least squares method for estimation of corn yield. *Int. J. Remote Sens.* **2008**, *29*, 175–189.
15. Wang, J.; Li, X.; Lu, L.; Fang, F. Estimating near future regional corn yields by integrating multi-source observations into a crop growth model. *Eur. J. Agron.* **2013**, *49*, 126–140.
16. Fang, H.; Liang, S.; Hoogenboom, G.; Teasdale, J.; Cavigelli, M. Corn-yield estimation through assimilation of remotely sensed data into the CSM-CERES-Maize model. *Int. J. Remote Sens.* **2008**, *29*, 3011–3032.
17. Van der Wal, T.; Abma, B.; Viguria, A.; Previnaire, E.; Zarco-Tejada, P.; Serruys, P.; van Valkengoed, E.; van der Voet, P. Fieldcopter: Unmanned aerial systems for crop monitoring services. In *Precision Agriculture '13*; Stafford, J., Ed.; Wageningen Academic Publishers: Wageningen, The Netherlands, 2013; pp. 169–175.
18. Berni, J.; Zarco-Tejada, P.; Suarez, L.; Fereres, E. Thermal and narrowband multispectral remote sensing for vegetation monitoring from an unmanned aerial vehicle. *IEEE Trans. Geosci. Remote Sens.* **2009**, *47*, 722–738.
19. Hunt, E., Jr.; Dean Hively, W.; Fujikawa, S.; Linden, D.; Daughtry, C.; McCarty, G. Acquisition of NIR-green-blue digital photographs from unmanned aircraft for crop monitoring. *Remote Sens.* **2010**, *2*, 290–305.
20. Thenkabail, P.S.; Lyon, J.G.; Huete, A. Advances in hyperspectral remote sensing of vegetation and agricultural croplands. In *Hyperspectral Remote Sensing of Vegetation*, 1st ed.; Thenkabail, P.S., Lyon, J.G., Huete, A., Eds.; CRC Press Inc.: Boca Raton, FL, USA, 2012; pp. 4–35.
21. Pena, J.M.; Torres-Sanchez, J.; de Castro, A.I.; Kelly, M.; Lopez-Granados, F. Weed mapping in early-season maize fields using object-based analysis of unmanned aerial vehicle (UAV) images. *PLoS One* **2013**, doi:10.1371/journal.pone.0077151.
22. Torres-Sanchez, J.; Lopez-Granados, F.; Castro, A.I.D.; Pena-Barragan, J.M. Configuration and specifications of an unmanned aerial vehicle (UAV) for early site specific weed management. *PLoS One* **2013**, doi:10.1371/journal.pone.0058210.
23. Eisenbeiss, H.; Sauerbier, M. Investigation of uav systems and flight modes for photogrammetric applications. *Photogramm. Rec.* **2011**, *26*, 400–421.

24. Neitzel, F.; Klonowski, J. Mobile 3D mapping with a low-cost UAV system. *Int. Arch. Photogramm. Remote Sens. Spat. Inf. Sci.* **2011**, *38*, 1–6.
25. Harwin, S.; Lucieer, A. Assessing the accuracy of georeferenced point clouds produced via multi-view stereopsis from Unmanned Aerial Vehicle (UAV) imagery. *Remote Sens.* **2012**, *4*, 1573–1599.
26. Lucieer, A.; Jong, S.M.D.; Turner, D. Mapping landslide displacements using Structure from Motion (SfM) and image correlation of multi-temporal UAV photography. *Prog. Phys. Geogr.* **2014**, *38*, 97–116.
27. Eisenbeiss, H. The autonomous mini helicopter: A powerful platform for mobile mapping. *Int. Arch. Photogramm. Remote Sens. Spat. Inf. Sci.* **2008**, *37*, 977–983.
28. Bendig, J.; Bolten, A.; Bareth, G. UAV-based imaging for multi-temporal, very high resolution crop surface models to monitor crop growth variability. *Photogramm. Fernerkund. Geoinf.* **2013**, *2013*, 551–562.
29. Bendig, J.; Willkomm, M.; Tilly, N.; Gnyp, M.L.; Bennertz, S.; Qiang, C.; Miao, Y.; Lenz-Wiedemann, V.I.S.; Bareth, G. Very high resolution crop surface models (CSMs) from UAV-based stereo images for rice growth monitoring in Northeast China. *Int. Arch. Photogramm. Remote Sens. Spat. Inf. Sci.* **2013**, *40*, 45–50.
30. Waser, L.; Baltsavias, E.; Ecker, K.; Eisenbeiss, H.; Feldmeyer-Christe, E.; Ginzler, C.; Küchler, M.; Zhang, L. Assessing changes of forest area and shrub encroachment in a mire ecosystem using digital surface models and CIR aerial images. *Remote Sens. Environ.* **2008**, *112*, 1956–1968.
31. Diaz-Varela, R.; Zarco-Tejada, P.; Angileri, V.; Loudjani, P. Automatic identification of agricultural terraces through object-oriented analysis of very high resolution DSMs and multispectral imagery obtained from an unmanned aerial vehicle. *J. Environ. Manag.* **2014**, *134*, 117–126.
32. Zarco-Tejada, P.; Diaz-Varela, R.; Angileri, V.; Loudjani, P. Tree height quantification using very high resolution imagery acquired from an unmanned aerial vehicle (UAV) and automatic 3D photo-reconstruction methods. *Eur. J. Agron.* **2014**, *55*, 89–99.
33. Woebbecke, D.; Meyer, G.; von Bargen, K.; Mortensen, D. Color indices for weed identification under various soil, residue and lighting conditions. *Ame. Soc. Agric. Eng.* **1995**, *38*, 259–269.
34. Gitelson, A.; Kaufman, Y.; Stark, R.; Rundquist, D. Novel algorithms for remote estimation of vegetation fraction. *Remote Sens. Environ.* **2002**, *80*, 76–87.
35. Torres-Sanchez, J.; Pena, J.; de Castro, A.; Lopez-Granados, F. Multi-temporal mapping of the vegetation fraction in early-season wheat fields using images from UAV. *Comput. Electron. Agric.* **2014**, *103*, 104–113.
36. Katsvairo, T.W.; Cox, W.J.; van Es, H.M. Spatial growth and nitrogen uptake variability of corn at two nitrogen levels. *Agron. J.* **2003**, *95*, 1000–1011.
37. Yin, X.; Jaja, N.; McClure, M.A.; Hayes, R.M. Comparison of models in assessing relationship of corn yield with plant height measured during early- to mid-season. *J. Agric. Sci.* **2011**, *3*, 14–24.

38. Yin, X.; McClure, M.A.; Jaja, N.; Tyler, D.D.; Hayes, R.M. In-season prediction of corn yield using plant height under major production systems. *Agron. J.* **2011**, *103*, 923–929.
39. HiSystems GmbH. Available online: http://mikrokopter.de/ucwiki/en/HexaKopter (accessed on 7 March 2014).
40. Raspberry Pi Foundation. Available online: http://www.raspberrypi.org/faqs (accessed on 7 March 2014).
41. Geipel, J.; Peteinatos, G.G.; Claupein, W.; Gerhards, R. Enhancement of micro Unmanned Aerial Vehicles to agricultural aerial sensor systems. In *Precision Agriculture '13*; Stafford, J., Ed.; Wageningen Academic Publishers: Wageningen, The Netherlands, 2013; pp. 161–167.
42. Canon Europe Ltd. Available online: http://www.canon-europe.com/For_Home/Product_Finder/Cameras/Digital_Camera/IXUS/Digital_IXUS_110_IS/ (accessed on 7 March 2014).
43. Zadoks, J.C.; Chang, T.T.; Konzak, C.F. A decimal code for the growth stages of cereals. *Weed Res.* **1974**, *14*, 415–421.
44. AgiSoft LLC. Available online: http://agisoft.ru/products/photoscan/professional/ (accessed on 12 March 2014).
45. Lowe, D.G. Method and Apparatus for Identifying Scale Invariant Features in an Image and Use of Same for Locating an Object in an Image. Patent US6711293 B1, 23 March 2004.
46. Snavely, N.; Seith, S.M.; Szeliski, R. Modeling the world from internet photo collections. *Int. J. Comput. Vis.* **2008**, *80*, 189–210.
47. Sibson, R. A brief description of natural neighbor interpolation. In *Interpreting Multivariate Data*; Barnett, V., Ed.; John Wiley: Chichester, UK, 1981; pp. 21–36.
48. R Development Core Team. *R: A Language and Environment for Statistical Computing*; R Foundation for Statistical Computing: Vienna, Austria, 2013.
49. Hijmans, R.J.; van Etten, J. *Raster: Geographic Analysis and Modeling with Raster Data*; R Package Version 2.3–0, 2014. Available online: http://cran.r-project.org/web/packages/raster/ (accessed on 15 April 2014).
50. Kort, E. *Rtiff: A Tiff Reader for R.*; R Package Version 1.4.4., 2014. Available online: http://cran.r-project.org/web/packages/rtiff/ (accessed on 15 April 2014).
51. Meyer, G.E.; Mehta, T.; Kocher, M.; Mortensen, D.; Samal, A. Textural imaging and discriminant analysis for distinguishing weeds for spot spraying. *Trans. ASAE* **1998**, *41*, 1189–1197.
52. Metternicht, G. Vegetation indices derived from high-resolution airborne videography for precision crop management. *Int. J. Remote Sens.* **2003**, *24*, 2855–2877.
53. Ridler, T.; Calvard, S. Picture thresholding using an iterative selection method. *IEEE Trans. Syst. Man Cybern.* **1978**, *8*, 630–632.
54. QGIS Development Team. *QGIS Geographic Information System*; Available online: http://qgis.osgeo.org (accessed on 15 April 2014).
55. Turner, D.; Lucieer, A.; Watson, C. An automated technique for generating georectified mosaics from ultra-high resolution Unmanned Aerial Vehicle (UAV) imagery, based on Structure from Motion (SfM) point clouds. *Remote Sens.* **2012**, *4*, 1392–1410.

56. Ruiz, J.J.; Diaz-Mas, L.; Perez, F.; Viguria, A. Evaluating the accuracy of DEM generation algorithms from UAV imagery. *Int. Arch. Photogramm. Remote Sens. Spatial Inf. Sci.* **2013**, *40*, 333–337.

4 A Programmable Aerial Multispectral Camera System for In-Season Crop Biomass and Nitrogen Content Estimation

Geipel, J., J. Link, J. A. Wirwahn and W. Claupein, 2016. A Programmable Aerial Multispectral Camera System for In-Season Crop Biomass and Nitrogen Content Estimation. *Agriculture*, 6(1):4.

The presented application in Section 3 was mainly based on spatial and temporal considerations. These components reflect only parts of the possibilities UAS can offer to PF. An even more promising ability is a spectral one: the analysis of plant canopy reflection. UAS are often used to carry imaging and non-imaging devices to detect upwelling radiation from the fields and analyze the canopy's reflection with the methods of satellite remote-sensing. However, compared to satellites, UAS have the advantage of a much higher spectral, spatial and temporal resolution.

This publication describes the development of a prototype multispectral camera system for the UAS. The camera system was designed as lightweight payload and was equipped with bandpass filters to measure four narrow wavelength bands in the so-called red-edge region. This is a transition zone in between the visual and the near-infrared radiation spectrum, which is sensitive to leaf chlorophyll content and is, therefore, used to estimate above-ground biomass and nitrogen content. The camera system is programmable and expendable for future real-time applications and was tested in a split-fertilized nitrogen field trial in winter wheat. Measurements were conducted to process NDVI and REIP orthoimages at different growth stages in between the end of stem elongation and the end of anthesis. The camera system performed well and the multispectral images could be processed to the desired orthoimages. The images were analyzed with simple linear regression models and showed good correlations in between above-ground biomass and the NDVI as well as for nitrogen content and the REIP. Moreover, the REIP showed excellent results for grain yield and good results for grain protein content prediction. The results indicate that the camera system offers the possibility of acquiring accurate actual canopy information at a large scale.

agriculture

MDPI

Article

A Programmable Aerial Multispectral Camera System for In-Season Crop Biomass and Nitrogen Content Estimation

Jakob Geipel [1,*], Johanna Link [1], Jan A. Wirwahn [2] and Wilhelm Claupein [1]

Received: 29 October 2015 ; Accepted: 29 December 2015 ; Published: 18 January 2016
Academic Editor: Yanbo Huang

[1] Institute of Crop Science, University of Hohenheim, Fruwirthstr. 23, Stuttgart 70599, Germany; Johanna.Link@uni-hohenheim.de (J.L.); Wilhelm.Claupein@uni-hohenheim.de (W.C.)
[2] Institute for Geoinformatics, University of Münster, Heisenbergstr. 2, Münster 48149, Germany; jan.wirwahn@uni-muenster.de
* Correspondence: jakob.geipel@uni-hohenheim.de; Tel.: +49-711-459-22938

Abstract: The study introduces a prototype multispectral camera system for aerial estimation of above-ground biomass and nitrogen (N) content in winter wheat (*Triticum aestivum* L.). The system is fully programmable and designed as a lightweight payload for unmanned aircraft systems (UAS). It is based on an industrial multi-sensor camera and a customizable image processing routine. The system was tested in a split fertilized N field trial at different growth stages in between the end of stem elongation and the end of anthesis. The acquired multispectral images were processed to normalized difference vegetation index (NDVI) and red-edge inflection point (REIP) orthoimages for an analysis with simple linear regression models. The best results for the estimation of above-ground biomass were achieved with the NDVI (R^2 = 0.72–0.85, RMSE = 12.3%–17.6%), whereas N content was estimated best with the REIP (R^2 = 0.58–0.89, RMSE = 7.6%–11.7%). Moreover, NDVI and REIP predicted grain yield at a high level of accuracy (R^2 = 0.89–0.94, RMSE = 9.0%–12.1%). Grain protein content could be predicted best with the REIP (R^2 = 0.76–0.86, RMSE = 3.6%–4.7%), with the limitation of prediction inaccuracies for N-deficient canopies.

Keywords: camera; multispectral; nitrogen; precision agriculture; protein; remote sensing; UAS; UAV; winter wheat (*Triticum aestivum* L.); yield

1. Introduction

Extensive use of nitrogen (N) leads to negative environmental impacts, like eutrophication, acid rains, drinking water contamination and nitrous oxide emissions [1–5]. Nevertheless, N plays a major role in crop growth and crop quality in wheat (*Triticum* L.) production [6]. Farmers have to achieve a certain quantity and quality of yield. Thus, they require N fertilization strategies that may ensure good outcomes for both yields and the environment. The calculation of appropriate amounts of N and the correct timing of the fertilization are crucial to supply the crop with sufficient nutrients at all stages of crop development. Moreover, it decreases the risk of N loss through leaching [7] and nitrous oxide emissions [8].

In wheat cultivation, split N application is a common way to influence grain yield and grain protein content. Several studies have shown that N applications before flowering increase mainly grain mass [9], whereas N applications around flowering increase mainly grain protein content [10,11]. In the past, farmers often used simplified methods to estimate the N demand for late N applications. Nowadays, rules of thumb like 1 kg N per 1000 kg of expected grain yield are more

Agriculture **2016**, *6*, 4

and more replaced by methods that take soil available N, previous N applications, above-ground biomass and its current N content into account [12,13]. A common N recommendation method is to measure the N content in plant leaves during the vegetative period and to compare it to a critical amount of N, required for a maximum of biomass production [14–16]. The critical N content in winter wheat (*Triticum aestivum* L.) was defined by Justes *et al.* [17,18] in a universal equation based on the actual above-ground biomass. Thus, recommended rates can be calculated from actual estimates of biomass and N content alone.

As sampling of a representative amount of probes in a heterogeneous field is a costly and time-consuming task, farmers increasingly utilize online systems to collect site-specific information, to calculate appropriate amounts of fertilizer and to apply the dressing at the same time [19]. Most of these systems are based on optical sensors, which measure the plant canopy reflection to calculate targeted N prescription with a proprietary algorithm, e.g., the Yara N-Sensor (Yara International ASA, Oslo, Norway), the ISARIA crop sensor (Fritzmeier GmbH & Co. KG, Großhelfendorf, Germany) and the GreenSeeker (Trimble Navigation Ltd., Sunnyvale, CA, USA).

Within the last few years, remote sensing with unmanned aerial vehicles (UAVs) or unmanned aircraft systems (UASs) became popular in the precision agriculture domain. These systems are able to provide data at high spatial and temporal resolutions for crop and soil monitoring [20]. Commonly, researchers utilize image-based systems in the visual and near-infrared radiation spectrum [21], giving a more comprehensive impression of the field than spot measurements with ground-based detection systems. Aasen *et al.* [22] gave a detailed overview and definition of the different types of imaging systems, which are currently in use on-board UAVs. Generally, imaging systems can be classified as multispectral systems with few bands [23–26] and as more sophisticated hyperspectral systems with a multitude of bands [22,27,28]. The hyperspectral systems combine the benefits of high spectral and spatial resolution, but are still rare and expensive.

Above-ground biomass and N content of wheat are known to be detectable with a limited number of bands [16,29,30]. Therefore, this study focuses on the development of a multispectral camera system capable of estimating parameters for the calculation of optimal N applications. The system is intended to operate on-board a UAS, to be lightweight and fully programmable for future applications. To ensure operability in this context, the system was tested in a split fertilized N field trial in winter wheat before and after the late N application.

2. Materials and Methods

The camera system was designed as a lightweight payload for a UAS (see Figure 1a). It is based on an industrial multi-sensor camera (D3, VRMagic GmbH, Mannheim, Germany), with four identical monochrome imaging sensors, four identical lens systems and four different bandpass filters (bk Interferenzoptik Elektronik GmbH, Nabburg, Germany) (see Figure 1b). It offers several hardware interfaces and was coupled to a luminosity sensor to measure ambient solar radiation for exposure time calculation. Moreover, it was connected to the UAS's processing unit via Ethernet connection. The specifications of all camera system components are given in Table 1.

The camera system is able to measure four narrow wavelength bands in the so-called red-edge region, a transition zone in between the visual and the near-infrared radiation spectrum, which is sensitive to leaf chlorophyll content [31–33]. For this study, the wavelength bands at 670, 700, 740 and 780 nm were selected. They can be used to approximate the normalized difference vegetation index (NDVI) [34] and the red-edge inflection point (REIP) [33]. The formulas are given in Equations (1) and (2), with R_{nm} being the reflectance at the four narrow bands.

$$NDVI = \frac{(R_{780} - R_{670})}{(R_{780} + R_{670})} \tag{1}$$

$$REIP = 700 + 40 \times \frac{(\frac{(R_{670}+R_{780})}{2} - R_{700})}{(R_{740} - R_{700})} \tag{2}$$

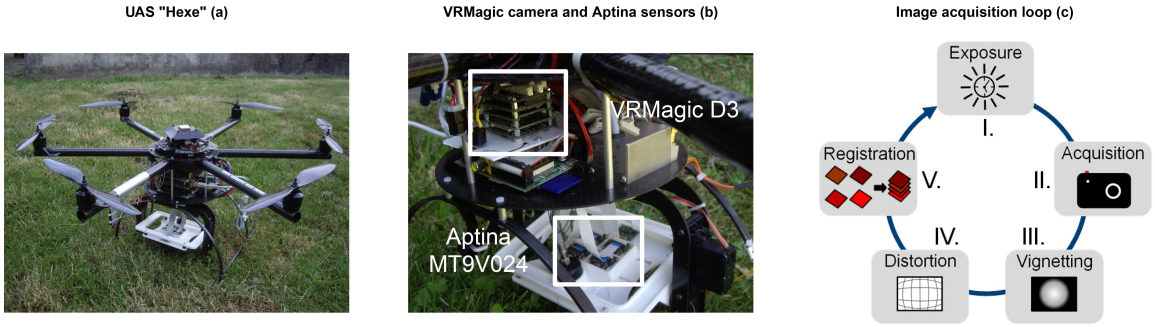

Figure 1. Carrier platform "Hexe" (**a**) with the mounted VRMagic D3 camera system and four attached Aptina imaging sensors (**b**). The five main steps of the image acquisition and processing loop (**c**): (i) exposure time measurement; (ii) simultaneous image acquisition; (iii) vignetting correction; (iv) lens distortion correction; and (v) image-to-image registration.

Table 1. Overview of the camera system specifications. The system consists of an industrial D3 camera platform, four identical imaging sensors and lens systems, four specific bandpass filters and a luminosity sensor to measure ambient solar radiation.

Component	Parameter	Value	Parameter	Value
D3 platform	Name	VRmD3MFC		
	CPU	1-GHz ARM Cortex-A8 Core	Memory	32 GB flash
	DSP	700-MHz C674x	RAM	2 GB DDR3-800
Image sensor	Name	Aptina MT9V024		
	Size	4.51 mm (H) × 2.88 mm (V)	Pixel size	6 µm × 6 µm
	Resolution	752 px (H) × 480 px (V)	Shutter	Global
	Dynamic range	10 bit (1024)	Quantum eff.	~49%, 47.5%, 44%, 41%
	Type	CMOS monochrome (1/3 in)		(670, 700, 740, 780 nm)
Lens system	Focal length	3.6 mm	F-number	1.8
Filter	Type	Bandpass interference filter		
	Wavelengths	670, 700, 740, 780 nm	Tmax	≥70, typically 85%
	Center	±2 nm	FWHM	10 ±2 nm
Luminosity	Name	TSL 2561		
	Sensitivity	~350–900 nm	Dynamic range	0.1–40,000 lx

Both NDVI and REIP are well-known measures for winter wheat properties, such as above-ground biomass, N content and grain yield. The REIP is commonly used to estimate crop N content, whereas the NDVI is often used for biomass estimation and grain yield prediction [16,30].

2.1. Image Acquisition Loop

The camera system is fully programmable and was operated with an image acquisition and processing routine of five main steps (see Figure 1c): (i) the ambient solar radiation is detected by the luminosity sensor and processed to an optimal exposure time; (ii) four individual images are acquired simultaneously and saved to the flash memory; (iii) a vignetting correction is applied to each image for the compensation of brightness reduction at the image borders; (iv) the lens distortion error is corrected by re-sampling each image to a rectilinear projection; and (v) the four images are spatially co-registered by a perspective transformation. Steps (i) and (ii) are always performed on-board the camera, whereas Steps (iii)–(v) can be performed on-board or in post-processing.

Agriculture **2016**, *6*, 4

2.1.1. Exposure Time

The exposure time is an important parameter for an imaging system. It controls the shutter and, as a consequence, the amount of time the imaging sensor is exposed to electro-magnetic radiation. Finding an optimal exposure time prevents the sensor from under- and over-exposure and allows one to make use of the sensor's full dynamic range. As ambient solar radiation typically changes during a flight mission, the exposure time needs to be adjusted according to these changes. Therefore, the camera system was set up with a TSL 2561 luminosity sensor (Adafruit Industries, New York, NY, USA) to detect the changes on-the-fly (while flying). The sensor is equipped with two photo-diodes and is sensitive to the visible and near-infrared radiation spectrum (~350–900 nm). It is connected to the camera system via an i2c interface and read-out every time before image acquisition. To avoid angular effects of the radiation's geometry, the sensor is covered with an ordinary ping-pong ball, which serves as a cosine corrector to diffuse the incoming radiation (see, *i.e.*, Figure 2a).

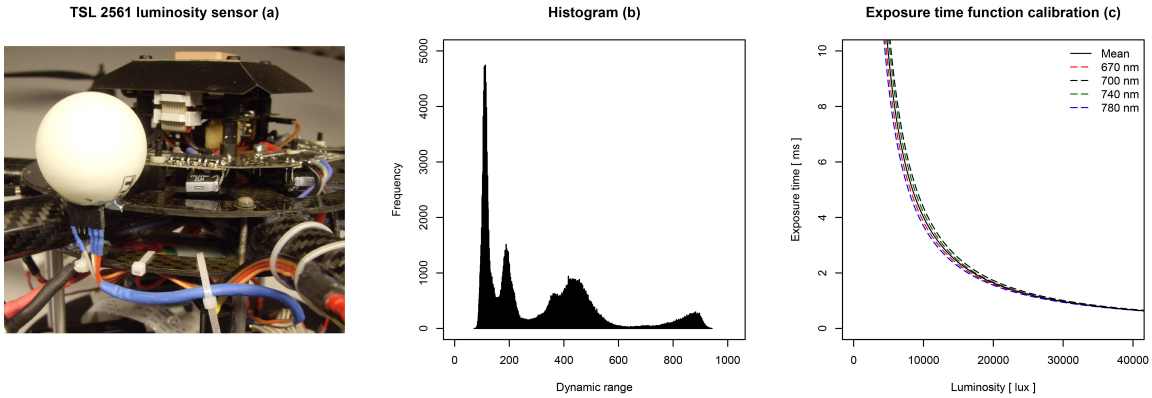

Figure 2. Carrier platform "Hexe" with an attached TSL 2561 luminosity sensor, covered by a ping-pong ball, which serves as a radiation diffuser (**a**); exemplary histogram of a calibration image comprising soil, vegetation, bright and shadowed areas (**b**); exposure time calibration functions for each sensor/filter combination and the final mean exposure time calibration function (**c**).

To estimate optimal exposure time, several imagery sets were acquired under variable radiation conditions. The camera was set up on a platform 5 m above-ground and targeted towards two white and black reference targets in a scene comprising soil, vegetation, bright and shadowed areas, representing a typical surrounding for in-field operation. Images were acquired in an automatic loop, incrementing the exposure time from a fraction of a ms (under-exposure) to 10 ms (over-exposure). For each image, exposure time and luminosity sensor readings were saved for analysis. The procedure was performed from morning to evening during different days in late spring. The imagery sets were analyzed for their histogram stretch. Images without under- or over-exposure (clipping) and a spread of $\geq$60% of the 10-bit dynamic range were selected as valid (see Figure 2b). Approximately 2500 images were selected per band. Corresponding exposure times and luminosity readings were regressed for each band individually by a power function (see Figure 2c). All functions follow the same trend and increasingly converge for higher luminosity values. As bigger differences only appear at relatively dark ambient conditions, all functions were averaged to a mean exposure time function for all four sensor/filter combinations.

2.1.2. Sensitivity, Vignetting and Lens Distortion

After image acquisition, the images receive radiometric and geometric corrections, accounting for their specific sensor/filter/lens combination [35]. First, the images undergo two radiometric corrections: (i) compensation of the image sensor's change in sensitivity at different wavelengths;

and (ii) the correction of vignetting, the radial reduction of brightness towards the image borders [35]. Second, a geometric correction is performed to remove the rectilinear projection error, which is caused by the lens system [36]. All correction parameters are system constants and need to be determined only once or after system changes.

To reduce the effect of sensitivity on the radiometric intensity of all images, the sensors' quantum efficiency (QE_{nm}) values (see Table 1) were used to calculate correction factors for a radiometric normalization. In this setup, the sensor's sensitivity is lowest in the near-infrared band (QE_{780} ~41%). This value was used as a reference for the calculation of the correction factors of all other images ($f_{QE} = QE_{780}/QE_{nm}$). In the acquisition loop, these factors are applied to the radiometric intensities of the images at 670, 700 and 740 nm before performing the vignetting correction. In order to quantify the effect of vignetting, the brightness gradient from each image center to the borders was determined by capturing a white target with defined reflectivity (~99%). The images were acquired on a cloudy day under the assumption of diffuse light conditions. The radiometric intensities of these reference images were, again, normalized to the mean reflection in the image and then inversed to create a correction factor matrix for each band. The matrices are applied to the captured images as a second radiometric correction. This correction does not only account for vignetting effects, but also for flaws of the sensor, lens and filter [35]. In the next step, the geometric distortion, deriving from the lens system, is corrected. Lens systems typically cause rectilinear projection errors, which need to be removed to preserve linear objects as straight lines [36]. Therefore, the parameters of distortion were estimated by camera calibration with the software Agisoft Lens 0.4.1 (Agisoft LLC, St. Petersburg, RU). These parameters are used to re-sample the images to a rectilinear projection as a first geometric correction.

2.1.3. Image-To-Image Registration

In the last step, the four individual images are geometrically aligned, cropped to a common extent and stacked to a multi-layered image. The implemented image-to-image registration procedure utilizes a perspective transformation to re-sample the images into a common coordinate system [37]. The transformation and cropping parameters were determined experimentally. The camera system was triggered at altitudes of 10 and 20 m above a sports ground facing a pattern of lines. The captured images were corrected for the lens distortion effects and, consequently, manually registered to identify the transformation parameters for image-to-image registration and cropping. As the optical axes of the lens systems were not aligned perfectly parallel, the parameters of projection vary for different distances [37]. As a consequence, the results of the manual registration were used to create a function of distance to calculate the parameters for any flight altitude, assuming a nadir view. The registration, therefore, depends on a measure of distance, which is provided as flight altitude by the UAS's control unit.

2.2. Carrier Platform

The camera system was installed on "Hexe", a modified MikroKopter (HiSystems GmbH, Moormerland, Germany) Hexa XL aerial carrier platform (see Figure 1a). "Hexe" is an unmanned aircraft system with standard multi-copter navigation capabilities. It is equipped with an inertial measurement unit (IMU) and a differential global navigation satellite system (GNSS) receiver. Moreover, it features an additional accelerometer to improve altitude accuracy. It can be assembled with a payload of ~1 kg and is powered by a 5000 mAh lithium polymer battery for an operation time of approximately 10 min. "Hexe" offers on-board sensor control and sensor data processing by a software framework, running on a Raspberry Pi 1 Model B single-board computer (Raspberry Pi Foundation, Caldecote, UK). The framework retrieves the navigation data and all sensor measurements for on-board data fusion, logging and broadcasting [38]. It shares the navigation information, *i.e.*, the altitude, with the attached camera system. In addition to the multispectral camera system, "Hexe" was equipped with a simple RGB camera with a resolution

of 2592 × 1944 pixels (Raspberry Pi Foundation, Caldecote, UK). Both systems were installed on a roll- and pitch-stabilized gimbal to ensure a best-possible nadir view.

2.3. Field Trial

The camera system was tested on a field trial, established at the Ihinger Hof (48.74° N, 8.92° E), a research station of the University of Hohenheim. The region has a temperate climate with an annual average temperature of 7.9 °C and an average precipitation of 690 mm. This season had 1266 growing degree days with an average winter temperature of 3.3 °C and an average summer temperature of 16.0 °C. The field trial was laid out on silty clay soil, comprising an area of 840 m^2. One cultivar of winter wheat ("Pamier") was treated with seven N fertilization levels of 0, 4, 8, 12, 16, 20 and 24 $g \cdot m^{-2}$ in a randomized complete block design with three replicates. Figure 3 gives an overview of the 21 plots, each of a size of 10 × 4 m. The total amount of N was split into three dressings and applied at growth stages Z 20, Z 31 and Z 51 (see Table 2) [39]. The growth stages correspond to the beginning of tillering, the beginning of stem elongation and the beginning of ear emergence, respectively. An analysis of soil N before the first dressing showed a uniform level of 1.6 $g \cdot m^{-2}$ for all plots. Plant protection followed common practice.

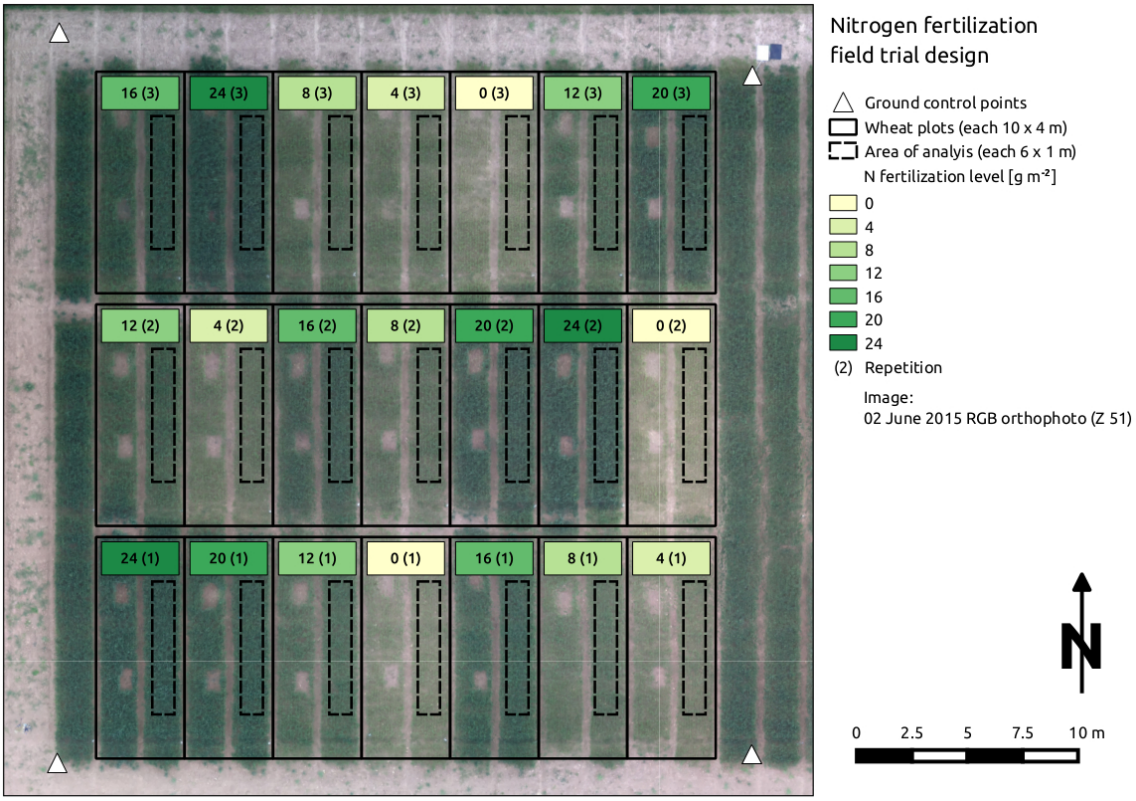

Figure 3. N field trial in winter wheat with 21 plots of a size of 10 × 4 m each. Seven N fertilization levels of 0, 4, 8, 12, 16, 20 and 24 $g \cdot m^{-2}$ were tested in a randomized complete block design with three replicates.

Table 2. Overview of the applied N dressings for each treatment (N_x) at different growth stages (Z) and the accumulated precipitation (P) since the last dressing.

Date	Z	N_0	N_4	N_8	N_{12} (g·m^{-2})	N_{16}	N_{20}	N_{24}	P (mm·m^{-2})
20 March 2015	20	0	2	3	4	6	8	10	
24 April 2015	31	0	2	3	4	6	8	10	43.8
26 May 2015	39–41								70.7
2 June 2015	51								79.7
5 June 2015	51	0	0	2	4	4	4	4	79.7
10 June 2015	61								46.0
17 June 2015	69								46.4
5 August 2015	90								104.3

2.4. Measurements

Four flight missions were performed during mid-season crop development. The missions were conducted 10 and 3 days before, as well as 5 and 12 days after the third N dressing (Z 39–41, Z 51, Z 61, Z 69). The growth stages correspond to the end of stem elongation, the beginning of ear emergence, the beginning of anthesis and the end of anthesis. The flight missions comprised the N field trial and an adjacent field trial, covering a total area of approximately 2500 m^2. The adjacent field trial is not part of this study. The white reference target was laid out beside the plots. Aerial images were acquired at a scheduled flight altitude of 25 m, a forward lap of 95%, a side lap of 60% and a desired ground resolution of 0.04 m·px^{-1}. The azimuthal orientation at image acquisition was constant during the missions (~320°). The image processing loop (see Figure 1c) was performed during flight, which resulted in an acquisition rate of approximately 0.25 Hz. Six ground control points were measured with a real-time kinematic GNSS receiver (Trimble Navigation Ltd., Sunnyvale, CA, USA). Table 3 gives an overview of all mission parameters.

Table 3. Overview of the performed flight missions at different growth stages (Z). The table comprises the mission date, the number of images (*n*) for subsequent processing, the scheduled flight altitude (A), the number of ground control points (G), the desired image ground resolution (R), the mission time (T), the weather conditions (W), the solar zenith (Ze) and azimuth angle (Az) and the wind speed (S).

Date	Z	*n*	A (m)	G	R (m·px^{-1})	T	W	Ze (°)	Az (°)	S (m·s^{-1})
26 May 2015	39–41	121	25	6	0.04	10–11 a.m.	clear sky	44	114	2
2 June 2015	51	128	25	6	0.04	10–11 a.m.	clear sky	43	113	3
10 June 2015	61	132	25	6	0.04	2–3 p.m.	clear sky	29	212	2
17 June 2015	69	135	25	6	0.04	2–3 p.m.	clear sky	29	212	1

After every mission, ground-truth information was acquired by destructive sampling of above-ground biomass in an area of 0.6 m^2 per plot. The crops were cut as close to the soil surface as possible, and fresh matter was determined. Probes of the samples were dried to constant mass in a drying cabinet at 80 °C and analyzed for dry matter (DM) and N content. N content was determined by near-infrared spectroscopy (NIRS XDS, FOSS, DK). Harvest took place on 5 August 2015. Again, each plot was sampled in the same way as after the flight missions. The samples were analyzed for grain yield and N content. Grain protein content was derived by multiplication of the N content with a universal conversion factor of 6.25.

2.5. Image Processing

The images were processed to multispectral orthoimages, using the 3D reconstruction software Agisoft PhotoScan Professional Edition 1.1.6 (Agisoft LLC, St. Petersburg, Russia). The images, the ground control point coordinates and the flight log, containing the coarse image locations, were

imported. After the first step of coarse alignment, manual identification of the ground control points was performed to optimize the alignment procedure. In the next step, the 3D scene was reconstructed as a point cloud and triangulated to build a digital elevation model. In the last step, the images were mosaicked to an orthoimage and exported in the GeoTIFF format (WGS84/UTM32N) for each flight mission, individually. The mosaicking method followed the description of Bendig *et al.* [40] utilizing the radiometric information from the best centered image in case of overlap. Color correction was not performed.

Further processing was conducted with the statistical computation software R [41], making use of the "spatial" and "raster" packages [42,43]. The radiometric intensities at the position of the white reflection target were used to compute averaged normalization factors for the four bands. Subsequently, all bands were normalized with these factors to transform the radiometric intensities into reflectance values. According to Equations (1) and (2), the NDVI and REIP layer were calculated for each orthoimage. The field trial's plot information was imported as polygonal shapefile. Each plot was reduced to a size of 6×1 m to account for plot boundary effects (e.g., inaccuracies in fertilization) and for excluding the reference sample areas from analysis (see Figure 3). Consequently, a spatial query was performed to extract the NDVI and REIP values of the raster cells, which fall inside a polygon. For each polygon, a summary statistics was calculated to average the values of the NDVI and the REIP.

2.6. Regression Analysis

In the last step of processing, a simple linear regression analysis was carried out to confirm the multispectral camera system's ability to detect and predict certain parameters of interest. The analysis was split into two parts: (i) a regression analysis to infer the sampled information at each flight mission; and (ii) a regression analysis to predict the sampled information at harvest (Z 90). The averaged NDVI and REIP values served as independent variable. They were used to estimate above-ground biomass and N content, as well as to predict grain yield and grain protein content. The models were evaluated by comparison of the coefficients of determination (R^2), the root mean square error (RMSE), the relative RMSE and the bias. The quality of each model was assessed by leave-one-out cross-validation and the resulting root mean square error of validation (RMSEV).

3. Results

The on-board camera system was able to capture multispectral images for all UAS flight missions. Reference samples were taken and analyzed to ensure the comparison to real ground truth data. The regression analyses indicate valuable first results.

3.1. Image Acquisition Loop

The camera system worked as expected. It performed all steps of the acquisition loop during the flight mission. One iteration, comprising the steps from exposure time definition to image-to-image registration, took approximately 4 s of time. The exposure time function led to an acquisition of images with a contrast stretch $\geq$60% of the 10-bit dynamic range. Due to the approximated mean exposure time function, some images had clipping effects at the white reference target.

Registered multispectral images were cropped to a common extent of 732×464 px and showed a geometrical error in alignment accuracy (see Figure 4). The error was unevenly distributed throughout the image. Objects that were near the image's center showed a smaller displacement in alignment (~2 px), whereas objects at the image's border showed a larger displacement (~6 px).

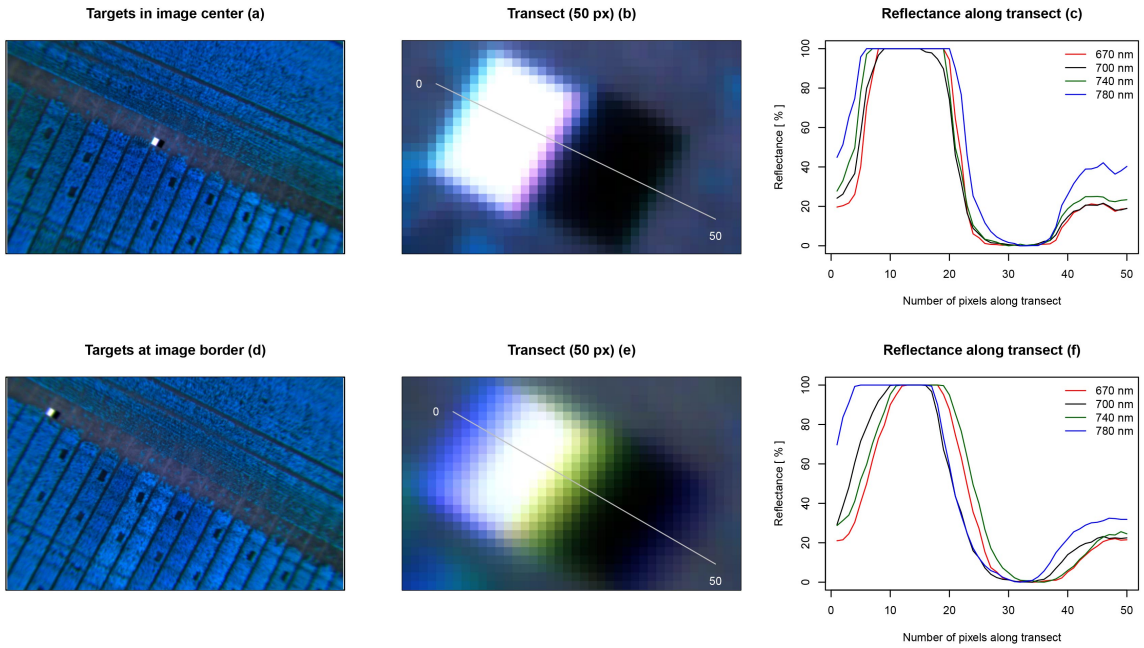

Figure 4. Image-to-image registration accuracy at different locations within the image. Two registered multispectral images are presented as false color images. The first image sets focus on two black and white reference targets (**a**); whereas the second image captures the targets at its border (**d**); two transects of a length of 50 px were selected to investigate the spatial displacement of the four registered bands (**b**,**e**); the reflectance along the transects is shown on the right. The spatial displacement can be observed on the x-axis, and the reflectance can be observed on the y-axis. The figures indicate that the spatial alignment is better in the center of an image (~2 px) (**c**); and it is worse in the border region (~6 px) (**f**).

3.2. Measurements

The laboratory analysis of the samples from Z 39–41 to Z 69 are presented in Table 4. Due to an error in the procedure, one sample could not be analyzed for Z 51 and Z 69, respectively. Average biomass showed an increase from 381.8–1351.3 g·m^{-2} over time. Mean N content was stable at Z 39–41 and Z 51 (1.5 g 100 g^{-1}), decreased at Z 61 (1.2 g 100 g^{-1}) and increased slightly at Z 69 (1.3 g 100 g^{-1}).

Table 4 also shows the results of the samples at harvest (Z 90). Grain yield ranged from 180.4–820.7 g·m^{-2}. The yield increased almost linearly with the amount of fertilized N (see Figure 5a). Grain protein content ranged from 13.7–19.6 g 100 g^{-1}. The protein content did not increase linearly with the amount of fertilized N (see Figure 5b). Its minimum was at an N level of 4 g·m^{-2}, whereas its maximum was reached at a level of 24 g·m^{-2}.

Table 4. Descriptive statistics (minimum, mean, maximum and standard deviation (SD)) of above-ground biomass, N content, grain yield and grain protein content, sampled at different growth stages (Z).

Variable	Z	Minimum	Mean	Maximum	SD
Biomass (DM) (g·m^{-2})	39–41	91.9	381.8	665.5	130.13
	51	241.8	512.1	848.0	165.17
	61	444.4	955.5	1447.3	324.26
	69	486.1	1351.3	2076.0	432.97
N content (g 100 g^{-1})	39–41	1.1	1.5	2.0	0.30
	51	1.1	1.5	2.2	0.36
	61	0.9	1.2	1.9	0.28
	69	0.9	1.3	1.7	0.24
Grain yield (g·m^{-2})	90	180.4	489.7	820.7	178.74
Grain protein content (g 100 g^{-1})	90	13.7	17.0	19.6	1.65

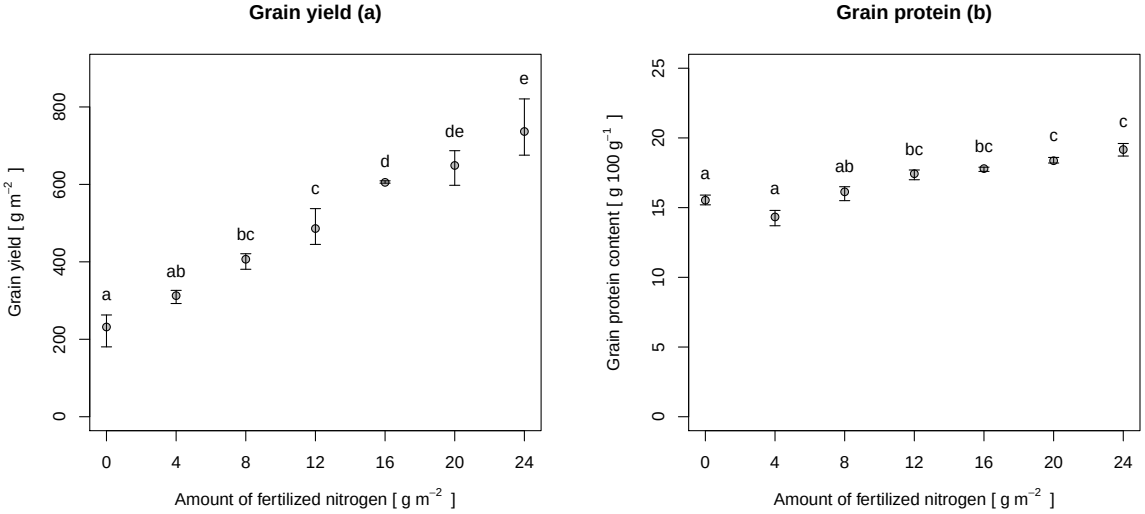

Figure 5. Grain yield (**a**) and grain protein content (**b**) at different levels of fertilization, sampled at harvest (Z 90). The points represent the mean values, whereas the whiskers represent the minima and maxima. Letters indicate the results of a Tukey's HSD multiple comparison test ($\alpha = 0.05$).

3.3. Image Processing

An orthoimage was computed from the acquired aerial imagery for each growth stage. The resulting RMSEs of the ground control point residuals ranged from 0.027–0.032 m in the horizontal and from 0.035–0.046 m in the vertical direction. The orthoimages were produced with a ground resolution of 0.04 m·px^{-1}, leading to an analysis at the canopy level with mixed signals, comprising soil and plant reflection [44]. The signals were used to compute the NDVI and the REIP layer, which were analyzed for the selected plot areas (see Figure 6). At Z 39–61, the average NDVI values were constant around 0.79 with a standard deviation of 0.07 and decreased at Z 69 (0.68 $\pm$ 0.10). The average REIP values were higher for Z 51 and Z 61 (~739 $\pm$ 4.2), whereas they were lower for Z 39–41 and Z 69 (~735 $\pm$ 4.7).

Agriculture **2016**, *6*, 4

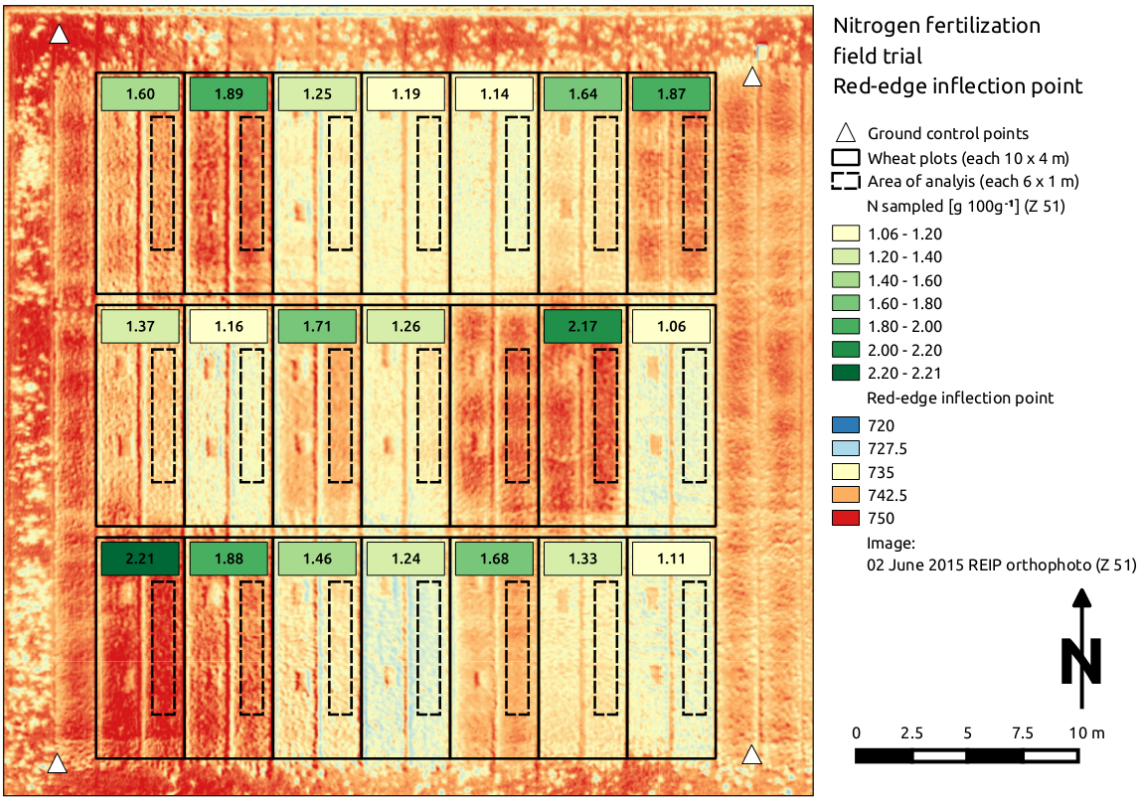

Figure 6. Exemplary red-edge inflection point (REIP) orthoimage with sampled above-ground biomass N content values (g 100 g^{-1}) at growth stage Z 51. One sample is missing due to an erroneous laboratory analysis.

3.4. Regression Analysis

The regression results are grouped by the two aims of this analysis: (i) estimation of biomass and N content; and (ii) prediction of grain yield and grain protein content. All regressions were significant ($p < 0.001$). Table 5 shows the results of the biomass and N content estimation. The table indicates that the NDVI performed better than the REIP. The NDVI estimated the biomass best at Z 39–41, Z 51 and Z 69 with coefficients of determination (R^2) of 0.78, 0.85 and 0.84 and relative RMSE values of 15.7%, 12.3% and 12.3%. The REIP estimated the biomass best at Z 61 with an R^2 of 0.77 and a relative RMSE of 15.8%. Figure 7a displays the regression lines for the NDVI at the different growth stages. The relationship between NDVI and biomass appeared to be linear for all growth stages, whereas the slopes of the regression lines increased with the gain in biomass over time.

For N content estimation, the REIP gave the best results. The R^2 showed values of 0.83, 0.89, 0.81 and 0.58 with relative RMSE values of 8.3%, 7.6%, 10.3% and 11.7% (Z 39–69). The REIP performed best at growth stage Z 51 and worst at growth stage Z 69. The regression plots for the REIP are shown in Figure 7b. The figure indicates a linear relationship of REIP and N content at all growth stages.

Table 6 comprises the results for the prediction of grain yield and grain protein content. The REIP performed better than the NDVI for the prediction of both, grain yield and grain protein content. For grain yield, the REIP showed R^2 values of 0.90, 0.92, 0.91 and 0.94 and relative RMSE values of 11.2%, 9.9%, 10.8% and 9.0%. The NDVI performed slightly worse with R^2 values of 0.89, 0.89, 0.90 and 0.91 and relative RMSE values of 11.6%, 12.1%, 11.0% and 10.9%. Although REIP and NDVI performed well at all growth stages, the prediction performance even improved with time. Figure 8a displays the regression results for the REIP and grain yield, indicating a linear relationship

Agriculture **2016**, *6*, 4

in between the two variables. The regression lines at Z 51 and Z 69 followed a similar pattern, being only translated in parallel at different growth stages. At Z 51, the regression line showed an increased slope.

Table 5. Results of linear regressions ($p < 0.001$) at different growth stages (Z) with the above-ground biomass and N content as the dependent variable (DV), as well as the NDVI and the REIP as the independent variable (IDV). The table comprises the number of samples (n), the coefficient of determination (R^2), the RMSE, the relative RMSE, the bias and the RMSE of validation (RMSEV), derived from a leave-one-out cross-validation.

DV	IDV	Z	n	R^2	RMSE	RMSE (%)	Bias	RMSEV
Biomass (DM) (g·m^{-2})	NDVI	39–41	21	0.78	59.9	15.7	0	66.4
		51	20	0.85	62.8	12.3	0	69.1
		61	21	0.72	168.1	17.6	0	185.4
		69	20	0.84	166.8	12.3	0	179.8
	REIP	39–41	21	0.74	65.1	17.1	0	73.0
		51	20	0.81	69.7	13.6	0	80.4
		61	21	0.77	150.8	15.8	0	167.6
		69	20	0.70	230.6	17.1	0	253.7
N content (g 100 g^{-1})	NDVI	39–41	21	0.75	0.15	10.2	0	0.17
		51	20	0.73	0.18	11.9	0	0.20
		61	21	0.63	0.17	14.3	0	0.19
		69	20	0.53	0.16	12.5	0	0.19
	REIP	39–41	21	0.83	0.12	8.3	0	0.13
		51	20	0.89	0.11	7.6	0	0.13
		61	21	0.81	0.12	10.3	0	0.14
		69	20	0.58	0.15	11.7	0	0.17

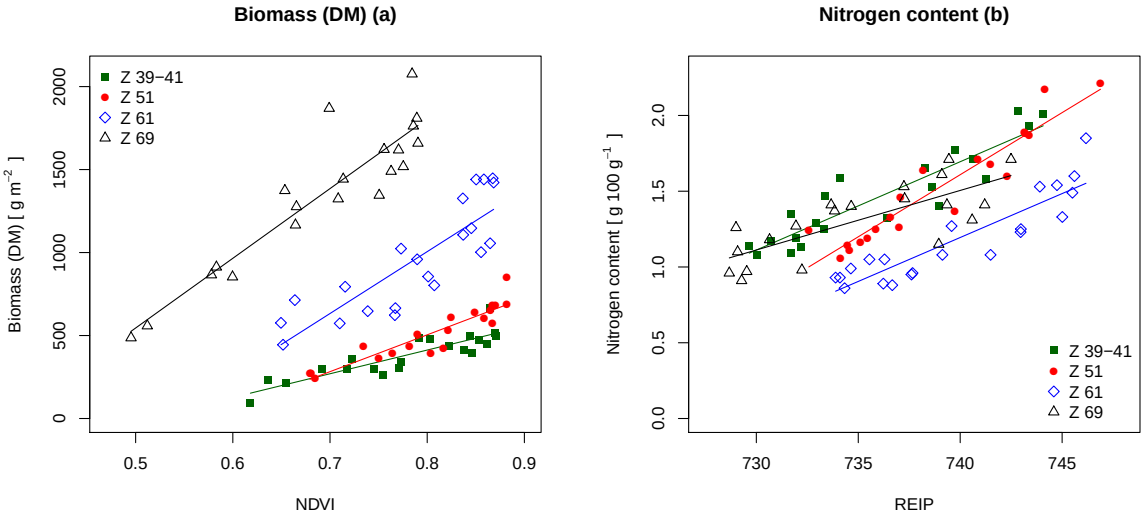

Figure 7. Linear regressions with (**a**) the above-ground biomass as the dependent and the NDVI as the independent variable and (**b**) with the N content as the dependent variable and the REIP as the independent variable at different growth stages (Z). The regression lines are displayed with corresponding colors.

For the prediction of grain protein content, the REIP showed R^2 values of 0.77, 0.76, 0.82 and 0.86 and relative RMSE values of 4.5%, 4.7%, 4.1% and 3.6%. Again, it performed better than the NDVI at

Agriculture **2016**, *6*, 4

all growth stages. Figure 5b shows a nonlinear distribution for the grain protein content. This pattern is also apparent in Figure 8b. The simple linear regressions with the REIP as the independent variable approximated the overall trend of increasing protein content with higher N content. Nevertheless, they could not account for the drop in protein content at low N levels. The lines show a similar pattern as for the grain yield.

Table 6. Results of linear regressions ($p < 0.001$) at different growth stages (Z) with the final grain yield and grain protein content as the dependent variable (DV), as well as the NDVI and the REIP as the independent variable (IDV). The table comprises the number of samples (n), the coefficient of determination (R^2), the RMSE, the relative RMSE, the bias and the RMSE of validation (RMSEV), derived from a leave-one-out cross-validation.

DV	IDV	Z	*n*	R^2	RMSE	RMSE (%)	Bias	RMSEV
Grain yield (g·m^{-2})	NDVI	39–41	21	0.89	56.7	11.6	0	64.5
		51	21	0.89	59.1	12.1	0	65.8
		61	21	0.90	54.1	11.0	0	60.7
		69	21	0.91	53.5	10.9	0	59.9
	REIP	39–41	21	0.90	54.8	11.2	0	60.4
		51	21	0.92	48.3	9.9	0	53.1
		61	21	0.91	52.9	10.8	0	58.7
		69	21	0.94	44.2	9.0	0	49.2
Grain protein content (g 100 g^{-1})	NDVI	39–41	21	0.72	0.86	5.1	0	0.96
		51	21	0.71	0.87	5.1	0	0.99
		61	21	0.72	0.85	5.0	0	0.95
		69	21	0.74	0.83	4.9	0	0.94
	REIP	39–41	21	0.77	0.77	4.5	0	0.84
		51	21	0.76	0.79	4.7	0	0.89
		61	21	0.82	0.69	4.1	0	0.76
		69	21	0.86	0.61	3.6	0	0.68

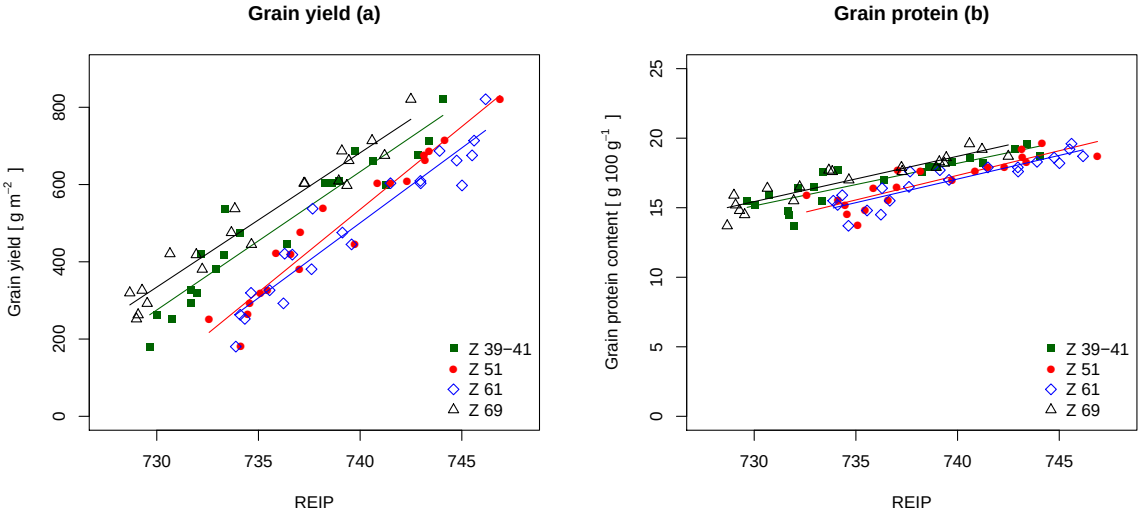

Figure 8. Linear regressions with (**a**) the grain yield and (**b**) the grain protein content as the dependent variable and the REIP as the independent variable at different growth stages (Z). The regression lines are displayed with corresponding colors.

4. Discussion

This study describes a programmable multispectral camera system for in-season aerial crop monitoring. The selected hardware components were successfully integrated into a multi-rotor UAS. The system proved to work in a use case for the estimation of above-ground biomass and N content, as well as for the prediction of grain yield and grain protein content in winter wheat.

4.1. Image Acquisition Loop

The image acquisition loop was able to account for exposure time measurement, image acquisition, radiometric corrections, lens distortion removal and image-to-image registration. Although having implemented a fully-operational system, some improvements may be considered in a future revision.

First, clipping effects occurred in some images at the white reference target. Therefore, an adjustment of the exposure time function is needed to prevent clipping effects in case highly reflective reference targets are used. A more elaborated approach would include a sensor, which registers the incident radiation for each band individually. After radiometric cross-calibration with the imaging sensors, this would not only allow one to set the optimal exposure time, but also to use the information to compute reflectance values without the need of a white reference target.

Second, the system does not account for dark current. Dark current is characterized as a small amount of electric current flowing through an imaging sensor, even at times that the sensor is not exposed to radiation. This electric current adds some noise to each readout of the sensor. Part of the noise is a constant of the electronic components used, whereas the rest of the noise depends on the combination of exposure time and the sensor's temperature [35]. Kuusk [45] describes a method to estimate dark current as a function of exposure time and temperature. Thus, equipping the camera system with a temperature sensor and performing the proposed calibration routine appears to be a valid approach to minimize this noise.

Third, the image-to-image registration procedure shows spatial alignment errors of up to 6 px. This is equivalent to a shift of 0.24 m for images, which were captured at an altitude of 25 m. Although the selected mosaicking routine of the Agisoft PhotoScan 3D reconstruction software makes use of the information from the most centered pixels of an image, one can still assume alignment errors of ~2 px throughout an orthoimage. For measurements of homogeneous dense plant canopies, this can be considered sufficient. For better registration results, more accurate altitude information than the one the UAS's navigation sensors are able to supply is required. In that case, more sophisticated methods like automatic feature detection based image-to-image registration algorithms should be considered [46,47].

Fourth, the processing speed of the image acquisition loop does not allow one to run the complete loop on fixed-wing carrier platforms. As these platforms operate at higher speeds, the current acquisition rate would lead to images without overlap. A possible solution is to perform exposure time measurement and image acquisition on-the-fly, whereas all other steps are carried out in post-processing. This guarantees acquisition rates of more than 1 Hz, which are well suited for fixed-wing operations. Applying this solution would reduce the possibilities that a fully-programmable camera system is generally able to offer to future tasks in the precision agriculture domain. Regarding the opportunities that robotic fleets and real-time data processing raise for automatized crop management [48–50], an improvement in the performance of the processing algorithm and utilization of the digital signal processor on-board the D3 camera platform appears to be better suited, if the system shall be used as a fixed-wing carrier payload.

Finally, all radiometric calibrations were performed in natural environments, assuming optimal conditions. Therefore, calibration in a controlled laboratory environment should be considered. Aasen *et al.* [22], for example, describe a comprehensive method for the calibration of a hyperspectral imaging system.

4.2. Measurements

The field trial was laid out with a wide spread of N fertilization steps to ensure differences in biomass and N content. As expected, the total amount of biomass increased during crop development, whereas the N content decreased due to dilution processes. Although biomass increased over time, the N content at growth stage Z 69 increased slightly compared to Z 61 due to the uptake of the additional N, fertilized in N_8–N_{24} twelve days before. The samples at Z 61 did not show this effect, as the time span of five days was not sufficient to absorb the N.

The differences in treatments became also visible in grain yield and grain protein content. The grain yield increased almost linearly with the amount of fertilized N, clearly distinguishing the treatments from each other. As the maximum treatment probably did not exceed the critical N level, yield loss effects did not occur. The grain protein content shows the expected drop at low N application (N_4) and then increased steadily [13].

4.3. Image Processing

The mosaicked bands of the orthoimages were normalized to the reflection of a white reference target in order to transform the signal intensities into reflectance values for further processing of the NDVI and the REIP. This method has the limitation that the normalization is performed uniformly over the resulting mosaic and not on each image individually. In addition, stable atmospheric conditions during the flight are assumed. A sensor, registering the incident radiation for each band every time at acquisition, could eliminate this drawback and enable the system for real-time analysis (see Section 4.1).

4.4. Regression Analysis

The linear regression analysis proved the operability of the camera system for winter wheat fertilization scenarios. Both parameters, actual above-ground biomass and N content, could be estimated with simple linear regression models at a good level of accuracy. The regression results were compared to an extensive study of Erdle *et al.* [16], which comprises the investigation of four commercially available spectral sensor systems in winter wheat at stem elongation, booting and anthesis in the years 2008 and 2009.

The NDVI appears to be best suited for the estimation of above-ground biomass. The findings indicate that the models were slightly more sensitive before anthesis. Erdle *et al.* [16] describe a similar trend, although their findings indicated bigger differences with higher R^2 values before the beginning of anthesis and smaller ones during the anthesis. This decrease of model accuracy with time is not reflected in the present study, probably due to the pronounced differences in N treatments and a weak occurrence of the typical NDVI saturation at denser crop stands [16,29]. The REIP proved to be a good estimator over all growth stages, as well, showing a trend that is also apparent in Erdle *et al.* [16].

For the estimation of the N content, the REIP performed better than the NDVI. Its R^2 values were high at Z 39–61 and show a reduction at Z 69, a trend that is also observable in Erdle *et al.* [16]. The REIP follows the observation of Collins [51] showing a shift to a longer wavelength during the vegetative period and shift backwards with the onset of senescence. With the chlorophyll content decrease, the canopy's reflection considerably changes [31] and influences the accuracy of the regression model at Z 69.

In addition to the estimation of above-ground biomass and N content, simple linear regressions were conducted to predict grain yield and grain protein content. As N applications before flowering increase mainly grain mass [9], the pronounced differences in N treatment are also apparent in the grain yield data. As a consequence, both REIP and NDVI proved to be good predictors at all growth stages. The results indicate a relatively stable slope of the regression line throughout all models

for both predictors. The models primarily differ in the intercept, depending on the mean canopy reflection at the distinct growth stages.

Grain protein content was predicted best by the REIP, whereas the prediction accuracy increases with time. The models reflect the trend of increasing protein content with a rise in the amount of N, but they cannot account for the drop, which is typical for low N applications [13]. Therefore, the simple linear regression models may be used for the prediction of grain protein content in sufficiently fertilized wheat fields, but should be avoided if N deficiency is present.

Although being comparable to similar studies of canopy reflection, the presented results shall be regarded as indicators, only. As the analysis is based on a single experiment with a wide spread of N treatments and a relative small amount of plots, further research is needed to calibrate this system to be utilized in real-world scenarios.

5. Conclusions

This study introduces a multispectral camera system and demonstrates its ability to estimate above-ground biomass and N content, as well as to predict grain yield and grain protein content in winter wheat. The system was designed as a lightweight payload for a UAS, being fully programmable and customizable for future tasks. It is based on a real-time image processing routine, which proved to cover all steps from exposure time determination, image acquisition, radiometric and geometric image correction and image-to-image registration. The system was successfully tested in a split fertilized N field trial in winter wheat at different growth stages in between the end of stem elongation and the end of anthesis. The acquired multispectral images could be processed to representative NDVI and REIP orthoimages. They were analyzed, using simple linear regression models, which showed good results for the estimation of above-ground biomass with the NDVI (R^2 = 0.72–0.85, RMSE = 12.3%–17.6%) and for the estimation of N content with the REIP (R^2 = 0.58–0.89, RMSE = 7.6%–11.7%). Grain yield could be predicted with both the NDVI and the REIP at a high level of accuracy (R^2 = 0.89–0.94, RMSE = 9.0%–12.1%). Grain protein content was predicted best with the REIP (R^2 = 0.76–0.86, RMSE = 3.6%–4.7%), with the limitation of not being sensitive for low-fertilized canopies. Further research is needed to calibrate the system for real-world scenarios.

The results indicate that a UAS, equipped with this camera system, offers the possibility of acquiring accurate actual canopy information at a large scale. Possible improvements, like the implementation of a sensor to measure ambient solar radiation for each band individually and the enhancement of the calibration and processing routine, enable the UAS to operate within a sensor web-enabled infrastructure for future real-time applications of robotic crop management [48–50,52].

Acknowledgments: The authors acknowledge the Carl-Zeiss Foundation (Carl-Zeiss-Stiftung) for funding this work as part of the collaborative project SenGISat the University of Hohenheim, Stuttgart, Germany. Moreover, the authors acknowledge Andrea Richter, Kevin Leitenberger, Theresa Lehmann and Philipp Pacaud for their field work.

Author Contributions: Jakob Geipel and Jan Wirwahn developed the camera system and performed the calibration measurements. Jakob Geipel processed the orthoimages, conducted the image and regression analysis and wrote the manuscript. Johanna Link set up and performed the field trial, supported the statistical analysis and helped with the manuscript. Wilhelm Claupein helped with editorial contributions.

Conflicts of Interest: The authors declare no conflict of interest.

References

1. Matson, P.A.; Parton, W.J.; Power, A.G.; Swift, M.J. Agricultural Intensification and Ecosystem Properties. *Science* **1997**, *277*, 504–509.
2. Spiertz, J.H.J. Nitrogen, sustainable agriculture and food security. A review. *Agron. Sustain. Dev.* **2010**, *30*, 43–55.
3. Cameron, K.; Di, H.; Moir, J. Nitrogen losses from the soil/plant system: A review. *Ann. Appl. Biol.* **2013**, *162*, 145–173.

4. OECD. *Eutrophication of Waters. Monitoring, Assessment and Control*; Final Report; Organization for Economic Co-Operation and Development (OECD): Paris, France, 1982.
5. WHO. *Guidelines for Drinking-Water Quality, Volume 1: Recommendations;* World Health Organization (WHO): Geneva, Switzerland, 1984.
6. Aufhammer, W. *Getreide- und Andere Körnerfruchtarten: Bedeutung, Nutzung und Anbau*; Ulmer Verlag, UTB für Wissenschaft: Stuttgart, Germany, 1998.
7. McKenna, P. *Report on the Commission Reports on the Implementation of Council Directive 91/676/EEC. Committee on the Environment, Public Health and Consumer Protection (A4-0284/98)*; European Commission: Brussels, Belgium, 1998.
8. Mosier, A.; Kroeze, C.; Nevison, C.; Oenema, O.; Seitzinger, S.; van Cleemput, O. Closing the global N2O budget: Nitrous oxide emissions through the agricultural nitrogen cycle. *Nutr. Cycl. Agroecosyst.* **1998**, *52*, 225–248.
9. Ellen, J.; Spiertz, J. Effects of rate and timing of nitrogen dressings on grain field formation of winter wheat (*Triticum aestivum* L.). *Fertil. Res.* **1980**, *1*, 177–190.
10. Weber, E.; Graeff, S.; Koller, W.D.; Hermann, W.; Merkt, N.; Claupein, W. Impact of nitrogen amount and timing on the potential of acrylamide formation in winter wheat (*Triticum aestivum* L.). *Field Crop. Res.* **2008**, *106*, 44–52.
11. Marino, S.; Tognetti, R.; Alvino, A. Effects of varying nitrogen fertilization on crop yield and grain quality of emmer grown in a typical Mediterranean environment in central Italy. *Eur. J. Agron.* **2011**, *34*, 172–180.
12. Dennert, J. N-Spätdüngung in Winterweizen, um das Ertragspotential auszuschöpfen und die geforderte Qualität zu erreichen; Optimierung von Termin und Menge. Available online: http://roggenstein.wzw.tum.de/fileadmin/Dokumente/ND_sp_07.pdf (accessed on 22 October 2015).
13. Jones, C.; Olson-Rutz, K. Practices to increase wheat grain protein. In *Montana State University Extension*; EBO206; Montana State University: Bozeman, MT, USA, 2012.
14. Houles, V.; Guerif, M.; Mary, B. Elaboration of a nitrogen nutrition indicator for winter wheat based on leaf area index and chlorophyll content for making nitrogen recommendations. *Eur. J. Agron.* **2007**, *27*, 1–11.
15. Mistele, B.; Schmidhalter, U. Estimating the nitrogen nutrition index using spectral canopy reflectance measurements. *Eur. J. Agron.* **2008**, *29*, 184–190.
16. Erdle, K.; Mistele, B.; Schmidhalter, U. Comparison of active and passive spectral sensors in discriminating biomass parameters and nitrogen status in wheat cultivars. *Field Crop. Res.* **2011**, *124*, 74–84.
17. Justes, E.; Mary, B.; Meynard, J.M.; Machet, J.M.; Thelier-Huche, L. Determination of a Critical Nitrogen Dilution Curve for Winter Wheat Crops. *Ann. Bot.* **1994**, *74*, 397–407.
18. Justes, E.; Jeuffroy, M.; Mary, B. *Wheat, Barley, and Durum Wheat*; Springer: Berlin, Germany; Heidelberg, Germany, 1997; pp. 73–91.
19. Auernhammer, H. Precision farming—The environmental challenge. *Comput. Electron. Agr.* **2001**, *30*, 31–43.
20. Van der Wal, T.; Abma, B.; Viguria, A.; Previnaire, E.; Zarco-Tejada, P.; Serruys, P.; van Valkengoed, E.; van der Voet, P. Fieldcopter: Unmanned aerial systems for crop monitoring services. In *Precision Agriculture '13*; Stafford, J., Ed.; Wageningen Academic Publishers: Wageningen, The Netherlands, 2013; pp. 169–175.
21. Thenkabail, P.S.; Lyon, J.G.; Huete, A. Advances in Hyperspectral Remote Sensing of Vegetation and Agricultural Croplands. In *Hyperspectral Remote Sensing of Vegetation*, 1st ed.; Thenkabail, P.S., Lyon, J.G., Huete, A., Eds.; Crc Press Inc.: Boca Raton, FL, USA, 2012; pp. 4–35.
22. Aasen, H.; Burkart, A.; Bolten, A.; Bareth, G. Generating 3D hyperspectral information with lightweight UAV snapshot cameras for vegetation monitoring: From camera calibration to quality assurance. *ISPRS J. Photogramm. Remote Sens.* **2015**, *108*, 245–259.
23. Lelong, C.C.D.; Burger, P.; Jubelin, G.; Roux, B.; Labbe, S.; Baret, F. Assessment of Unmanned Aerial Vehicles Imagery for Quantitative Monitoring of Wheat Crop in Small Plots. *Sensors* **2008**, *8*, 3557–3585.
24. Berni, J.; Zarco-Tejada, P.; Suarez, L.; Fereres, E. Thermal and Narrowband Multispectral Remote Sensing for Vegetation Monitoring From an Unmanned Aerial Vehicle. *IEEE Trans. Geosci. Remote Sens.* **2009**, *47*, 722–738.
25. Hunt, E., Jr.; Dean Hively, W.; Fujikawa, S.; Linden, D.; Daughtry, C.; McCarty, G. Acquisition of NIR-green-blue digital photographs from unmanned aircraft for crop monitoring. *Remote Sens.* **2010**, *2*, 290–305.

26. Primicerio, J.; di Gennaro, S.; Fiorillo, E.; Genesio, L.; Lugato, E.; Matese, A.; Vaccari, F. A flexible unmanned aerial vehicle for precision agriculture. *Precis. Agric.* **2012**, *13*, 517–523.
27. Honkavaara, E.; Saari, H.; Kaivosoja, J.; Pölönen, I.; Hakala, T.; Litkey, P.; Mäkynen, J.; Pesonen, L. Processing and Assessment of Spectrometric, Stereoscopic Imagery Collected Using a Lightweight UAV Spectral Camera for Precision Agriculture. *Remote Sens.* **2013**, *5*, 5006–5039.
28. Lucieer, A.; Malenovsky, Z.; Veness, T.; Wallace, L. HyperUAS–Imaging Spectroscopy from a Multirotor Unmanned Aircraft System. *J. Field Robot.* **2014**, *31*, 571–590.
29. Heege, H.; Reusch, S.; Thiessen, E. Prospects and results for optical systems for site-specific on-the-go control of nitrogen-top-dressing in Germany. *Precis. Agric.* **2008**, *9*, 115–131.
30. Mistele, B.; Schmidhalter, U. Tractor-Based Quadrilateral Spectral Reflectance Measurements to Detect Biomass and Total Aerial Nitrogen in Winter Wheat. *Agron. J.* **2010**, *102*, 499–506.
31. Horler, D.; Dockray, M.; Barber, J. The red edge of plant leaf reflectance. *Int. J. Remote Sens.* **1983**, *4*, 273–288.
32. Guyot, G.; Baret, F.; Major, D.J. High spectral resolution: Determination of spectral shifts between the red and infrared. *ISPRS Int. Arch. Photogramm. Remote Sens.* **1988**, *27*, 750–760.
33. Guyot, G.; Baret, F.; Jacquemoud, S. *Imaging Spectroscopy for Vegetation Studies*; Kluwer Academic Publishers: Dordrecht, The Netherlands, 1992; pp. 145–165.
34. Rouse, J.W., Jr.; Haas, R.H.; Schell, J.A.; Deering, D.W. Monitoring vegetation systems in the Great Plains with ERTS. *NASA Spec. Publ.* **1974**, *351*, 309–317.
35. Mansouri, A.; Marzani, F.; Gouton, P. Development of a protocol for CCD calibration: Application to a multispectral imaging system. *Int. J. Robot. Autom.* **2005**, *20*, 94–100.
36. Brown, D.C. Close-range camera calibration. *Photogramm. Eng. Remote Sens.* **1971**, *37*, 855–866.
37. Brown, L.G. A Survey of Image Registration Techniques. *ACM Comput. Surv.* **1992**, *24*, 325–376.
38. Geipel, J.; Peteinatos, G.G.; Claupein, W.; Gerhards, R. Enhancement of micro Unmanned Aerial Vehicles to agricultural aerial sensor systems. In *Precision Agriculture '13*; Stafford, J.V., Ed.; Wageningen Academic Publishers: Wageningen, The Netherlands, 2013; pp. 161–167.
39. Zadoks, J.C.; Chang, T.T.; Konzak, C.F. A decimal code for the growth stages of cereals. *Weed Res.* **1974**, *14*, 415–421.
40. Bendig, J.; Yu, K.; Aasen, H.; Bolten, A.; Bennertz, S.; Broscheit, J.; Gnyp, M.L.; Bareth, G. Combining UAV-based plant height from crop surface models, visible, and near infrared vegetation indices for biomass monitoring in barley. *Int. J. Appl. Earth Obs.* **2015**, *39*, 79–87.
41. R Core Team. *R: A Language and Environment for Statistical Computing*; R Foundation for Statistical Computing: Vienna, Austria, 2015.
42. Bivand, R.S.; Pebesma, E.; Gomez-Rubio, V. *Applied Spatial Data Analysis with R*, 2nd ed.; Springer: New York, NY, USA, 2013.
43. Hijmans, R.J. *Raster: Geographic Data Analysis and Modeling*; R PackageVersion 2.4-15; 2015.
44. Major, D.J.; Baumeister, R.; Toure, A.; Zhao, S. *Methods of Measuring and Characterizing the Effects of Stresses on Leaf and Canopy Signatures*; ASA Special Publication 66; American Society of Agronomy, Crop Science Society of America, and Soil Science Society of America: Madison, WI, USA, 2003; pp. 81–93.
45. Kuusk, J. Dark Signal Temperature Dependence Correction Method for Miniature Spectrometer Modules. *J. Sens.* **2011**, *2011*, 1–9.
46. Lowe, D.G. Method and Apparatus for Identifying Scale Invariant Features in an Image and Use of Same for Locating an Object in an Image. U.S. Patent 6711293 B1, 23 March 2004.
47. Zitova, B.; Flusser, J. Image registration methods: A survey. *Image Vis. Comput.* **2003**, *21*, 977–1000.
48. Kazmi, W.; Bisgaard, M.; Garcia-Ruiz, F.; Hansen, K.D.; la Cour-Harbo, A. Adaptive Surveying and Early Treatment of Crops with a Team of Autonomous Vehicles. In Proceedings of the 5th European Conference on Mobile Robots ECMR2011, Örebro, Sweden, 7–9 September 2011; Lilienthal, A.J., Duckett, T., Eds.; Örebro University: Örebro, Sweden, 2011; pp. 253–258.
49. Kuhnert, L.; Müller, K.; Ax, M.; Kuhnert, K.D. Object localization on agricultural areas using an autonomous team of cooperating ground and air robots. In Proceedings of the International Conference of Agricultural Engineering CIGR-Ageng2012, International Commision of Agricultural Engineering (CIGR): Valencia, Spain, 2012.
50. Hernandez, A.; Murcia, H.; Copot, C.; de Keyser, R. Towards the Development of a Smart Flying Sensor: Illustration in the Field of Precision Agriculture. *Sensors* **2015**, *15*, 16688–16709.

51. Collins, W. Remote sensing of crop type and maturity. *Photogramm. Eng. Rem. Sens.* **1978**, *44*, 43–55.
52. Geipel, J.; Jackenkroll, M.; Weis, M.; Claupein, W. A Sensor Web-Enabled Infrastructure for Precision Farming. *ISPRS Int. J. Geo Inf.* **2015**, *4*, 385–399.

5 A Sensor Web-Enabled Infrastructure for Precision Farming

Geipel, J., M. Jackenkroll, M. Weis and W. Claupein, 2015. A Sensor Web-Enabled Infrastructure for Precision Farming. *ISPRS International Journal of Geo-Information*, 4(1):385–399.

A UAS is only one of many means for the purpose of data retrieval in future farming environments. A multitude of sensor systems and web-connected sources of information need to be combined to give a more holistic impression of the current crop status and the adequate management operations. Proprietary solutions, which are currently sold by the different agrotechnical vendors, do not aim at data interoperability. This leads to increasing efforts in establishing sophisticated sensor data infrastructures, combining actual and archived sensor measurements from different sources with already generated information. An infrastructure with common standards can overcome this limitation and build a bridge in between sensor networks, agricultural data bases, commercial and public decision services, and farm management information systems.

Having developed a fully functional UAS with real-time processing capabilities (see Section 2–4), another important step of this thesis was to embed the UAS into a sensor data infrastructure, which is presented in this publication. The infrastructure was developed using open source software and the standards of the Open Geospatial Consortium (OGC). Its purpose was to automatize the control of different sensor systems, the retrieval of the sensor measurements, their transmission to web services and their standardized storage in a web-accessible data base in near real-time. It was designed in a way that it is scalable to large scenarios, where a multitude of sensor systems and sensor web services can interact with each other to exchange and process data. The infrastructure was tested in a setup with four exemplary sensor systems, being typical for applications in PF. The setup was able to process measurements from temperature, humidity, radiation, and fluorescence sensing devices and to archive the data in a standardized data base, making them accessible for users and services via networks.

ISPRS Int. J. Geo-Inf. **2015**, *4*, 385-399; doi:10.3390/ijgi4010385

OPEN ACCESS

ISPRS International Journal of
Geo-Information
ISSN 2220-9964
www.mdpi.com/journal/ijgi

Article

A Sensor Web-Enabled Infrastructure for Precision Farming

Jakob Geipel [1,*], Markus Jackenkroll [2], Martin Weis [3] and Wilhelm Claupein [1]

[1] Institute of Crop Science, University of Hohenheim, Fruwirthstr. 23, 70599 Stuttgart, Germany; E-Mail: wilhelm.claupein@uni-hohenheim.de

[2] Institute of Phytomedicine, University of Hohenheim, Otto-Sander-Str. 5, 70599 Stuttgart, Germany; E-Mail: m.jackenkroll@uni-hohenheim.de

[3] Centre for Geodesy and Geoinformatics, University of Applied Sciences (HFT) Stuttgart, Schellingstr. 24, 70174 Stuttgart, Germany; E-Mail: Martin.Weis@hft-stuttgart.de

* Author to whom correspondence should be addressed; E-Mail: jakob.geipel@uni-hohenheim.de; Tel.: +49-711-459-22938; Fax: +49-711-459-22297.

Academic Editors: Georg Bareth, Fei Yuan and Wolfgang Kainz

Received: 30 November 2014 / Accepted: 5 March 2015 / Published: 18 March 2015

Abstract: The use of sensor technologies is standard practice in the domain of precision farming. The variety of vendor-specific sensor systems, control units and processing software has led to increasing efforts in establishing interoperable sensor networks and standardized sensor data infrastructures. This study utilizes open source software and adapts the standards of the Open Geospatial Consortium to introduce a method for the realization of a sensor data infrastructure for precision farming applications. The infrastructure covers the control of sensor systems, the access to sensor data, the transmission of sensor data to web services and the standardized storage of sensor data in a sensor web-enabled server. It permits end users and computer systems to access the sensor data in a well-defined way and to build applications on top of the sensor web services. The infrastructure is scalable to large scenarios, where a multitude of sensor systems and sensor web services are involved. A real-world field trial was set-up to prove the applicability of the infrastructure.

Keywords: Sensor Web Enablement; Open Geospatial Consortium; precision farming; interoperable; open source; 52° N; sensor; UAS; web service

ISPRS Int. J. Geo-Inf. **2015**, *4* **386**

1. Introduction

The use of sensor technologies is more and more applicable in agriculture nowadays. In the domain of precision farming (PF), it is an inevitable aid for the generation of site-specific spatial and temporal information to support crop management strategies [1–3]. Within the last decade, several agricultural machinery and sensor construction companies have established a multitude of sensor systems for sensing soil- and plant-related parameters, as well as for sensing environmental impact factors, influencing the development of the cultivated plants [3]. Most of these sensor systems are designed for: (i) stationary use, e.g., soil moisture sensing networks [4,5]; (ii) hand-held use, e.g., fluorescence and hyper-spectral reflection sensors [6]; or (iii) mobile use on ground-based sensor platforms, e.g., fluorescence, hyper-spectral reflection and ultrasonic sensors, which are mounted on tractors [7–10]. Recent development added the possibility for (iv) mobile use on aerial sensor platforms, e.g., camera systems, which are mounted on unmanned aerial vehicles (UAVs) or unmanned aircraft systems (UASs) [11–13].

Most of these sensor systems are operated with vendor-specific control units, user interfaces and communication protocols. As this varies from sensor system to sensor system, using sensors from different vendors may quickly lead to complex, inconsistent and time-intensive procedures for sensor data storage, processing and distribution. Moreover, many sensor systems are integrated into decision support systems for site-specific online and offline applications and are implemented on tractor terminals, e.g., the Yara N-Sensor (Yara International ASA, Germany) and the GreenSeeker (NTech Industries Inc., Ukiah, CA, USA). Raw data access is not guaranteed in all circumstances, and users are commonly bound to vendor-specific processing routines in order to retrieve and analyze the collected sensor measurements.

To overcome this lack of standardized procedures for sensor control and access, as well as for sensor data encoding and distribution, Nash *et al.* [14] suggest utilizing standards from the Open Geospatial Consortium's (OGC) initiatives to automate agricultural sensor data processing. The OGC Sensor Web Enablement (SWE) initiative bridges the gap between sensors and processing applications, providing a suite of standards "[...] to enable all types of Web and/or Internet-accessible sensors, instruments, and imaging devices to be accessible and, where applicable, controllable via the Web" [15]. It consists of several definitions of "sensor related data in a self-describing and semantically enabled way" [16]. SWE, therefore, can be utilized as the basis for a sensor web, an infrastructure that hides the underlying architecture, the network communication mechanisms and the heterogeneous sensor hardware from the applications built on top [17]. Although most realizations of a sensor web originate in other fields of research and for large-scale scenarios, e.g., oil spill disasters [18], flood management [19] or general risk management [20], recent studies proved the adaptability for the agricultural domain, operating in even smaller contexts [21].

The first implementations for stationary wireless sensor networks (WSNs) proved the potential of this idea for precision agriculture. Some researchers describe improved concepts for decision making processes in agriculture by connecting WSNs with web services as part of a spatial data infrastructure (SDI), building on the SWE specifications [22–24]. Other researchers developed applications, based on these web services, e.g., for online spraying operations, utilizing a web feature service (WFS)

ISPRS Int. J. Geo-Inf. **2015**, *4* **387**

on-the-fly [25]. Having a magnitude of possibilities to combine stationary and mobile, ground-based and aerial, as well as temporary and permanent sensor systems, current sensor networks have become more and more complex. As a consequence, the connection of sensor systems and entire sensor networks with a sensor web needs to be as flexible as possible to facilitate the integration of sensor data into web services and applications.

This study provides a simple, but effective method to embed various sensor systems into a sensor web approach, making their data accessible for applications using well-defined and interoperable standards of the OGC SWE initiative framework. The idea for establishing this method originates from the various field experiments, which were conducted at the agricultural research stations of the University of Hohenheim, Stuttgart, Germany. Many of these experiments involve sensor measurements, but lack a general work flow with standardized mechanisms for the control and access of sensors, as well as the storage and processing of their data. The authors show how to utilize open source software, provided by the 52° North Initiative for Geospatial Open Source Software GmbH (52° N), and adapt it to the needs of PF. A field trial environment was set-up to verify the method in a real use-case scenario for the adoption of SWE for PF-sensing.

2. Materials and Methods

This section gives background information about the principles and the implementation of an actual agricultural sensor infrastructure. The focus was set to publish sensor data to a remotely-distributed SWE infrastructure and make it accessible for researchers and user applications in a well-defined way. The sensor infrastructure of this study was based on the recommendations of Bröring *et al.* [18], who described the implementation of an extended sensor infrastructure stack. The infrastructure stack is shown in Figure 1 and will be explained in the following.

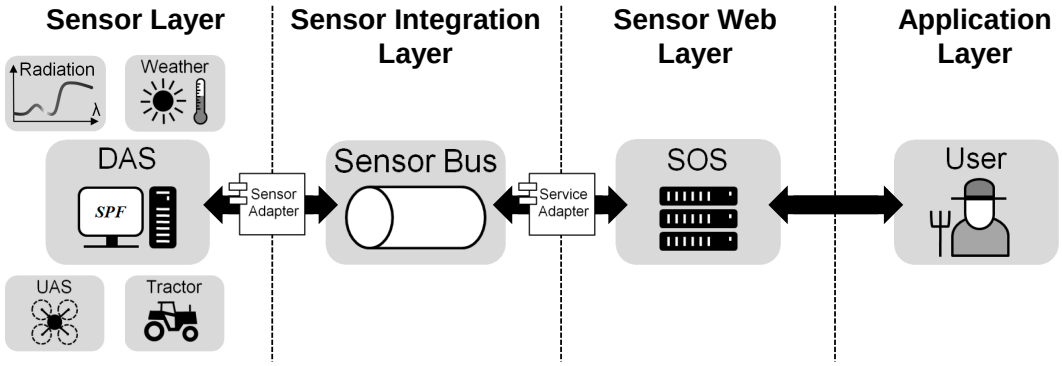

Figure 1. The extended sensor infrastructure stack as introduced by Bröring *et al.* [18]. It is based on three main layers for: (i) sensor control and communication (sensor layer); (ii) Sensor Web Enablement (SWE) services as part of a sensor web (sensor web layer); and (iii) end users and computers (application layer), which build applications on top of the SWE services. A fourth layer is an intermediary integration layer, facilitating the connection of sensors and services (sensor integration layer).

The extended sensor infrastructure stack is based on three main layers and one integration layer, covering all levels from sensor measurements to end-user applications. The sensor layer is the lowest level layer, managing the communication within sensor networks. It consists of the different sensor devices and one or several data acquisition systems (DAS), to control and access all sensor systems on-the-fly. The sensor integration layer is an intermediary layer between sensors and SWE services. Its idea is to establish an infrastructure that connects sensor web services, requesting specific sensor data, with sensors, delivering exactly the requested data, on-the-fly [26]. The sensor web layer consists of one or a multitude of SWE services. Each service is defined for special purposes, e.g., the sensor event service (SES), which offers a web interface to publish and subscribe to notifications from sensors [27], or the sensor observation service (SOS), which offers the discovery and retrieval of real-time or archived data, produced by any kind of sensor system [28]. The application layer is the highest level layer, where users or computer systems interact with the SWE services.

This study proposes an infrastructure that consists of a sensor layer, a sensor integration layer and a sensor web layer. An application layer was not part of this study. The following paragraphs give insight into the implementation of these layers.

2.1. Sensor Layer

The sensor layer represents the lowest level layer of the proposed infrastructure. It was set-up by four different sensor systems and a DAS, to control and access the sensor systems. Communication was enabled by a 2.4-GHz wireless local area network (WLAN) and a 3G mobile Internet connection.

2.1.1. Sensor Systems

The sensor layer involved: (i) a stationary HYT221 weather sensor (HYT221, IST AG, Wattwil, Switzerland) for measuring temperature and relative humidity; (ii) a stationary MMS1 NIR enhanced spectrometer (HandySpec Field, tec5 AG, Oberursel, Germany) for the registration of incident solar radiation; (iii) a tractor, equipped with a Multiplex fluorescence sensor (Multiplex, FORCE-A, Orsay, France) for the detection of within-field plant health; and (iv) Hexe, a prototype UAS, equipped with a PiCam RGB camera (Raspberry Pi Camera, Raspberry Pi Foundation, Caldecote, Cambridgeshire, UK), a self-assembled multi-spectral camera (D3, VRmagic Holding AG, Mannheim, Germany) and an MMS1 NIR enhanced spectrometer, for the detection of plants' spectral parameters [29]. The HandySpec sensor system was operated by a consumer notebook, which also served as the processing unit for the DAS. All other sensor systems were operated by individual Raspberry Pi Model B computers (Raspberry Pi Foundation, Caldecote, Cambridgeshire, UK), which were equipped with wireless adapters to enable communication with the DAS (see Figure 2).

All sensor systems were geo-referenced. The stationary sensor systems were placed at well-known locations, whereas the mobile platforms were equipped with a Global Navigation Satellite System (GNSS) to track their locations on-the-fly. The sensors were controlled by self-developed software routines, implementing vendor-specific application programming interfaces (APIs). The software routines were executed on the Raspberry Pi control units and the notebook.

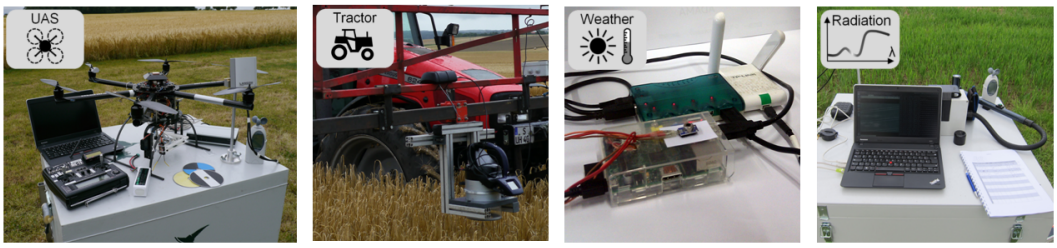

Figure 2. Overview of the sensor systems involved in the sensor layer. From left to right: Hexe (unmanned aircraft system (UAS)), Multiplex fluorescence sensor (tractor), HYT221 weather sensor (weather) and HandySpec Field spectrometer with base station (radiation).

2.1.2. Data Acquisition System

As DAS software, the authors chose the java-based and open source software framework "Sensor Platform Framework" (SPF, https://wiki.52north.org/bin/view/SensorWeb/SensorPlatformFramework). Its main purpose is to gather and, if needed, interpolate sensor data based on a periodic time interval or the availability of certain observations. Its generic architecture supports the inversion of control (IoC) design, offering extension points, which act as interfaces for input and output plugins [30].

Every connection of a sensor system with the DAS was realized by implementing an individual input-plugin and a plugin description document. As all sensor control units and the DAS share the same network, the input-plugins were configured: (i) to establish a network connection to the appropriate sensor control unit; (ii) to send configuration parameters; and (iii) to request sensor observations (see Figure 3).

The plugin description document describes the plugin's interpolation behavior, the sensor's observations and its meta data. The meta data were encoded in SensorML, a sensor description language, which is specified by SWE and used to describe sensors and processes [31]. Table 1 lists the most important parameters of each input plugin.

On the output plugins' side, three output mechanisms were of interest: a visual control of the geo-referenced sensor observations, a mechanism to forward the sensor observations into the sensor web and a simple data logger in case the DAS is disconnected from the sensor web. All of these mechanisms have already been established in three different output plugins, which can be downloaded from the 52°N website and are displayed in Figure 3. Visualization was done by the "SensorVis—Real Time Sensor Visualization" (https://wiki.52north.org/bin/view/SensorWeb/SensorVis) plugin, which allows live visualization of sensor data based on a 3D virtual globe environment [32]. Logging was realized using a slightly adapted version of the "File Writer Plugin", which is part of the standard SPF packages. As the forwarding mechanism, the "Sensor Bus Output Plugin", also distributed within the standard SPF packages, was used. It implements a sensor adapter for a logical bus for the standardized connection of sensor data and SWE services, which will be explained in the following paragraphs [18,26].

ISPRS Int. J. Geo-Inf. **2015**, *4* **390**

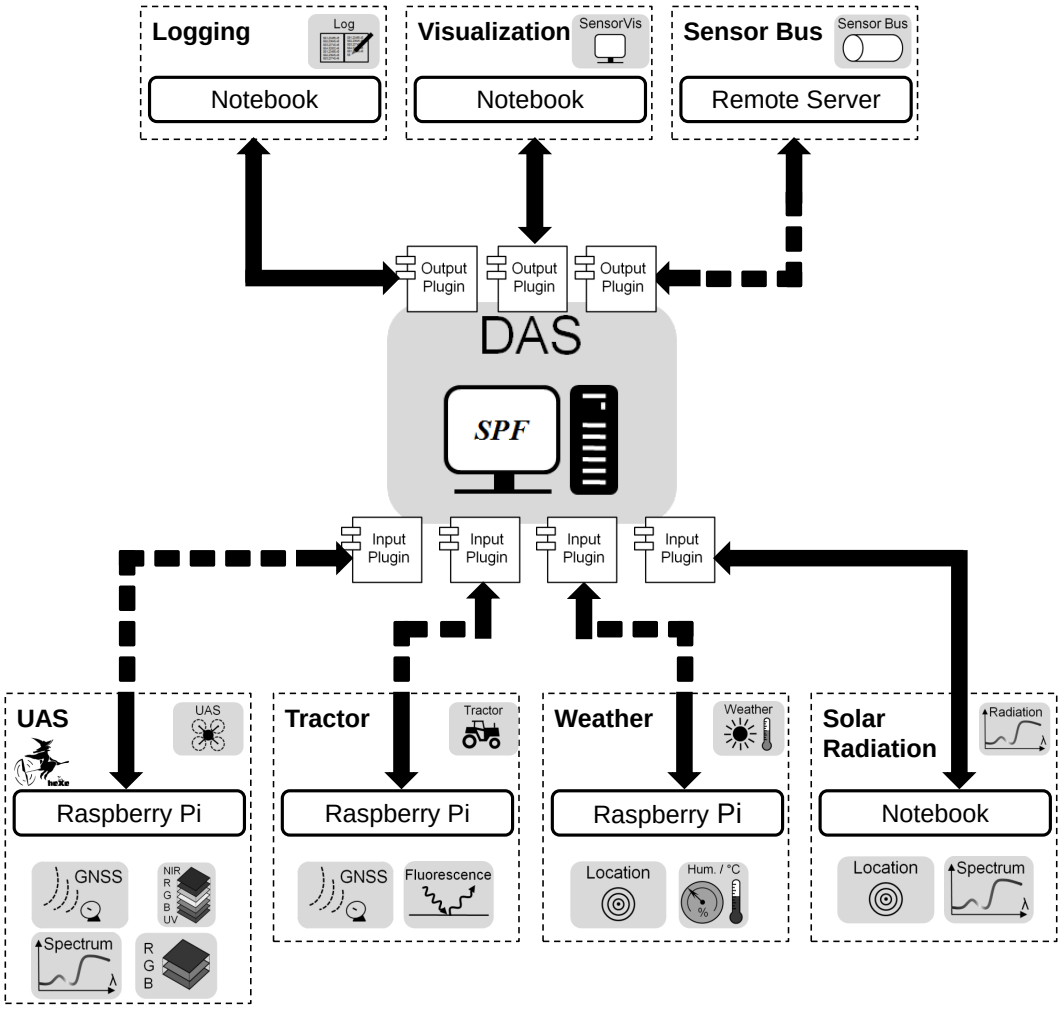

Figure 3. Overview of the input and output plugin architecture of the Sensor Platform Framework (SPF), which serves as the data acquisition system (DAS). Four input plugins were implemented to control and access all sensor systems individually. The Raspberry Pis and the notebook serve as control units, implementing vendor-specific sensor protocols. DAS and control units communicate with each other either through wireless (dashed lines) or wired connections (solid lines). Three output plugins were implemented for: (i) the live-visualization of sensor observations during measurement; (ii) for the local logging of received sensor data; and (iii) for the forwarding of the sensor data into the sensor bus. Visualization and logging were performed on the notebook, running the DAS. Forwarding data into the sensor bus was realized via a mobile Internet connection.

ISPRS Int. J. Geo-Inf. **2015**, *4* **391**

Table 1. Summary of the the sensor systems' observations, specified in the input plugins.

Sensor System	Sensors	Observations
Hexe	GNSS	Lon, Lat, Alt
	IMU	Nick, Roll, Yaw
	MMS1 NIR enhanced	256 reflection values
	PiCam RGB	Image identifier
	VRmagic Camera	Image identifier
Tractor	GNSS	Lon, Lat, Alt
	Multiplex	6 fluorescence indices
Weather	Preset location	Lon, Lat, Alt
	HYT221	Relative humidity
		Temperature
Solar Radiation	Preset location	Lon, Lat, Alt
	HandySpec	256 radiation values

2.2. Sensor Integration Layer

The authors chose the sensor bus to serve as the sensor integration layer in between sensor systems and remotely-connected sensor web services (see Figure 4). Although it is designed to enable a sensor plug and play infrastructure for a sensor web by incorporating semantic matchmaking functionality, a publish/subscribe mechanism and a generic driver mechanism [18], the available sensor bus output plugin is limited to messaging, based on the sensor bus protocol [26]. Therefore, matchmaking, publish/subscribe and driver issues were handled manually.

A driver mechanism to control and access the connected sensors was implemented for every SPF input plugin, individually. The sensor bus plugin was configured to publish all sensor data, gathered by the SPF, into an Extensible Messaging and Presence Protocol (XMPP) chat channel, which ran as ejabberd (https://www.ejabberd.im) software on an Internet-connected server at the University of Hohenheim (see Listing 1). The chat message format follows the sensor bus protocol specifications and offers a simple solution to distribute sensor data to a remote SWE service.

A sensor bus service adapter was implemented to forward the observations from the sensor bus to an SOS. It was realized as a python program. It subscribed and listened to the XMPP chat channel, which contained the published sensor data (see Listing 1). The service adapter was designed to parse the sensor data from the sensor bus protocol format to an SOS request Extensible Markup Language (XML) format. Related sensor observations were assembled and grouped following the predefined SensorML profiles. Subsequently, an *InsertObservation* request was composed to add the observations to the SOS [28]. The *InsertObservation* request is part of the transactional operations SOS profile. This optional transactional profile allows clients to register new sensors (*InsertSensor*) and add observations. Observations in the request are encoded in accordance with the Observations and Measurement (O&M) schema, a standard to describe all observations of a sensor system [33].

Listing 1: Exemplary listing of a sensor bus message, published by the HYT221 weather station. The sensor adapter broadcasts a message to register the sensor (*SensorRegistration*) and publishes all available sensor observations (*PublishData*), consequently.

```
(10:11:58) spf_user2: SensorRegistration>urn:sengis:id:HYT221>urn:sengis:id:HYT221 (stationary platform) connected via SPFramework>
urn:sengis:id:HYT221>
firstCoordinateName<latitude<secondCoordinateName<longitude<thirdCoordinateName<altitude>urn:ogc:def:crs:EPSG::4326>0.0>0.0>0.0>
humidity<%<altitude<m<longitude<deg<latitude<deg<temperature<Cel>SensorRegistration
(10:11:58) spf_user2: PublishData>urn:sengis:id:HYT221>2014−06−27T10:11:57.355+01:00>class java.lang.Double>36.2>humidity>
(10:11:58) spf_user2: PublishData>urn:sengis:id:HYT221>2014−06−27T10:11:57.355+01:00>class java.lang.Double>485.234>altitude>
(10:11:58) spf_user2: PublishData>urn:sengis:id:HYT221>2014−06−27T10:11:57.355+01:00>class java.lang.Double>8.9221>longitude>
(10:11:58) spf_user2: PublishData>urn:sengis:id:HYT221>2014−06−27T10:11:57.355+01:00>class java.lang.Double>48.7450>latitude>
(10:11:58) spf_user2: PublishData>urn:sengis:id:HYT221>2014−06−27T10:11:57.355+01:00>class java.lang.Double>18.54>temperature>
```

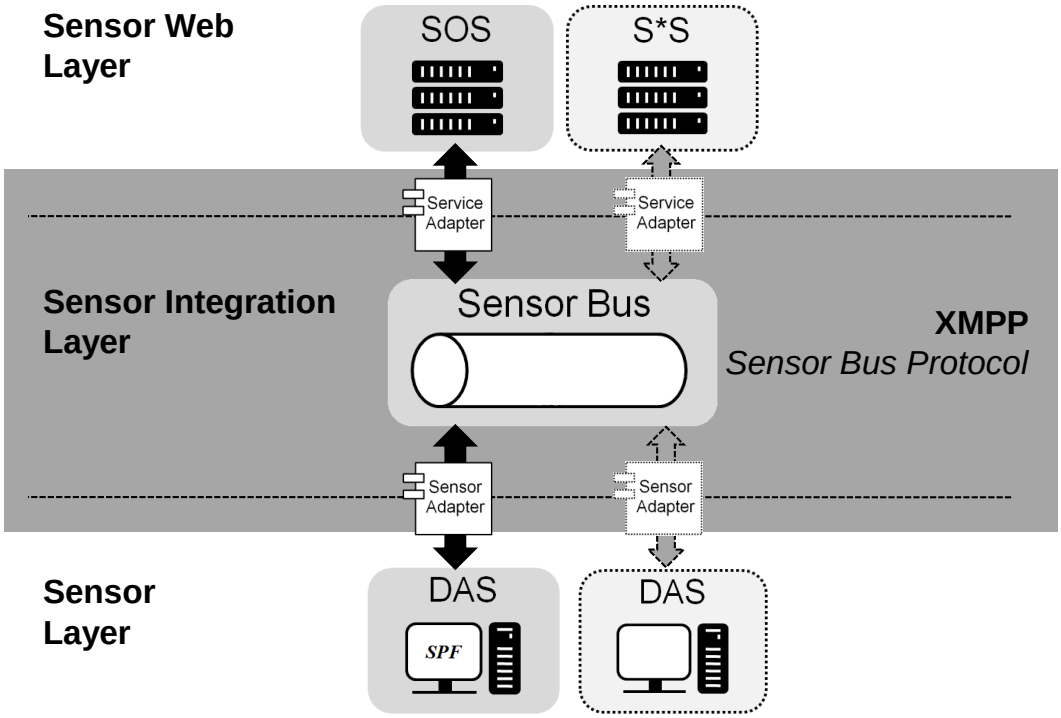

Figure 4. Overview of the sensor bus architecture, which is designed to facilitate the communication of sensor systems and SWE services. Any kind of sensor adapter can register to the bus and publish its sensor data according to the sensor bus message protocol. For subscription and receiving of sensor data, any kind of SWE services can register a service adapter, listening to the sensor bus. The architecture is scalable to scenarios where a multitude of sensor systems and SWE services participate.

2.3. Sensor Web Layer

The sensor web layer consists of an SOS. It is the most common SWE service and it was used in this study in its 52° N SOS 4.1 (https://wiki.52north.org/bin/view/SensorWeb/SensorObservationServiceIV) implementation, exclusively. It was set-up on a server, running at the University of Hohenheim. It offers a web interface for publishing operations, e.g., *GetCapabilities*, *GetObservation* and *DescribeSensor*, on the one hand, and for transactional operations, e.g., *InsertSensor* and *InsertObservation*, on the other hand. It builds on the technical frameworks of an Apache Tomcat 7 (http://tomcat.apache.org/tomcat-7.0-doc) servlet container, a PostgreSQL 9.3 (http://www.postgresql.org/docs/9.3) Database Management System (DBMS) and a PostGIS 2.1 (http://postgis.net/2013/08/17/postgis-2-1-0) support for geographic objects.

Based on the SensorML descriptions of every input plugin, each sensor system was registered once using the *InsertSensor* operation. After having registered the individual sensors, the sensor bus service adapter was able to perform *InsertObservation* operations on-the-fly, using the Service-Oriented Architecture Protocol (SOAP).

2.4. Field Trial

A typical PF field experiment served as test-bed for the proposed infrastructure. The field trial was conducted on 27 June 2014 and in clear skies in a field of winter-wheat (*Triticum aestivum* L.), located at Ihinger Hof (48.74°N, 8.92°E), a research station of the University of Hohenheim. The trial's aim was the acquisition and storage of sensor observations: (i) locally, on a notebook, running the DAS; and (ii) remotely, on an Internet-connected SOS.

The sensor systems were mounted on ground, on a tractor and on a UAS. The tractor and the UAS were configured to follow a predefined route in the field, whereas the weather station and the solar radiation sensor were set-up at fixed locations at the field's border. The consumer notebook, running the DAS, was set-up at the solar radiation sensor's location, together with a 2.4-GHz WLAN access point and a 3G mobile Internet connection, realized by mobile phone tethering. All sensor systems were operated simultaneously with a sampling interval of 1 Hz during a measurement period of approximately 6 min. Observation pull-requests were performed at the same rate via the 2.4-GHz WLAN connection. A maximum distance of 180 m in between the sensor system and notebook was reached by the UAS. The UAS covered a total area of 180 × 36 m.

Visualization and logging of the received observations took place on the notebook. Moreover, broadcasting was performed by the sensor bus plugin via the mobile Internet connection. The sensor bus messaging infrastructure was implemented as an ejabberd XMPP service on an Internet-connected server at the University of Hohenheim. In addition, this server hosted the SOS, as well as the sensor bus service adapter, which was listening to incoming messages of the XMPP chat channel. Figure 5 gives an overview of the complete infrastructure with a UAS observation example.

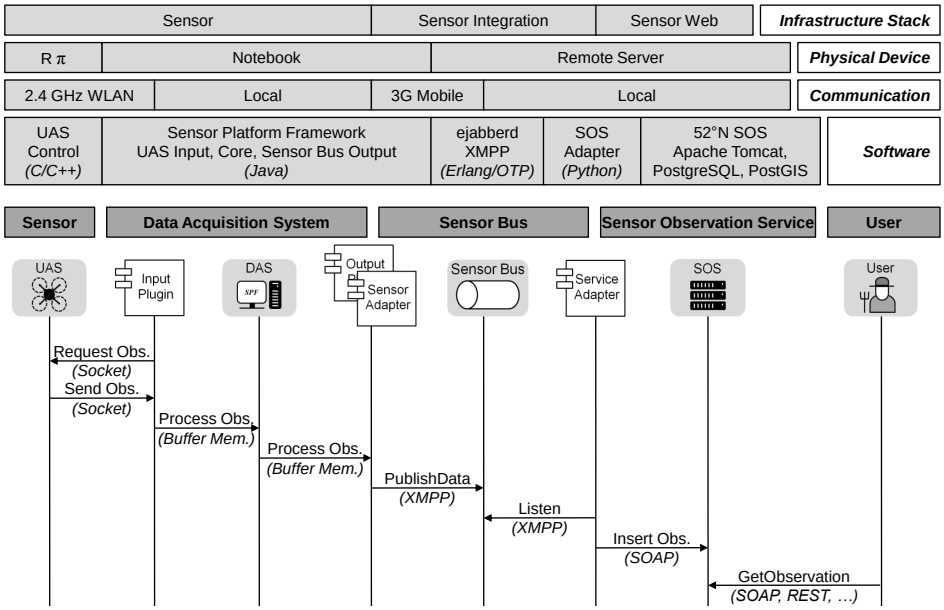

Figure 5. Sequence diagram of the processing of an exemplary UAS observation from acquisition to storage on an Internet-connected SOS (lower half). The upper half gives information about the realization of the different components of the infrastructure.

3. Results and Discussion

The infrastructure proved its ability to control all sensors, to access and forward their data and to store them in a well-defined, standardized SOS. The field trial showed that this sensor infrastructure is applicable to PF scenarios, although some hurdles still exist.

3.1. Sensor Layer

Despite having two connection losses of approximately 10 s due to instabilities of the WLAN, the sensor layer behaved as expected. Under stable network conditions, all sensor systems could be controlled flawlessly. Their data could be accessed by the DAS and forwarded to the sensor integration layer. The mobile Internet connection was stable throughout the whole test.

Intensive work had to be invested in the programming of the control unit software of all sensor devices. The software was designed to keep the sensors remotely controllable and accessible via network socket communication. Every software implementation had to cope with sensor-specific drivers and protocols. Although most sensor vendors offer APIs for software developers, some sensor protocols still have to be implemented by one's self, e.g., the Spectral Device Control and Transfer Protocol (SDCTP) for network control of the MMS1 NIR enhanced spectrometer. A generic driver mechanism, e.g., the sensor interface descriptor (SID) model, could overcome this intensive labor [34].

The SPF, which was used as DAS, served its purpose to integrate all sensor systems. Nevertheless, implementing correct input plugins and plugin descriptions had to be done carefully. Each input plugin

was programmed to connect to a specific network socket to communicate with its according sensor control unit. Sensor data access was implemented with 1-Hz pull requests, which worked reliably, apart from two times of network instability. For configurable sensors, sensor control was realized via a graphical user interface (GUI). Sensor descriptions were realized in a standardized way with SensorML, defining the sensors' characteristics as part of a plugin description document. Moreover, the description document was used to specify the input plugins' interpolation behavior, as well as the input and output of observations. The output plugins worked as expected. Once registered for use, the visualization plugin was able to display all observations from every sensor on-the-fly (see Figure 6). The logging plugin logged all incoming observations to a .csv file. The size of the .csv file summed up to 1.3 MB during 6 min of measurement. The sensor bus output plugin worked flawlessly. It parsed the incoming observations to the sensor bus protocol format and forwarded the data into the XMPP chat channel.

The sensor layer implementation proved its practicability. A stable network and Internet connection is essential for this architecture. Despite potentially missing some of the sensed data due to unpolled pull mechanisms, instabilities may be also critical for near real-time applications in scenarios where data acquisition, data processing and application are performed online.

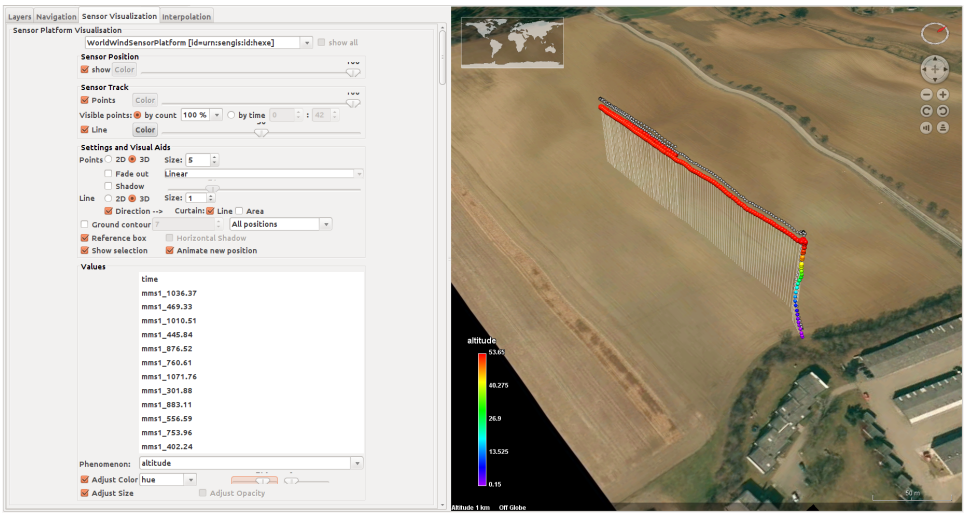

Figure 6. Example of the SPF "SensorVis" output plugin [32] live-visualization of Hexe, a UAS sensor system, operating during the field trial. On the left side, visualization parameters can be selected and configured, depending on the available sensor observations. On the right side, the flight path and the selected sensor observation values are visualized by colored spheres, *i.e.*, indicating the received flight altitude information.

3.2. Sensor Integration Layer

The sensor integration layer was restricted to the sensor bus messaging mechanism, due to the limited functionality of the sensor bus output plugin. It was able to connect to the chat channel and broadcast all sensor data, collected by the DAS. Instead of broadcasting complete raster datasets, e.g., images, the captured raster data description was restricted to short image identifiers. As a consequence, all sensor

datasets could be transmitted through the wireless Internet connection. The data transfer to the XMPP service was not encrypted. Generally, transfer encryption is desirable and available (transport layer security, TLS). If the channel communication should be kept private, it can be restricted to certain users and password authentication.

As this study utilizes only one sensor adapter and one service adapter, the sensor bus architecture is not exploited in all of its possibilities. Nevertheless, the introduced infrastructure offers the scalability of the sensor bus concept. It can be adapted to a multitude of sensor adapters and service adapters, e.g., for multiple SOS and SES, located at different institutions. Moreover, as it is a logical concept, messaging is not restricted to XMPP and can be replaced or extended by other communication protocols, e.g., Twitter and Internet Relay Chat (IRC) [18]. To enable sensor plug and play, mediating, publish/subscribe and driver mechanisms still have to be implemented.

3.3. Sensor Web Layer

The sensor web layer performed well. The Apache Tomcat server, as well as the PostgreSQL/PostGIS DBMS were installed smoothly, following the documented standard installation routines. The SOS package was delivered as a self-extracting file for the servlet container. The installation worked as expected. All needed databases were created automatically after SOS configuration. The SOS supported all operations of the implemented SOS service adapter. Here, *InsertSensor* and *InsertObservation* were used.

4. Conclusions

This work proved the applicability of the OGC SWE initiative framework definitions for the set-up of a sensor data infrastructure for PF applications. The proposed infrastructure guarantees a standardized collection and storage of spatio-temporal agricultural sensor data, accessible by SWE services and user applications. It is based on open source software, offering the possibility to deploy numerous sensor systems and SWE services. The DAS provides a consistent method for the control, access and forwarding of sensor observations. The sensor bus concept is scalable to more complex scenarios involving a multitude of sensor systems, DAS and SWE services. The implemented SOS is a first step towards a service-oriented architecture, based on further web services and OGC standards, offering functionalities of a holistic SDI for PF. In an SDI, web clients act as interfaces in between stored sensor data and a user, realizing the application layer of the infrastructure stack. It can be applied to machinery and sensor systems on the farm scale or be extended with data services offered by external parties. Moreover, as observations acquired by mobile or stationary systems share the same infrastructure, the applications and work flows built on top of it can themselves be built for mobile or stationary devices. Future research will be concentrated on establishing such an SDI for standardized sensor data distribution, processing and analysis in the PF domain.

Acknowledgments

The authors acknowledge the Carl-Zeiss-Foundation (Carl-Zeiss-Stiftung) for funding this work as part of the collaborative project SenGIS, at the University of Hohenheim, Stuttgart, Germany. Moreover, the authors acknowledge Arne Bröring, Matthes Rieke, Daniel Nüst, Christian Malewski and Jan Wirwahn for their advice and support in the implementation of this infrastructure.

Author Contributions

Jakob Geipel and Martin Weis proposed the idea for this work. Jakob Geipel wrote the manuscript, and programmed the control units and the input plugins of the sensor layer. Markus Jackenkroll set up the server, the DBMS and the SOS of the sensor web layer. Martin Weis programmed the sensor bus service adapter of the sensor integration layer. Jakob Geipel, Markus Jackenkroll, and Martin Weis performed the field work. Wilhelm Claupein helped with editorial contributions.

Conflicts of Interest

The authors declare no conflicts of interest.

References

1. Oerke, E.C.; Gerhards, R.; Menz, G.; Sikora, R.A.; Eds. *Precision Crop Protection—The Challenge and Use of Heterogeneity*, 1st ed.; Springer Verlag: Dordrecht, The Neatherlands, 2010.
2. Heege, H.J.; Eds. *Precision in Crop Farming: Site Specific Concepts and Sensing Methods: Applications and Results*, 1st ed.; Springer Science & Business Media: Dordrecht, The Neatherlands, 2013.
3. Peteinatos, G.G.; Weis, M.; Andújar, D.; Rueda Ayala, V.; Gerhards, R. Potential use of ground-based sensor technologies for weed detection. *Pest Manag. Sci.* **2014**, *70*, 190–199.
4. Phillips, A.J.; Newlands, N.K.; Liang, S.H.; Ellert, B.H. Integrated sensing of soil moisture at the field-scale: Measuring, modeling and sharing for improved agricultural decision support. *Comput. Electron. Agric.* **2014**, *107*, 73–88.
5. Li, Z.; Wang, N.; Franzen, A.; Taher, P.; Godsey, C.; Zhang, H.; Li, X. Practical deployment of an in-field soil property wireless sensor network. *Comput. Stand. Interfaces* **2014**, *36*, 278–287.
6. Peteinatos, G.G.; Geiser, M.; Kunz, C.; Gerhards, R. Multisensor approach to identify combined stress symptoms on spring wheat. In Proceedings of the 2nd International Conference on Robotics and Associated High-Technologies and Equipment for Agriculture and Forestry, Madrid, Spain, 21–23 May 2014; Gonzalez-de-Santos, P., Ribeiro, A., Eds.; pp. 131–140.
7. Martinon, V.; Fadailli, E.M.; Evain, S.; Zecha, C. Multiplex: An innovative optical sensor for diagnosis, mapping and management of nitrogen on wheat. In *Precision Agriculture 2011*, Proceedings of the ECPA, Prague, Czech Republic, 11–14 July 2011; Stafford, J., Ed.; Czech Centre for Science and Society: Prague, Czech Republic, 2011; pp. 547–561.
8. Tremblay, N.; Wang, Z.; Ma, B.L.; Belec, C.; Vigneault, P. A comparison of crop data measured by two commercial sensors for variable-rate nitrogen application. *Precis. Agric.* **2009**, *10*, 145–161.

9. Andújar, D.; Weis, M.; Gerhards, R. An ultrasonic system for weed detection in cereal crops. *Sensors* **2012**, *12*, 17343–17357.
10. Escolá, A.; Andújar, D.; Dorado, J.; Fernández-Quintanilla, C.; Rosell-Polo, J.R. Weed detection and discrimination in maize fields using ultrasonic and lidar sensors. In Proceedings of the International Conference of Agricultural Engineerig CIGR, Valencia, Spain, 8–12 July 2012.
11. Thenkabail, P.S.; Lyon, J.G.; Huete, A. Advances in hyperspectral remote sensing of vegetation and agricultural croplands. In *Hyperspectral Remote Sensing of Vegetation*, 1st ed.; Thenkabail, P.S., Lyon, J.G., Huete, A., Eds.; CRC Press Inc.: Boca Raton, FL, USA, 2012; pp. 4–35.
12. Berni, J.; Zarco-Tejada, P.; Suarez, L.; Fereres, E. Thermal and narrowband multispectral remote sensing for vegetation monitoring from an Unmanned Aerial Vehicle. *IEEE Trans. Geosci. Remote Sens.* **2009**, *47*, 722–738.
13. Geipel, J.; Link, J.; Claupein, W. Combined spectral and spatial modeling of corn yield based on aerial images and crop surface models acquired with an unmanned aircraft system. *Remote Sens.* **2014**, *6*, 10335–10355.
14. Nash, E.; Korduan, P.; Bill, R. Applications of open geospatial web services in precision agriculture: A review. *Precis. Agric.* **2009**, *10*, 546–560.
15. Botts, M.; Percivall, G.; Reed, C.; Davidson, J. OGC sensor web enablement: Overview and high level architecture. In *GeoSensor Networks*; Nittel, S., Labrinidis, A., Stefanidis, A., Eds.; Springer: Berlin/Heidelberg, Germany, 2008; Volume 4540, pp. 175–190.
16. Botts, M.; Percivall, G.; Reed, C.; Davidson, J. *OGC Sensor Web Enablement: Overview and High Level Architecture (White Paper) (OGC 06-050r2)*; OGC Implementation Specification: Wayland, MA, USA, 2013.
17. Bröring, A.; Echterhoff, J.; Jirka, S.; Simonis, I.; Everding, T.; Stasch, C.; Liang, S.; Lemmens, R. New generation sensor web enablement. *Sensors* **2011**, *11*, 2652–2699.
18. Bröring, A.; Maué, P.; Janowicz, K.; Nüst, D.; Malewski, C. Semantically-enabled sensor plug & play for the sensor web. *Sensors* **2011**, *11*, 7568–7605.
19. Bröring, A.; Beltrami, P.; Lemmens, R.; Jirka, S. Automated integration of geosensors with the sensor web to facilitate flood management. In *Approaches to Managing Disaster—Assessing Hazards, Emergencies and Disaster Impacts*; Tiefenbacher, J., Ed.; InTech: Rijeka, Croatia, 2012; pp. 65–86.
20. Klopfer, M.; Ioannis, K.; Eds. *Orchestra—An Open Service Architecture for Risk Management*; ORCHESTRA Consortium, 2008. Available online: http://www.eu-orchestra.org/docs/ORCHESTRA-Book.pdf (accessed on 13 November 2014).
21. Wiebensohn, J.; Jackenkroll, M. Evaluation and modelling of a standard based spatial data infrastructure for precision farming. In Proceedings of the EFITA-WCCA-CIGR Conference, Turino, Italy, 24–27 June 2013; p. C0107.
22. Polojärvi, K.; Koistinen, M.; Luimula, M.; Verronen, P.; Pahkasalo, M.; Tervonen, J. Distributed system architectures, standardization, and web-service solutions in precision agriculture. In Proceedings of the 4th International Conference on Advanced Geographic Information Systems, Applications and Services, Valencia, Spain, 30 January–4 February 2012; pp. 171–176.

23. Sawant, S.; Adinarayana, J.; Durbha, S.; Tripathy, A.; Sudharsan, D. Service oriented architecture for wireless sensor networks in agriculture. In *International Archives of the Photogrammetry, Remote Sensing and Spatial Information Sciences*, Proceedings of the ISPRS Congress, Melbourne, Australia, 25 August–1 September 2012; pp. 467–472.
24. Kubicek, P.; Kozel, J.; Stampach, R.; Lukas, V. Prototyping the visualization of geographic and sensor data for agriculture. *Comput. Electron. Agric.* **2013**, *97*, 83–91.
25. Kaivosoja, J.; Jackenkroll, M.; Linkolehto, R.; Weis, M.; Gerhards, R. Automatic control of farming operations based on spatial web services. *Comput. Electron. Agric.* **2014**, *100*, 110–115.
26. Bröring, A.; Foerster, T.; Jirka, S.; Priess, C. Sensor bus: An intermediary layer for linking geosensors and the sensor web. In *COM.Geo '10*, Proceedings of the 1st International Conference and Exhibition on Computing for Geospatial Research & Application, Bethesda, MD, USA, 21–23 June 2010; ACM: New York, NY, USA; pp. 12:1–12:8.
27. Echterhoff, J.; Everding, T. *OpenGIS Sensor Event Service Interface Specification (Discussion Paper) (OGC 08-133)*; OGC Implementation Specification: Wayland, MA, USA, 2008.
28. Na, A.; Priest, M. *Sensor Observation Service (OGC 06-009r6)*; OGC Implementation Specification: Wayland, MA, USA, 2007.
29. Geipel, J.; Peteinatos, G.G.; Claupein, W.; Gerhards, R. Enhancement of micro Unmanned Aerial Vehicles to agricultural aerial sensor systems. In *Precision Agriculture '13*, Proceedings of the ECPA, Lleida, Spain, 7–11 July 2013; Stafford, J., Ed.; Wageningen Academic Publishers: Wageningen, The Neatherlands, 2013; pp. 161–167.
30. Rieke, M.; Foerster, T.; Bröring, A. Unmanned Aerial Vehicles as mobile multi-sensor platforms. In Proceedings of the 14th AGILE International Conference on Geographic Information Science, Utrecht, The Neatherlands, 18–21 April 2011.
31. Botts, M.; Robin, A. *OpenGIS Sensor Model Language (SensorML) (OGC 07-000)*; OGC Implementation Specification: Wayland, MA, USA, 2007.
32. Nüst, D. Visualising interpolations of mobile sensor observations. In Proceedings of the GeoViz, Hamburg, Germany, 5–8 March 2013.
33. Cox, S. *Observation and Measurements—XML Implementation (OGC 10-025rl)*; OGC Implementation Specification: Wayland, MA, USA, 2011.
34. Bröring, A.; Below, S.; Foerster, T. Declarative Sensor Interface Descriptors for the Sensor Web. In Proceedings of the WebMGS 2010: 1st International Workshop on Pervasive Web Mapping, Geoprocessing and Services, Como, Italy, 26–27 August 2010.

6 Discussion

This thesis was conducted to develop a UAS for the purpose of PF management support and set focus to five major aspects: (i) implementation of an unmanned aerial vehicle, (ii) its improvement to a UAS by adding sensor control, data processing and communication functionality, (iii) the selection and development of appropriate sensors for yield prediction and nitrogen fertilization strategies, (iv) to test the system in example use cases, and (v) to embed the UAS in a standardized sensor data infrastructure.

The subsequent discussion intends to combine these findings and to evaluate the general usability of a UAS in PF practice. The discussion addresses the findings with respect to the current technology, the processing methods in use, their possibilities and limitations.

6.1 Implementation of an unmanned aerial vehicle

The presented micro UAV is a prototype implementation and cannot be bought as a professional ready-to-use system. Colomina and Molina (2014) gave a recent overview of the current research on UAVs and sensor technology. Although there is a trend to utilize more and more professional UAVs, they are still expensive and offer only limited sensor choice and control. Therefore, many researchers still invest time in the development of cheaper and more configurable platforms. A rotary-wing platform was chosen because of its benefit of easy handling, flexible speed, hovering, and vertical take-off and landing. The prototype is comparable to other systems in PF research with an average payload capability and a relatively low flight endurance (Zecha et al., 2013; Colomina and Molina, 2014). The UAV is very versatile in use but prone to wind and rain. It can be piloted by an autopilot, guided by a differential GNSS and features a pitch and roll compensated gimbal to ensure stabilized sensor measurements. The system worked very well, was able to carry all the sensors for the desired tasks and proved to be an excellent tool for close-range remote sensing research in agriculture.

Besides agricultural research, which often requires a relatively stable observer above a field to guarantee good measurements, a rotary-wing UAV is not necessarily the first choice. For wide area missions, fixed-wing platforms are advantageous. In contrast to rotary-wing UAVs, they are aerodynamically shaped and feature higher speeds at a distinct increase in flight endurance. Therefore, fixed-wing platforms appear more practical with regard to scouting applications, which demand to cover large areas in a shortest possible period.

6.2 Improvement to an unmanned aircraft system

As many researchers utilize self-assembled UAVs, they consider them generally as carrier platform. One can state that the use of UASs in PF applications is not common

practice, yet. If sensor data is combined on-the-fly, the most frequent application is to couple a GNSS receiver and a sensor system. Within the last years, some researchers started to combine this with attitude information of the gimbal for more sophisticated bi-directional reflection modeling of their spectral sensors (Hakala et al., 2010; Burkart et al., 2015). Professional vendors identified the need of on-line sensor data processing and started to develop application programming interfaces to enable their carriers to communicate with the sensors (microdrones GmbH, 2015).

The proposed implementation of an embedded processing unit with real-time sensor fusion functionality proved to be an adequate UAV enhancement. The software framework was developed with an input and output plugin-based architecture. In consequence, it was capable of controlling any kind of connected sensor device. Moreover, it was able to retrieve, fuse, log and broadcast all data on-the-fly. Its architecture guarantees flexibility and adaptability to any kind of need.

The broadcasting functionality enables remote control of the sensor devices and data exchange with a ground station. However, it is also the critical component of this setup. The downlink communication is established by wireless local area network techniques and transfers data at typical bandwidths of the Institute of Electrical and Electronic Engineers standard IEEE 802.11. Raster data from imaging sensors are quite large and require high bandwidths. If image capturing is performed at high acquisition rates, broadcasting of the entire data may not be possible. Therefore, image processing onboard the UAS and transfer of the computed result as small information package can be an alternative (Bürkle et al., 2011). Another critical component is the network range, which can be extended by more powerful antennas and repeater stations. Nevertheless, such a setup does not appear to be practical. As mobile network coverage and data bandwidth steadily improve, an exchange of communication technology is a future step to consider.

6.3 Selection and development of sensor systems

The selection of an appropriate sensor system depends on the desired application. A multitude of multi- and hyperspectral systems are in use, whereas the hyperspectral imaging sensors are still rare and expensive (Cubert GmbH, 2015; Rikola Ltd., 2015). Besides the sensor specifications and the spectral resolution, size, weight, and power consumption are the most important parameters, as they have to fit the carrier platform's capabilities (Zhang and Kovacs, 2012).

For the prediction of corn grain yield, several studies have shown a linear relationship in between corn height and yield (Yin et al., 2011a;b). The presented approach in this work was, therefore, based on the usage of CSMs for the estimation of crop heights. Eisenbeiss (2007) and Bendig et al. (2013) already pointed out the possibilities of 3D model generation with UAVs and simple RGB cameras. In consequence, a low-cost consumer grade RGB camera was selected because of its price and its combination of

focal length and sensor size. This camera guarantees images with a detailed ground resolution of 2 $cm\ px^{-1}$ at a typical flight altitude of 50 m. The device is electronically trigger-able and easy to handle, which makes it very suitable for this task.

For the estimation of biomass and nitrogen content in winter wheat, a first approach utilized a hyperspectral sensor system, which has not been presented in this thesis. This approach was inspired by the various commercial ground-based sensing and nitrogen treatment recommendation systems (Erdle et al., 2011). It comprised the development of a hyperspectral aerial point spectrometer as a flying biomass and nitrogen sensor. The idea was to utilize the sensor of a commercial field spectrometer and adapt the methodologies of relative reflection measurements in the VIS and NIR spectrum (Heege et al., 2008). Therefore, the spectrometer was deployed on the UAS and controlled by the central processing unit. The spectrometer's optic was mounted on the gimbal in order to point towards the canopy in a nadir direction of view. A field spectrometer was used as ground reference for the calculation of relative reflection intensities. The aerial spectrometer was synchronized in real-time with the field spectrometer via the ground control station. The setup proved to be able to control both devices and performed measurements at high acquisition rates of approximately 5 Hz. Relative reflection spectra could be computed, but test measurements did not show high correlation with ground-based reference measurements. Burkart et al. (2014) developed a similar system. They found higher correlations, but they performed their flight missions at very low altitudes of 10 m. In contrast to that, this setup was tested at a more practical altitude of 50 m. It can be assumed that erroneous localizations of the spectrometer's measurement spot caused the weak correlations with ground based measurements. These errors mainly derived from the inaccuracies of the GNSS position and the imperfect nadir orientation of the gimbal. As an imaging system allows for better geo-referencing of the measurements, the spectrometer setup was regarded as inappropriate for practical use and the programmable multispectral camera system was developed.

The multispectral camera system utilizes four narrow wavelength bands of the red-edge region to infer above-ground biomass and nitrogen content. Its advantages are a powerful processing unit, a low weight, a small size and a low power consumption. It is based on an advanced image acquisition routine, accounting for the ambient light conditions and performing all steps from image acquisition to image-to-image registration on-the-fly. The dynamic computation of an adequate exposure time guarantees images with a high contrast and a great level of detail. The setup allows to create multispectral aerial images, which provide a high spatial resolution of 4 $cm\ px^{-1}$ at a flight altitude of 25 m. Moreover, real-time image processing algorithms can be deployed to this setup in future.

Within the last years, the development of small and lightweight hyperspectral imaging sensors generated new possibilities for UAV research. They combine the benefits of

a high spatial and spectral resolution and can be considered as multi-purpose sensor, covering almost any interesting wavelength in the VIS and NIR spectrum. With the advancement in technology, these system will become affordable and have the potential to become a standard sensor system for 3D modeling and canopy reflection analysis.

6.4 Performance tests in precision farming use cases

The UAS and the different camera systems were tested in two field experiments. The first experiment indicated that RGB images with a ground resolution of 4 $cm\ px^{-1}$ were suited to create 3D crop surface models with a sufficient level of detail. The classification algorithm performed automatic thresholding to simple VI orthoimages to derive crop coverage factors in corn. The predictive quality of the multiple linear regression model, combining crop height and crop coverage, was best at mid-season growth stages, as reported by (Yin et al., 2011a;b).

In the second experiment, the multispectral camera system proved to be a valuable imaging system, perfectly suited for the desired task of nitrogen fertilization information retrieval. The camera system created multispectral images at a ground resolution of 4 $cm\ px^{-1}$, which have been processed to NDVI and REIP orthoimages. The NDVI allowed to estimate the above-ground biomass in winter wheat at high accuracies, whereas the REIP allowed to estimate the nitrogen content even more accurately. The results are comparable to the findings of Erdle et al. (2011), who investigated the performance of commercial ground based systems. Also, the prediction of grain yield and grain protein content performed at high accuracies, indicating that nitrogen fertilization strategies can be build on remotely sensed in-season canopy information.

The presented results demonstrate the potential of the proposed methods. Nevertheless, they should be regarded as indicators, only. Since the field trials have only been carried out within a period of one year and with a high level of in-field heterogeneity, the methods have yet to prove applicability under realistic conditions.

Although being based on simple statistical models, the processing methods show promising results. With the advancement in hyperspectral aerial sensing, more sophisticated approaches can be considered. Øvergaard et al. (2010; 2013) have already demonstrated the possibilities multivariate methods can offer in reflectance analysis. A combination of spatial and spectral information could be used in future methods, comprising crop shape and location, bi-directional reflection, fluorescence, and thermal information.

Both experiments also demonstrated the limitations of imaging approaches. There is still a need of intensive post-processing to create 3D models and orthoimages. Moreover, to guarantee high spatial accuracies, ground control points need to be deployed and measured before the flight mission. Research is heading towards real-time georeferencing and image processing methods, but these methods are not state-of-the-art, yet. For accurate absolute positioning, these methods heavily rely on the UAV's on-

board navigation sensors, which commonly lack highest accuracy. In addition, most of the sensor systems, which are currently in use, do not offer the required processing capabilities.

6.5 Sensor data infrastructure

The standardized sensor data infrastructure sets the basis of an advanced network of sensor systems, data bases, and web processing services. It was implemented with open source software and data standards to guarantee a high level of interoperability in between any kind of component, following the recommendation of Nash et al. (2009). It is a simple and effective approach to make spatio-temporal agricultural sensor data accessible for a service-oriented data architecture. The data can be processed by self-developed routines to be used in FMISs. In addition, external partners can offer web processing services and perform the analysis of the sensor data remotely.

A current disadvantage is that the infrastructure targets at real-time sensor data acquisition. It is also possible to deploy sensor data in post-processing, but this results in an increased after mission effort and the need of expert knowledge. As manual user interaction is intended to be avoided wherever possible, mobile network coverage and bandwidth issues play an important role. However, with an expected advance in mobile network technology this problem will hopefully be solved in the near future. The infrastructure itself, demonstrates a valuable step to a holistic data management of a farm, as addressed by Fountas et al. (2015).

6.6 Applicability to and perspectives in precision farming

This thesis demonstrated the successful development of an advanced UAS and a sensor data infrastructure with real-time data processing functionality. The UAS is fully programmable and can, therefore, be adapted to any kind of PF application. The developed imaging sensors and processing routines are suitable to generate 3D CSMs and VIs to infer crop parameters, like crop height, above-ground biomass and nitrogen content. The image processing routines are sophisticated and are carried out in post-processing, until now. The implemented sensor data infrastructure may be regarded as an intelligent mean of data acquisition and storage in a standardized web-enabled environment. PF web services and real-time applications can be built utilizing the provided network capabilities.

Further improvement in UAV technology will combine the benefits of fixed-wing and rotary-wing platforms. Seibel et al. (2015) already proposed an improved fixed-wing UAV, by enriching it with hovering and vertical take-off and landing abilities. This is a next step towards practical applicability for wide-area scenarios. The possibilities of coordinated missions of aerial and ground vehicle teams, as well as improved machine-to-machine communication have the potential to promote UASs for future farming.

However, for establishing UAS in PF practice, the technology needs to undergo more improvements first. As UAS handling and data processing is still a complicated task, the development of a 'push-one-button system' is desirable for practical usage. A further step to such a system is to develop real-time data processing routines, based on the proposed analysis strategies. Moreover, the utilization of the sensor data infrastructure for automatized sensor data acquisition and standardized sensor data storage ensures interoperability of all parts of a FMIS. The implementation of web processing services, e.g. for the generation of application maps, facilitates the process of information generation and makes the data usable, even for non-expert users. This is an important feature, as the intensive post-processing cannot be performed by farmers themselves. Until UASs are able to operate fully autonomously, close-range remote sensing should be considered as an agricultural service of specialized companies only.

References

Aasen, H., A. Burkart, A. Bolten and G. Bareth, 2015. Generating 3D hyperspectral information with lightweight UAV snapshot cameras for vegetation monitoring: From camera calibration to quality assurance. *ISPRS Journal of Photogrammetry and Remote Sensing*, 108:245–259.

Adamchuk, V., J. Hummel, M. Morgan and S. Upadhyaya, 2004. On-the-go soil sensors for precision agriculture. *Computers and Electronics in Agriculture*, 44(1):71–91.

Auernhammer, H., 2001. Precision farming – the environmental challenge. *Computers and Electronics in Agriculture*, 30:31–43.

Bendig, J., A. Bolten and G. Bareth, 2013. UAV-based imaging for multi-temporal, very high resolution crop surface models to monitor crop growth variability. *Photogrammetrie, Fernerkundung, Geoinformation*, 2013(6):551–562.

Bendig, J., K. Yu, H. Aasen, A. Bolten, S. Bennertz, J. Broscheit, M. L. Gnyp and G. Bareth, 2015. Combining UAV-based plant height from crop surface models, visible, and near infrared vegetation indices for biomass monitoring in barley. *International Journal of Applied Earth Observation and Geoinformation*, 39:79–87.

Berni, J., P. Zarco-Tejada, L. Suarez and E. Fereres, 2009. Thermal and Narrowband Multispectral Remote Sensing for Vegetation Monitoring From an Unmanned Aerial Vehicle. *IEEE Transactions on Geoscience and Remote Sensing*, 47(3):722–738.

Bongiovanni, R. and J. Lowenberg-Deboer, 2004. Precision Agriculture and Sustainability. *Precision Agriculture*, 5(4):359–387.

Borra-Serrano, I., J. M. Peña, J. Torres-Sánchez, F. J. Mesas-Carrascosa and F. López-Granados, 2015. Spatial Quality Evaluation of Resampled Unmanned Aerial Vehicle-Imagery for Weed Mapping. *Sensors*, 15(8):19688–19708.

Burkart, A., H. Aasen, L. Alonso, G. Menz, G. Bareth and U. Rascher, 2015. Angular Dependency of Hyperspectral Measurements over Wheat Characterized by a Novel UAV Based Goniometer. *Remote Sensing*, 7(1):725–746.

Burkart, A., S. Cogliati, A. Schickling and U. Rascher, 2014. A Novel UAV-Based Ultra-Light Weight Spectrometer for Field Spectroscopy. *IEEE Sensors Journal*, 14(1):62–67.

Bürkle, A., F. Segor and M. Kollmann, 2011. Towards Autonomous Micro UAV Swarms. *Journal of Intelligent & Robotic Systems*, 61(1-4):339–353.

CAA, 2015. *Unmanned Aircraft System Operations in UK Airspace – Guidance*. UK Civil Aviation Authority, Gatwick,West Sussex, UK, 6 edn.

Calderón, R., J. Navas-Cortés, C. Lucena and P. Zarco-Tejada, 2013. High-resolution airborne hyperspectral and thermal imagery for early detection of Verticillium wilt of olive using fluorescence, temperature and narrow-band spectral indices. *Remote Sensing of Environment*, 139:231–245.

Colomina, I. and P. Molina, 2014. Unmanned aerial systems for photogrammetry and remote sensing: A review. *ISPRS Journal of Photogrammetry and Remote Sensing*, 92:79–97.

Corwin, D. and S. Lesch, 2005. Apparent soil electrical conductivity measurements in agriculture. *Computers and Electronics in Agriculture*, 46(1–3):11–43.

Cubert GmbH, 2015. http://cubert-gmbh.de/uhd-185-firefly/, accessed on 2015-11-07. UHD 185 – Firefly.

Díaz-Varela, R. A., R. de la Rosa, L. León and P. J. Zarco-Tejada, 2015. High-Resolution Airborne UAV Imagery to Assess Olive Tree Crown Parameters Using 3D Photo Reconstruction: Application in Breeding Trials. *Remote Sensing*, 7(4):4213–4232.

Eisenbeiss, H., 2007. Applications of photogrammetric processing using an autonomous model helicopter. *Revue Francaise de Photogrammetrie et de Teledetection*, (185):51–56.

Erdle, K., B. Mistele and U. Schmidhalter, 2011. Comparison of active and passive spectral sensors in discriminating biomass parameters and nitrogen status in wheat cultivars. *Field Crops Research*, 124(1):74–84.

Fountas, S., G. Carli, C. Sørensen, Z. Tsiropoulos, C. Cavalaris, A. Vatsanidou, B. Liakos, M. Canavari, J. Wiebensohn and B. Tisserye, 2015. Farm management information systems: Current situation and future perspectives. *Computers and Electronics in Agriculture*, 115:40–50.

Gonzalez-Dugo, V., P. Zarco-Tejada, E. Nicolás, P. Nortes, J. Alarcón, D. Intrigliolo and E. Fereres, 2013. Using high resolution UAV thermal imagery to assess the variability in the water status of five fruit tree species within a commercial orchard. *Precision Agriculture*, 14(6):660–678.

Griepentrog, H., M. Nørremark, H. Nielsen and B. Blackmore, 2005. Seed Mapping of Sugar Beet. *Precision Agriculture*, 6(2):157–165.

Guyot, G., F. Baret and S. Jacquemoud, 1992. Imaging spectroscopy for vegetation studies. In F. Toselli and J. Bodechtel, eds., *Imaging Spectroscopy: Fundamentals and Prospective Applications*, pages 145–165. Kluwer Academic Publishers, Dordrecht, The Netherlands.

Guyot, G., F. Baret and D. J. Major, 1988. High spectral resolution: Determination of spectral shifts between the red and infrared. *International Archives of Photogrammetry and Remote Sensing*, XXVII(B7):750–760.

Hakala, T., J. Suomalainen and J. I. Peltoniemi, 2010. Acquisition of Bidirectional Reflectance Factor Dataset Using a Micro Unmanned Aerial Vehicle and a Consumer Camera. *Remote Sensing*, 2(3):819–832.

Heege, H., S. Reusch and E. Thiessen, 2008. Prospects and results for optical systems for site-specific on-the-go control of nitrogen-top-dressing in Germany. *Precision Agriculture*, 9(3):115–131.

Hernandez, A., H. Murcia, C. Copot and R. De Keyser, 2015. Towards the Development of a Smart Flying Sensor: Illustration in the Field of Precision Agriculture. *Sensors*, 15(7):16688–16709.

Horler, D., M. Dockray and J. Barber, 1983. The red edge of plant leaf reflectance. *International Journal of Remote Sensing*, 4(2):273–288.

Hunt Jr., E., W. Dean Hively, S. Fujikawa, D. Linden, C. Daughtry and G. McCarty, 2010. Acquisition of NIR-green-blue digital photographs from unmanned aircraft for crop monitoring. *Remote Sensing*, 2(1):290–305.

Jones, H. G., R. Serraj, B. R. Loveys, L. Xiong, A. Wheaton and A. H. Price, 2009. Thermal infrared imaging of crop canopies for the remote diagnosis and quantification of plant responses to water stress in the field. *Functional Plant Biology*, 36:978–989.

Kaivosoja, J., M. Jackenkroll, R. Linkolehto, M. Weis and R. Gerhards, 2014. Automatic control of farming operations based on spatial web services. *Computers and Electronics in Agriculture*, 100:110–115.

Kazmi, W., M. Bisgaard, F. Garcia-Ruiz, K. D. Hansen and A. la Cour-Harbo, 2011. Adaptive Surveying and Early Treatment of Crops with a Team of Autonomous Vehicles. In A. J. Lilienthal and T. Duckett, eds., *In Proceedings of the 5th European Conference on Mobile Robots ECMR2011*, pages 253–258. Örebro University, Örebro, Sweden.

Kise, M., Q. Zhang and F. R. Mas, 2005. A Stereovision-based Crop Row Detection Method for Tractor-automated Guidance. *Biosystems Engineering*, 90(4):357–367.

Kuhnert, L., K. Müller, M. Ax and K.-D. Kuhnert, 2012. Object localization on agricultural areas using an autonomous team of cooperating ground and air robots. In *Proceedings of the International Conference of Agricultural Engineering CIGR-Ageng2012*. International Commision of Agricultural Engineering (CIGR), Valencia, Spain.

Kusnierek, K. and A. Korsaeth, 2014. Challenges in using an analog uncooled microbolometer thermal camera to measure crop temperature. *International Journal of Agricultural and Biological Engineering*, 7(4):60–74.

Lawson, L. G., S. M. Pedersen, C. G. Sørensen, L. Pesonen, S. Fountas, A. Werner, F. W. Oudshoorn, L. Herold, T. Chatzinikos, I. M. Kirketerp and S. Blackmore, 2011. A four nation survey of farm information management and advanced farming systems: A descriptive analysis of survey responses. *Computers and Electronics in Agriculture*, 77(1):7–20.

Leemans, V. and M.-F. Destain, 2007. A computer-vision based precision seed drill guidance assistance. *Computers and Electronics in Agriculture*, 59(1–2):1–12.

McBratney, A., B. Whelan, T. Ancev and J. Bouma, 2005. Future Directions of Precision Agriculture. *Precision Agriculture*, 6(1):7–23.

McHugh, A., J. Tullberg and D. Freebairn, 2009. Controlled traffic farming restores soil structure. *Soil and Tillage Research*, 104(1):164–172.

microdrones GmbH, 2015. www.microdrones.com/en/products/technology/mdsi2/, accessed on 2015-10-29. Flexible Payload Integration.

Nash, E., P. Korduan and R. Bill, 2009. Applications of open geospatial web services in precision agriculture: a review. *Precision Agriculture*, 10(6):546–560.

Pedersen, S. M., S. Fountas, B. S. Blackmore, M. Gylling and J. L. Pedersen, 2004. Adoption and perspectives of precision farming in Denmark. *Acta Agriculturae Scandinavica, Section B – Soil & Plant Science*, 54(1):2–8.

Primicerio, J., S. Di Gennaro, E. Fiorillo, L. Genesio, E. Lugato, A. Matese and F. Vaccari, 2012. A flexible unmanned aerial vehicle for precision agriculture. *Precision Agriculture*, 13(4):517–523.

Rascher, U., A. Damm, S. van der Linden, A. Okujeni, R. Pieruschka, A. Schickling and P. Hostert, 2010. Sensing of Photosynthetic Activity of Crops. In E.-C. Oerke, R. Gerhards, G. Menz and R. A. Sikora, eds., *Precision Crop Protection - the Challenge and Use of Heterogeneity*, pages 87–99. Springer Verlag, Dordrecht; Heidelberg; London; New York.

Reichardt, M., C. Jürgens, U. Klöble, J. Hüter and K. Moser, 2009. Dissemination of precision farming in Germany: acceptance, adoption, obstacles, knowledge transfer and training activities. *Precision Agriculture*, 10(6):525–545.

Reyns, P., B. Missotten, H. Ramon and J. De Baerdemaeker, 2002. A Review of Combine Sensors for Precision Farming. *Precision Agriculture*, 3(2):169–182.

Rikola Ltd., 2015. http://www.rikola.fi/site/products/hyperspectral-camera/, accessed on 2015-11-07. Hyperspectral Camera.

Rouse Jr., J. W., R. H. Haas, J. A. Schell and D. W. Deering, 1974. Monitoring vegetation systems in the Great Plains with ERTS. *NASA special publication*, 351:309–317.

Rueda-Ayala, V., G. Peteinatos, R. Gerhards and D. Andújar, 2015. A Non-Chemical System for Online Weed Control. *Sensors*, 15(4):7691–7707.

Seibel, F., M. Wohlfahrt and M. Kriegel, 2015. AIRCRAFT, PREFERABLY UNMANNED. US Patent 20,150,136,897.

Sørensen, C. G., S. Fountas, E. Nash, L. Pesonen, D. Bochtis, S. M. Pedersen, B. Basso and S. B. Blackmore, 2010. Conceptual model of a future farm management information system. *Computers and Electronics in Agriculture*, 72(1):37–47.

Stafford, J., 2000. Implementing precision agriculture in the 21st century. *Journal of Agricultural Engineering Research*, 76(3):267–275.

Stagakis, S., V. González-Dugo, P. Cid, M. Guillén-Climent and P. Zarco-Tejada, 2012. Monitoring water stress and fruit quality in an orange orchard under regulated deficit irrigation using narrow-band structural and physiological remote sensing indices. *ISPRS Journal of Photogrammetry and Remote Sensing*, 71:47–61.

Thenkabail, P. S., J. G. Lyon and A. Huete, 2012. Advances in Hyperspectral Remote Sensing of Vegetation and Agricultural Croplands. In P. S. Thenkabail, J. G. Lyon and A. Huete, eds., *In Hyperspectral Remote Sensing of Vegetation*, pages 4–35. Crc Press Inc, Boca Raton, Florida, USA.

Tilman, D., K. Cassman, P. Matson, R. Naylor and S. Polasky, 2002. Agricultural sustainability and intensive production practices. *Nature*, 418:671–677.

Tullberg, J., D. Yule and D. McGarry, 2007. Controlled traffic farming – From research to adoption in Australia. *Soil and Tillage Research*, 97(2):272–281.

Van Der Wal, T., B. Abma, A. Viguria, E. Previnaire, P. Zarco-Tejada, P. Serruys, E. Van Valkengoed and P. Van Der Voet, 2013. Fieldcopter: Unmanned aerial systems for crop monitoring services. In J. Stafford, ed., *Precision agriculture '13*, pages 169–175. Wageningen Academic Publishers.

Watts, A. C., V. G. Ambrosia and E. A. Hinkley, 2012. Unmanned aircraft systems in remote sensing and scientific research: classification and considerations of use. *Remote Sensing*, 4(12):1671–1692.

Weis, M., C. Gutjahr, V. Rueda Ayala, R. Gerhards, C. Ritter and F. Schölderle, 2008. Precision farming for weed management: techniques. *Gesunde Pflanzen*, 60:171–181.

Whelan, B. M. and A. B. McBratney, 2000. The "null hypothesis" of precision agriculture management. *Precision Agriculture*, 2(3):265–279.

Yin, X., N. Jaja, M. A. McClure and R. M. Hayes, 2011a. Comparison of Models in Assessing Relationship of Corn Yield with Plant Height Measured during Early- to Mid-Season. *Journal of Agricultural Science*, 3(3):14–24.

Yin, X., M. A. McClure, N. Jaja, D. D. Tyler and R. M. Hayes, 2011b. In-Season Prediction of Corn Yield Using Plant Height under Major Production Systems. *Agronomy Journal*, 103(3):923–929.

Zarco-Tejada, P., R. Diaz-Varela, V. Angileri and P. Loudjani, 2014. Tree height quantification using very high resolution imagery acquired from an unmanned aerial vehicle (UAV) and automatic 3D photo-reconstruction methods. *European Journal of Agronomy*, 55(0):89–99.

Zarco-Tejada, P., V. González-Dugo and J. Berni, 2012. Fluorescence, temperature and narrow-band indices acquired from a UAV platform for water stress detection using a micro-hyperspectral imager and a thermal camera. *Remote Sensing of Environment*, 117:322–337. Remote Sensing of Urban Environments.

Zecha, C. W., J. Link and W. Claupein, 2013. Mobile sensor platforms: categorisation and research applications in precision farming. *Journal of Sensors and Sensor Systems*, 2:51–72.

Zhang, C. and J. M. Kovacs, 2012. The application of small unmanned aerial systems for precision agriculture: a review. *Precision Agriculture*, 13(6):693–712.

Åstrand, B. and A.-J. Baerveldt, 2005. A vision based row-following system for agricultural field machinery. *Mechatronics*, 15(2):251–269.

Øvergaard, S., T. Isaksson and A. Korsaeth, 2013. Prediction of wheat yield and protein using remote sensors on plots – Part I: assessing near infrared model robustness for year and site variations. *Journal of Near Infrared Spectroscopy*, 21(2):117–131.

Øvergaard, S. I., T. Isaksson, K. Kvaal and A. Korsaeth, 2010. Comparisons of two hand-held, multispectral field radiometers and a hyperspectral airborne imager in terms of predicting spring wheat grain yield and quality by means of powered partial least squares regression. *Journal of Near Infrared Spectroscopy*, 18(4):247–261.

Publications

The following paragraphs list all peer-reviewed and non-peer-reviewed publications associated with this dissertation.

Peer-reviewed publications

Geipel, J., J. Link, J. A. Wirwahn and W. Claupein, 2016. A Programmable Aerial Multispectral Camera System for In-Season Crop Biomass and Nitrogen Content Estimation. *Agriculture*, 6(1):4.

Geipel, J., M. Jackenkroll, M. Weis and W. Claupein, 2015. A Sensor Web-Enabled Infrastructure for Precision Farming. *ISPRS International Journal of Geo-Information*, 4(1):385–399.

Geipel, J., J. Link and W. Claupein, 2014. Combined Spectral and Spatial Modeling of Corn Yield Based on Aerial Images and Crop Surface Models Acquired with an Unmanned Aircraft System. *Remote Sensing*, 6(11):10335–10355.

Geipel, J., G. G. Peteinatos, W. Claupein and R. Gerhards, 2013. Enhancement of micro Unmanned Aerial Vehicles for agricultural aerial sensor systems. In J. V. Stafford, ed., *Precision agriculture '13*, pp. 161–167. Wageningen Academic Publishers, Wageningen, The Netherlands.

Non-peer-reviewed publications

Link, J., J. Geipel and W. Claupein, 2015. Einsatz der unbemannt fliegenden Multi-Sensor-Plattform „Hexe“ zur Berechnung teilflächenspezifisch angepasster N-Düngermengen in Winterweizen. In H. Kage, K. Sieling, and L. Francke-Weltmann, eds., *Mitteilungen der Gesellschaft für Pflanzenbauwissenschaften, Multifunktionale Agrarlandschaften – Pflanzenbaulicher Anspruch, Biodiversität, Ökosystemdienstleistungen*, volume 27, pp. 171–172. Verlag Liddy Halm, Göttingen, Germany.

Geipel, J., J. A. Wirwahn, J. Link and W. Claupein, 2014. Eine programmierbare Red Edge Inflection Point (REIP) Kamera für Unmanned Aircraft Systems (UAS). In C. Pekrun, M. Wachendorf, and L. Francke-Weltmann, eds., *Mitteilungen der Gesellschaft für Pflanzenbauwissenschaften, Nachhaltige Erzeugung von Nachwachsenden Rohstoffen*, volume 26, pp. 300–301. Verlag Liddy Halm, Göttingen, Germany.

Geipel, J., G. G. Peteinatos, J. Link and W. Claupein, 2013. “Hexe”: Eine unbemannt fliegende Multi-Sensor-Plattform zur Erfassung hyperspektraler Daten. In C. Pekrun, M. Wachendorf, and L. Francke-Weltmann, eds., *Mitteilungen der Gesellschaft für Pflanzenbauwissenschaften, Technik in der Pflanzenproduktion*, volume 25, pp. 295–296. Verlag Liddy Halm, Göttingen, Germany.

Geipel, J. and W. Claupein, 2012. Anforderungen an unbemannt fliegende Sensor-

plattformen (Unmanned Aircraft Systems) als Entscheidungshilfe im Pflanzenbaumanagement. In C. Pekrun, M. Wachendorf, T. Müller, J. Utermann, and A. Düker, eds., *Mitteilungen der Gesellschaft für Pflanzenbauwissenschaften, Bodenfruchtbarkeit – Bedeutung und Bestimmung in Pflanzenbau und Bodenkunde*, volume 24, pp. 260–261. Verlag Liddy Halm, Göttingen, Germany.

Link-Dolezal, J., J. Geipel, Ch. Zecha and W. Claupein, 2012. Erhebung aerialer Multispektraldaten in Winterweizen. In C. Pekrun, M. Wachendorf, T. Müller, J. Utermann, and A. Düker, eds., *Mitteilungen der Gesellschaft für Pflanzenbauwissenschaften, Bodenfruchtbarkeit – Bedeutung und Bestimmung in Pflanzenbau und Bodenkunde*, volume 24, p. 274. Verlag Liddy Halm, Göttingen, Germany.

Acknowledgements

I want to express my gratitude to a number of people for supporting me and giving me the confidence in my work on this thesis. I thank my supervisor Prof. Dr. Wilhelm Claupein for granting me freedom of thought and placing trust in my ideas. Moreover, I thank Prof. Dr. Wolfgang Dorner and Prof. Dr. Hans W. Griepentrog for examining this thesis. I also acknowledge Prof. Dr. Roland Gerhards and Prof. Dr. Hans W. Griepentrog for always supporting me and giving me a place to concentrate on my work.

Furthermore, I thank my co-supervisor Johanna and my colleagues Gerassimos, Markus, and Martin. You are a great source of inspiration, feedback, and support. I thank Jan and Matthias for the important assistance in sensor development. For the many hands helping with my field trials, I profoundly thank Andrea, Marianne, Herbert, Markus, Martin, and the whole team at Ihinger Hof research station. Christine, thank you for always proofreading.